

**PHENOTYPIC AND METABOLIC PROFILING OF  
BIOLOGICAL SAMPLES IN NEAR REAL-TIME  
USING RAMAN SPECTROSCOPY**

Theresah Nom Korbieh Zu

Dissertation submitted to the faculty of the Virginia Polytechnic Institute and State  
University in partial fulfillment of the requirements for the degree of

Doctor of Philosophy  
In  
Biological Systems Engineering

Ryan S. Senger (Chair)

Justin R. Barone  
Jactone A. Ogejo  
Eva Collakova  
John L. Robertson

September 18, 2014  
Blacksburg, Virginia

**Keywords:** Raman spectroscopy, surface enhanced Raman scattering, microbial phenotyping, alcohol toxicity, organ transplantation, *ex vivo* perfusion, near real-time analysis, silver nanoparticles

Copyright

# Phenotypic and Metabolic Profiling of Biological Samples in Near Real-Time Using Raman Spectroscopy

Theresah N. Korbich Zu

## ABSTRACT

Raman spectroscopy, together with multivariate statistical analyses, has proven to be a near real-time analytical technique capable of phenotyping cells, tissues and organs. This dissertation will show exclusively the application of the Raman spectroscopy phenotypic profiling method to; (i) microbial toxicity, (ii) *ex-vivo* organ perfusion, and (iii) subcellular location targeting.

Real-time analytical methods for monitoring living biological systems will enable study of the physiological changes associated with growth, genetic manipulations, and adverse environmental conditions. Most existing analytical methods (NMR exempt), though highly accurate, must be performed off-line and most require destruction of the studied sample. These attributes make these methodologies less desirable to the study of physiological changes of cells, tissues, and organs. In this work, Raman spectroscopy has been identified and shown to be a good candidate for real-time analysis mainly because it can be performed: (i) in near real-time, (ii) non-destructively and with minimal sample preparation, (iii) through a glass barrier (i.e., can be performed *in situ*), and (iv) with minimal spectral interference from water. Here, Raman spectroscopy was used in combination with multivariate statistics to analyze the differing toxic effects of 4-C chain alcohols on *E. coli*. Good correlations were established between Raman spectra and off-line analytical techniques used to measure: (i) saturated, unsaturated, and cyclopropane fatty acids; (ii) amino acid composition of total protein; and (iii) cell membrane fluidity. Also, Raman “fingerprint” analysis was used to discriminate among different phenotypic responses of cells. In addition, this methodology was applied to analyze perfusates of organs maintained by the VasoWave<sup>®</sup> organ perfusion system. Raman fingerprints can be used to assess organ health, and it is believed this data can be used to inform decisions such as whether or not to transplant an organ. Finally, molecular biology techniques were used to design and produce specific protein targets harboring a silver binding domain fusion, which upon release migrate to specific subcellular locations. By employing the related technique of surface-enhanced Raman scattering (SERS), which produces a highly amplified Raman signal in the presence of metallic nanoparticle substrates (e.g., silver nanoparticles), different regions of the *E. coli* cell structure were studied. The target regions studied by the technique included: (i) outer cell membrane, (ii) periplasm, and the (iii) cytoplasm.

## Dedication

This dissertation is dedicated to the memory of my late father, **Peter B. C. Korbieh**, without whom I may never have stumbled onto the joys of being a scientist.

To my husband, **Prince N. Zu**, for your continual encouragement and support throughout my MS. and Ph.D. studies, sacrificing the warmth of your wife so I could pursue my dreams ... thank you!

To my daughter, **Nadine M. Zu**, for keeping me company in the absence of daddy and for making this Ph.D. journey all the more fulfilling.

To my mother, **Margaret S. Rudolph**, for your encouragement.

To my siblings, **Laah, Sungliedong, Dery, Fuunaangmin, and Mankuyeli**.

To **the Rudolph Tuotaah, Korbieh, Kontuo, and Zu families**, for missing the joys of your daughter and wife over the past couple of years I have been away in school out of Ghana.

## Acknowledgments

I would like to thank my advisor **Dr. Ryan S. Senger** for his dedication and patience working with me throughout the course of my research work and also for his mentorship on professional and personal matters.

I would like to acknowledge my committee members **Dr. Justin R. Barone, Dr. Jactone A. Ogejo, Dr. Eva Collakova, and Dr. John L. Robertson** for your continued guidance and support throughout my tenure here in Virginia Tech.

I am indebted to **Dr. Ahmad I. M. Athamneh** for your guidance and training on the use of the Raman spectrometer and the initial statistical analysis with MATLAB.

Acknowledgements are also sent out to my research group in the Senger lab – Hadi Nazeem-Bokae, Benjamin Freedman, John Yen, and Imen Tanniche, for your friendship and intellectual interactions that have helped shaped me into the professional I am today.

Finally, and most importantly, I would like to acknowledge the **Biological Systems Engineering** department for financial assistance to embark on this life's journey.

## Attribution

All four (4) main chapters – chapter 2 through to chapter 5, are manuscript accepted for publication, submitted or yet to be submitted for publication, with each manuscript having a list of contributing authors.

**CHAPTER TWO:** Near real-time analysis of the phenotypic responses of *Escherichia coli* to 1-butanol exposure using Raman spectroscopy

Manuscript has been accepted for publication to the Journal of Bacteriology

Ahmad I. M. Athamneh, Ph.D. is currently a postdoctoral research scientist in Purdue University. Dr. Athamneh is a contributing author to this paper and helped with Raman data acquisition, Raman data analysis and also Fluorescence anisotropy (membrane fluidity) experiments.

Robert S. Wallace, was an undergraduate researcher with the Senger research group at the time of the experiments and helped out with total protein assay measurements.

Eva Collakova, Ph. D. is currently an assistant professor in the department of Plant Pathology, Physiology and Weed Science at Virginia Tech and facilitated all GC-MS/FID experiments and analysis. Dr. Collakova is a contributing author to the manuscript

Ryan S. Senger, Ph.D. is currently an assistant professor in the department of Biological Systems Engineering at Virginia Tech and served as the principal investigator (P.I) for the project. Dr. Senger is a contributing author to the manuscript.

**CHAPTER THREE:** Assessment of *ex vivo* perfused liver health by Raman spectroscopy

Manuscript under review by Journal of Raman Spectroscopy

Ahmad I. M. Athamneh, Ph.D. is currently a postdoctoral research scientist in Purdue University. Dr. Athamneh is a contributing author to this paper and helped with Raman data analysis.

Eva Collakova, Ph. D. is currently an assistant professor in the department of Plant Pathology, Physiology and Weed Science at Virginia Tech and facilitated all GC-MS/FID experiments and analysis. Dr. Collakova is a contributing author to the manuscript

John Robertson, VMD, Ph.D., is currently a professor with both the Virginia-Maryland Regional College of Veterinary Medicine and the School of Biomedical Engineering and Science. Dr. Rob was the principal investigator for perfusion experiments done in collaboration with the Smart Perfusion Company located in Denver, NC and also a contributing author to the manuscript

Chip Aardema, was a researcher in Dr. Robertson's lab in the Virginia-Maryland Regional College of Veterinary Medicine at Virginia Tech at the time of the liver experiments. Chip helped with the perfusion of livers and collection of samples for Raman spectroscopy analysis.

Thomas Hawken, VMD is a graduate of the Virginia-Maryland Regional College of Veterinary Medicine at Virginia Tech and assisted with perfusion experiments.

Ryan S. Senger, Ph.D. is currently an assistant professor in the department of Biological Systems Engineering at Virginia Tech and served as the principal investigator (P.I) for the project. Dr. Senger is a contributing author to the manuscript.

**CHAPTER FOUR:** A study of the phenotypic responses of *Escherichia coli* to multiple 4-carbon alcohols using Raman spectroscopy

Manuscript to be submitted to Journal of Bacteriology in October 2014.

Ahmad I. M. Athamneh, Ph.D. is currently a postdoctoral research scientist in Purdue University. Dr. Athamneh is a contributing author to this paper.

Ryan S. Senger, Ph.D. is currently an assistant professor in the department of Biological Systems Engineering at Virginia Tech and served as the principal investigator (P.I) for the project. Dr. Senger is a contributing author to the manuscript.

**CHAPTER FIVE:** Peptide-guided silver nanoparticles for spatio-temporal surface-enhanced Raman spectroscopy (SERS) analysis of target cellular locations in the *E. coli* bacterium

Manuscript to be submitted to a peer-reviewed Journal by December 2014.

Theresah N. K. Zu, Ph.D., Ahmad I. M. Athamneh, Ph. D., and Ryan S. Senger Ph.D. conceived the study.

Theresah N. K. Zu, Ph.D. and Ahmad I. M. Athamneh performed the *ex vivo* pgSERS assembly and analysis.

Theresah N. K. Zu, Ph.D., Benjamin G. Freedman, (Ph.D. candidate, Biological Systems Engineering department, Virginia Tech) and Imen Tanniche (Ph.D. student, Biological

Systems Engineering department, Virginia Tech) performed the *in vivo* pgSERS assembly and analysis.

Theresah N. K. Zu, Ph.D., Ahmad I. M. Athamneh, Ph.D. and Ryan S. Senger, Ph.D. analyzed the data.

All authors contributed to writing the manuscript, and all authors approved the final manuscript.

## TABLE OF CONTENTS

<b>ABSTRACT</b> .....	<b>ii</b>
<b>Dedication</b> .....	<b>iii</b>
<b>Acknowledgments</b> .....	<b>iv</b>
<b>Attribution</b> .....	<b>v</b>
<b>TABLE OF CONTENTS</b> .....	<b>viii</b>
<b>LIST OF FIGURES</b> .....	<b>xv</b>
<b>LIST OF TABLES</b> .....	<b>xxi</b>
<b>LIST OF ABBREVIATIONS</b> .....	<b>xxii</b>
<b>CHAPTER ONE: INTRODUCTION</b> .....	<b>1</b>
<b>MOTIVATION</b> .....	<b>1</b>
<b>ANALYSIS OF BIOLOGICAL SAMPLES</b> .....	<b>1</b>
<i>Motivation for biofuel research</i> .....	<b>2</b>
<i>Argument for organ perfusion</i> .....	<b>3</b>
<b>TRADITIONAL METHODS OF ANALYSES</b> .....	<b>3</b>
<b>RAMAN SPECTROSCOPY</b> .....	<b>4</b>
<b>CHALLENGES WITH RAMAN SPECTROSCOPY</b> .....	<b>5</b>
<b>HYPOTHESES</b> .....	<b>5</b>
<b>DISSERTATION SUMMARY</b> .....	<b>6</b>
<b>REFERENCES</b> .....	<b>8</b>

<b>CHAPTER TWO: Near real-time analysis of the phenotypic responses of <i>Escherichia coli</i> to 1-butanol exposure using Raman spectroscopy .....</b>	<b>12</b>
<b>ABSTRACT.....</b>	<b>13</b>
<b>INTRODUCTION.....</b>	<b>14</b>
<i>The role of product toxicity in biofuel production by microbes .....</i>	14
<i>Microbial toxicity mechanisms of alcohols .....</i>	14
<i>Monitoring dynamic phenotypes with Raman spectroscopy .....</i>	16
<i>Studying the response of E. coli to 1-butanol exposure using Raman spectroscopy ..</i>	18
<b>MATERIALS AND METHODS .....</b>	<b>18</b>
<i>Bacteria strain .....</i>	18
<i>Chemicals and reagents .....</i>	18
<i>Culture media, growth conditions, and harvesting.....</i>	19
<i>Raman spectroscopy.....</i>	20
<i>Raman data processing .....</i>	20
<i>Fatty acid analysis by GC-MS/FID.....</i>	21
<i>Total protein content, protein hydrolysis and amino acid analysis by UPLC .....</i>	21
<i>Membrane fluidity.....</i>	22
<b>RESULTS .....</b>	<b>23</b>
<i>Raman spectroscopy of growing and growth inhibited cells .....</i>	23
<i>Correlation of Raman spectroscopy and GC-FID for fatty acids analysis .....</i>	26

<i>Correlation of Raman spectroscopy and UPLC for amino acids analysis</i> .....	28
<i>Correlation of Raman spectroscopy and fluorescence anisotropy for cell membrane fluidity analysis</i> .....	30
<b>DISCUSSION</b> .....	32
<i>Use of Raman spectroscopy to study cell physiology in near real-time</i> .....	32
<i>Peak assignment observations and discrepancies</i> .....	33
<i>Potential applications</i> .....	34
<b>REFERENCES</b> .....	35
<b>CHAPTER THREE: Assessment of <i>ex vivo</i> perfused liver health by Raman spectroscopy</b> .....	<b>43</b>
<b>ABSTRACT</b> .....	44
<b>INTRODUCTION</b> .....	45
<b>Liver transplant statistics and challenges</b> .....	45
<i>Statistics</i> .....	45
<i>Guidelines for liver transplantation</i> .....	46
<i>Methods of organ storage pending transplant</i> .....	46
<i>Description of VasoWave® technologies</i> .....	47
<i>Methods for assessment of liver quality</i> .....	48
<i>Raman spectroscopy and liver disease diagnosis</i> .....	48
<i>Studying the effects of <i>ex vivo</i> perfusion on porcine liver health</i> .....	49

<b>MATERIALS AND METHODS</b> .....	50
<i>Animals and liver conditioning</i> .....	50
<i>Liver perfusion by VasoWave®</i> .....	50
<i>Raman spectroscopy</i> .....	51
<i>Fatty acid analysis</i> .....	52
<i>Total protein measurements</i> .....	52
<i>Statistical methods</i> .....	52
<b>RESULTS</b> .....	53
<i>Reproducibility and changes observed in Raman spectra</i> .....	53
<i>Multivariate statistical analysis of Raman spectra</i> .....	56
<i>Establishing a measure of time-dependent liver health</i> .....	64
<i>Correlating Raman bands with GC-FID FAME analysis results</i> .....	66
<i>Correlating Raman bands with total protein measurements</i> .....	67
<b>DISCUSSION</b> .....	69
<b>REFERENCES</b> .....	73
<b>CHAPTER FOUR: A study of the phenotypic responses of <i>Escherichia coli</i> to multiple 4-carbon alcohols using Raman spectroscopy</b> .....	<b>78</b>
<b>ABSTRACT</b> .....	79
<b>INTRODUCTION</b> .....	80
<i>Phenotyping with Raman spectroscopy</i> .....	80

<i>Conventional uses of Raman spectroscopy to analyze biological samples</i> .....	80
<i>Toxicity mechanisms of alcohols</i> .....	81
<i>Phenotypic responses to 4-carbon alcohols</i> .....	82
<b>MATERIALS AND METHODS</b> .....	83
<i>Bacteria strain and chemicals</i> .....	83
<i>Culture conditions</i> .....	84
<i>Raman spectroscopy</i> .....	84
<b>RESULTS</b> .....	85
<i>4-Carbon alcohol toxicity and inhibition of culture growth</i> .....	85
<i>Normalized Raman spectra</i> .....	86
<i>Discriminate analysis by alcohol</i> .....	88
<i>Discriminate analysis by time</i> .....	90
<i>Discriminant analysis by alcohol at multiple time points</i> .....	92
<b>DISCUSSION</b> .....	93
<i>Monitoring phenotypic changes in near real-time</i> .....	93
<i>Effects of terminal alkyl chain length</i> .....	94
<i>Potential uses</i> .....	95
<b>REFERENCES</b> .....	97

<b>CHAPTER FIVE: Peptide-guided silver nanoparticles for spatio-temporal surface-enhanced Raman spectroscopy (SERS) analysis of target cellular locations in the <i>E. coli</i> bacterium.....</b>	<b>102</b>
<b>ABSTRACT.....</b>	<b>103</b>
<b>INTRODUCTION.....</b>	<b>104</b>
<i>Advances in microbial phenotyping using Raman spectroscopy</i> .....	104
<i>Surface-enhanced Raman scattering (SERS)</i> .....	104
<i>In vivo assembly of pgSERS probes</i> .....	105
<i>FadL: An outer membrane protein</i> .....	106
<i>MalE: A periplasm localized protein</i> .....	107
<i>AroP: A cytoplasm localized protein</i> .....	108
<i>AgBP<sub>2</sub>: Silver binding domain</i> .....	109
<i>pgSERS for subcellular targeting of E. coli</i> .....	110
<b>MATERIALS AND METHODS .....</b>	<b>110</b>
<i>Bacterial strain, media, and growth conditions</i> .....	110
<i>PCR and cloning</i> .....	111
<i>Protein induction</i> .....	113
<i>Ex vivo pgSERS probe assembly</i> .....	113
<i>In vivo pgSERS probe assembly</i> .....	113
<i>TEM imaging</i> .....	113

<i>pgSERS analysis and data processing</i> .....	114
<b>RESULTS</b> .....	114
<i>Ex vivo pgSERS assembly</i> .....	114
<i>In vivo pgSERS assembly</i> .....	115
<i>Raman spectroscopy of in vivo assembled pgSERS probes</i> .....	118
<b>DISCUSSION</b> .....	122
<i>Use of SERS to acquire microbial phenotype signatures</i> .....	122
<i>Analyzing 1-butanol toxicity</i> .....	123
<i>Integrating pgSERS into metabolic engineering</i> .....	124
<b>REFERENCES</b> .....	125
<b>CHAPTER SIX: CONCLUSIONS</b> .....	<b>131</b>
<b>CHAPTER SEVEN: SUPPLEMENTARY MATERIALS</b> .....	<b>134</b>
<b>Supplementary Appendix</b> .....	134
<b>REFERENCES</b> .....	143

## LIST OF FIGURES

### CHAPTER TWO: Near real-time study of the phenotypic response of *Escherichia coli* to n-butanol exposure using Raman spectroscopy

**Figure 1.** Raman spectra of (a) the biological region (600-1800  $\text{cm}^{-1}$ ) and (b) the CH region (2800-3100  $\text{cm}^{-1}$ ) at time equal to 0 min (before the application of 1-butanol) (solid heavy red line), time equal to 180 min for the control cells (solid thin blue line), and time equal to 180 min after treatment for the 1-butanol treated cells (dashed black line). .....**24**

**Figure 2.** (a) Culture growth (OD600) and (b) Raman (I1449) measure of broader metabolic activity as functions of time for 1-butanol treated cells (blue squares) and control cells (red circles). 1-Butanol (1.2% v/v) was added to the treated cells at 0 min. Error bars represent 1 standard deviation among at least 3 biological replicates. ....**25**

**Figure 3.** (a) Saturated fatty acids measured by GC-FID, (b) unsaturated fatty acids measured by GC-FID, (c) cyclopropane fatty acids measured by GC-FID, (d) saturated fatty acids measured by Raman (I2870), (e) unsaturated fatty acids measured by Raman (I1263), (f) cyclopropane fatty acids measured by Raman (I1554) as functions of time for 1-butanol treated cells (blue squares) and control cells (red circles). 1-Butanol (1.2% v/v) was added to the treated cells at 0 min. Error bars represent 1 standard deviation among at least 3 biological replicates. ....**28**

**Figure 4.** (a) Change in fluorescence anisotropy (%) for 1-butanol treated cells relative to the control cells, (b) experimentally measured total protein content, (c) membrane fluidity (I2852/2924) measured by Raman, and (d) total protein content measured by Raman (I2954) as functions of time for 1-butanol treated cells (blue circles), control cells (red circles), and percent change between 1-butanol treated and control cells (blue diamonds).

1-Butanol (1.2% v/v) was added to the treated cells at 0 min. Error bars represent 1 standard deviation among at least 3 biological replicates.....32

**CHAPTER THREE: Assessment of *ex vivo* perfused liver health by Raman spectroscopy**

**Figure 1.** (a) Raman spectra of perfused porcine liver at the following time points: 2 hours before perfusion begins (blue line), 1 hour of perfusion (red line), and 8 hours of perfusion (green line). (b) The standard deviations of 50 replicate scans for each sample. ....55

**Figure 2.** (a) Raman spectra of the biological region at 8h of perfusion for livers perfused under conditions A (red line), B (green line), and C (blue line). (b) Raman spectra of the –CH region for the three livers. ....56

**Figure 3.** Discriminant analysis results of (a) un-perfused and perfused livers at 0 h and 8 h, (b) all data points for livers perfused under conditions A, B, and C discriminated by pressure, (c) all data points for livers perfused under conditions A, B, and C discriminated by temperature, and (d) all data points for livers perfused under conditions A, B, and C discriminated by time. ....58

**Figure 4.** Multivariate statistical analysis of the 2<sup>nd</sup> set of three livers. All data points for livers perfused under conditions A, B, and C discriminated by pressure.....59

**Figure 5.** Multivariate statistical analysis of the 2<sup>nd</sup> set of three livers. All data points for livers perfused under conditions A, B, and C discriminated by temperature .....60

**Figure 6.** Multivariate statistical analysis of the 2<sup>nd</sup> set of three livers. All data points for livers perfused under conditions A, B, and C discriminated by time.....61

**Figure 7.** Multivariate statistical analysis of all livers. All data points for livers perfused under conditions A, B, and C discriminated by pressure .....62

**Figure 8.** Multivariate statistical analysis of all livers. All data points for livers perfused under conditions A, B, and C discriminated by temperature.....63

**Figure 9.** Multivariate statistical analysis of all livers. All data points for livers perfused under conditions A, B, and C discriminated by time.....64

**Figure 10.** One-dimensional linear discriminant analysis by time for livers perfused under conditions (a) A, (b) B, and (c) C. The initial state of each liver is denoted by the “Fraction of Degradation” equal to 0, and the final state has a value equal to 1.....66

**Figure 11.** (a) Saturated fatty acids measured by GC-FID, (b) unsaturated fatty acids measured by GC-FID, (c) experimental measurements of total protein, (d) saturated fatty acids measured by Raman spectroscopy using peak intensity at 2850 cm<sup>-1</sup>, (e) unsaturated fatty acids measured by Raman spectroscopy using peak intensity at 1655 cm<sup>-1</sup>, (f) total protein measured by Raman spectroscopy using peak intensity at 1450 cm<sup>-1</sup>. Livers perfused under conditions A (blue-solid line), B (red line) and C (green line) are represented in each plot.....69

**CHAPTER FOUR: A study of the phenotypic responses of *Escherichia coli* to multiple 4-carbon alcohols using Raman spectroscopy**

**Figure 1.** Chemical structures of 4-carbon alcohols and *E. coli* culture growth inhibition. Each alcohol was added to 1.2% v/v at 0 min. Each curve label (A-E) corresponds to the alcohol above. The control culture is labeled F. ....86

**Figure 2.** Normalized and averaged Raman spectra of the control and alcohol-treated cultures at 180 min over (a) the biological range (700-1800 cm<sup>-1</sup>) and (b) the CH range (2800-3100 cm<sup>-1</sup>). ....88

**Figure 3.** DA results by alcohol. Three clusters are identified and consist of (1) 1-butanol and 2-butanol, (2) isobutanol and tert-butanol, and (3) the control and 1,4-butanediol treated cultures. ....90

**Figure 4.** DA results by time. The times given in the legend refer to minutes past the addition of alcohol. ....91

**Figure 5.** DA results by alcohol at (a) 60 min and (b) 180 min .....93

**CHAPTER FIVE: Peptide-guided surface-enhanced Raman scattering (pgSERS) for localized subcellular analysis of *E. coli***

**Figure 1.** The protein 3D structure for FadL (1T6 in the protein database (PDB)) (26).....107

**Figure 2.** The protein 3D structure for MalE (1FQA in the PDB) model from protein database (32).....108

**Figure 3.** The protein 3D structural prediction for AroP (P15993 in the Protein Model Portal (39)) .....109

**Figure 4.** *Ex vivo* assembly of pgSERS probes, localization in the *E. coli* interior, and resulting spectra when analyzed by Raman spectroscopy .....115

**Figure 5.** Visualization of the hypothesized protein-AgBP2-SNP *in vivo* assembly and localization for (a) FadL:AgBP<sub>2</sub>, (b) MalE:AgBP<sub>2</sub>, and (c) AroP:AgBP<sub>2</sub> .....116

**Figure 6.** SDS-page gel image showing the three proteins; (i) FadL, (ii) MalE, and (iii) AroP before and after induction with arabinose and in the presence of 1-butanol (but). .....117

**Figure 7.** Localization of protein:AgBP2-SNP conjugates at targeted locations of *E. coli* cells. SNP aggregates are shown as dark spots in b-f. The following images are shown: (a,b) control sample with no Ag-NPs added, (c) control sample mixed with unlabeled Ag-NPs, (d) induced FadL:AgBP<sub>2</sub> (targeting the outer membrane) mixed with Ag-NPs, (e) induced MalE:AgBP<sub>2</sub> (targeting the periplasm) mixed with Ag-NPs, and (f) induced AroP:AgBP<sub>2</sub> (targeting the cell interior) mixed with Ag-NPs. ....118

**Figure 8.** Averaged (n=10) SERS spectra (top), normal Raman (middle), and standard deviations of SERS signal (bottom) for *E. coli* cells containing the FadL:AgBP<sub>2</sub> fusion. The following SERS spectra are shown: (red) induced, (blue-dashed) uninduced, and (green) induced with 1-butanol exposure. The following normal Raman spectra are

shown: (red) induced, (blue-dashed) uninduced, and (green) induced with 1-butanol exposure. ....120

**Figure 9.** Averaged (n=10) SERS spectra (top), normal Raman (middle), and standard deviations of SERS signal (bottom) for *E. coli* cells containing the MalE:AgBP2 fusion. The following SERS spectra are shown: (red) induced, (blue-dashed) uninduced, and (green) induced with 1-butanol exposure. The following normal Raman spectra are shown: (red) induced, (blue-dashed) uninduced, and (green) induced with 1-butanol exposure. ....121

**Figure 10.** Averaged (n=10) SERS spectra (top), normal Raman (middle), and standard deviations of SERS signal (bottom) for *E. coli* cells containing the AroP:AgBP2 fusion. The following SERS spectra are shown: (red) induced, (blue-dashed) uninduced, and (green) induced with 1-butanol exposure. The following normal Raman spectra are shown: (red) induced, (blue-dashed) uninduced, and (green) induced with 1-butanol exposure. ....122

## LIST OF TABLES

### **CHAPTER TWO: Near real-time analysis of the phenotypic responses of *Escherichia coli* to 1-butanol exposure using Raman spectroscopy**

<b>Table 1.</b> Amino acid composition determined by Raman spectroscopy with an optimized set of bands and UPLC. The published amino acids composition of <i>E. coli</i> protein is also given.....	<b>29</b>
---	-----------

### **CHAPTER FIVE: Peptide-guided surface-enhanced Raman scattering (pgSERS) for localized subcellular analysis of *E. coli***

<b>Table 1.</b> PCR primers used to amplify the <i>fadL</i> , <i>malE</i> , and <i>aroP</i> genes for over-expression .....	<b>112</b>
---	------------

### **CHAPTER SEVEN: SUPPLEMENTARY MATERIALS**

<b>Supplementary Table 1.</b> Correlation coefficients (R values) for FAME analysis data with Raman spectroscopy data using Raman bands assigned in the literature and new bands identified in this research.....	<b>134</b>
---	------------

<b>Supplementary Table 2.</b> All literature cited Raman bands considered for each amino acid (8, 9) for compiling the optimized results shown in Table 1. ....	<b>139</b>
---	------------

<b>Supplementary Table 3.</b> Alternative Raman band assignment Set 1 for amino acids. Correlation coefficient (R) between Raman and UPLC data = 0.86. ....	<b>140</b>
---	------------

<b>Supplementary Table 4.</b> Alternative Raman band assignment Set 2 for amino acids. Correlation coefficient (R) between Raman and UPLC data = 0.89. ....	<b>141</b>
---	------------

<b>Supplementary Table 5.</b> Alternative Raman band assignment Set 3 for amino acids. Correlation coefficient (R) between Raman and UPLC data = 0.85The published amino acids composition of <i>E. coli</i> protein is also given. ....	<b>142</b>
--	------------

## LIST OF ABBREVIATIONS

AgB.	Silver-binding protein
AroP.	Aromatic protein
DPH.	1,3-diphenyl-1,3,5-hexatriene
ESI/M.	Electrospray ionization mass spectrometry
FadL	Long-chain fatty acid transporter
FAME.	Fatty acids as fatty acid methyl ester
FTIR.	Fourier transform infrared spectroscopy
GC-MS.	Gas chromatography-mass spectrometry
ICTAS.	Institute of Critical Technologies and Applied Science
IEO.	International Energy Outlook
IPCS.	International Program on Chemical Safety
K <sub>ow</sub>	Octanol-water partition coefficient
LB.	Luria-Burtani
LCFA.	Long chain fatty acids
MalE.	Maltose binding protein
MBP.	Maltose binding protein
MST	Mass spectral metabolite tag
OPTN.	Organ Procurement and Transplantation Network
ORP.	Oxidation reduction potential
PgSERS.	peptide-guided surface enhanced scattering
PLE.	Pressurized liquid extraction
RDA.	Raman Data Analysis
SPME.	Solid-phase micro extraction
TEM.	Transmission electron microscopy
UPLC.	Ultra-performance liquid chromatography

## **CHAPTER ONE**

# **INTRODUCTION**

### **MOTIVATION**

This work was aimed at applying Raman spectroscopy together with statistical methods as an analytical methodology for continuous monitoring and assessment of phenotypic and physiological changes in both micro (e.g., cellular and sub-cellular) and macro (e.g., tissues and organs) systems in response to environmental stimuli. This methodology has several immediate applications, including understanding (i) the microbial toxicity mechanisms of engineered biofuels and chemicals and (ii) the fate of organs as they are perfused *ex vivo* awaiting transplant.

### **ANALYSIS OF BIOLOGICAL SAMPLES**

Due to their complex nature, biological samples (i.e., macromolecules, cells, tissues, or organs) often require much detailed sample preparations such as extraction of individual components prior to analysis (1). Different approaches have been employed for biological sample analyses depending on the state or form of the samples. For example biological fluids (urine, saliva, gastric juice, plasma) have been analyzed for nitrate via high-pressure cadmium reduction column (2). Gas chromatography-mass spectrometry has been employed largely for metabolite profiling in biological samples (3, 4). However, more than 50% of the metabolites that are covered by GC-MS are currently represented as non-identified mass spectral metabolite tags (MSTs) (2).

The techniques mentioned above though highly efficient, most certainly cannot be employed for real-time analysis. Also these techniques are destructive in that the sample preparation involves disruption of the cell membrane and for pharmaceutical products produced

at high cost, it may be undesirable for use with analytical techniques requiring relatively large sample amount. Also each approach focuses on limited extractable content and rarely gives a holistic data source for each individualized sample. The ability to non-destructively characterize biological phenotypes in real-time will have great implications for advancement in both industrial and clinical microbiology (12).

### ***Motivation for biofuel research***

World energy consumption is projected to increase by 53% between 2008 and 2035 according to the International Energy Outlook 2011 (IEO) (13). To meet this demand, scientists are seeking energy solutions which are both renewable and cost-effective. Biomass is simply organic matter mostly derived from dead material that was once living. For example, kernels of corn, mats of algae, and stalks of sugar cane are all biomass. Biomass is one such natural resource currently being researched due to its abundance and renewable nature (14). Biodiesel and ethanol are currently very competitive energy sources representing approximately 90% of the renewable liquid biofuels on the market (15). Challenges with these biofuel sources (e.g. ethanol), include incompatibility with existing storage and transport infrastructure mainly due to differences in energy content and hygroscopicity (16, 17). Unlike ethanol, 1-butanol has a similar energy content to gasoline (27 vs. 32 MJ/L) making it a preferred candidate for biofuel yield optimization. Current approaches involve the creation of microbial cell factories that are used as bio-refineries for the production of advanced biofuels from non-native producers such as *E. coli* and also *de-novo* synthesis of value-added chemicals [18-20]. Product toxicity to the microbe is a major impediment in this regard (18-20), resulting in yields as low as 1% (v/v) of isobutanol in *E. coli* (21). This challenge with low product yields, presents research interests for investigating host toxicity mechanisms of microbially derived products. However, the major

challenge to understanding solvent toxicity effect on an organism is the ability to characterize the organisms' chemical composition and inherent changes upon solvent exposure opening doors for research in this field.

### ***Argument for organ perfusion***

Like microbes, mammalian cells (organs and tissue) have an even more complex nature where an organism's phenotype is a complex function involving its genotype and constantly changing environmental conditions. To facilitate better diagnosis and care of patients, methods are needed for quick and easy detection and possible arrest of degenerate tissue (22). Real-time diagnosis is essential in critical surgical procedures such as organ transplants. Over a 9-year course (315/yr in 1990 to 2,000/yr in 1999) patients on the liver donor waiting list who have died prior to receiving a donor liver has increased about 6-fold (23). To offset the current mortality rate, methods need to be developed to enable a more objective review of donor organs, which will otherwise be discarded based on subjective review or existing protocols such as a donor's age. The average cost of a single liver transplant is about \$60,000 (23) and it is important to detect any post-surgical issues, such as graft failures, and avert them (24, 25).

### **TRADITIONAL METHODS OF ANALYSES**

Biological samples are traditionally analyzed by methods such as gas-chromatography mass-spectroscopy (GC-MS), liquid-chromatography mass-spectroscopy (LC-MS), nuclear magnetic resonance (NMR) and transmission electron microscopy (TEM). Both methods, however, involve laborious sample preparation and analysis and cannot be performed in real-time. A faster analytical approach, the Fourier transform infrared spectroscopy (FTIR) has the major disadvantage for analyzing biological samples, which is signal interference from water, which constitutes the bulk of biological mass. Analytical methods are thus needed to address

these challenges with sample preparation time, ease of analysis, and ability for data acquisition in near real-time analysis.

## **RAMAN SPECTROSCOPY**

Discovered in 1928 by C.V. Raman, the technique of Raman spectroscopy was largely unexplored until the past decade when there was major improvements to instrumentation, with major feats such as development of the coupled-charge device (CCD) (26). The major initial restrictions to the use of Raman spectroscopy included (i) high cost, (ii) interference from background fluorescence, (iii) low sensitivity, and low (iv) reproducibility, making analysis by infra-red (IR) spectroscopy a preferred method (27, 28) . Together, IR and Raman spectroscopy have been employed as powerful tools for analysis of biological samples acting as complementary techniques. Raman spectroscopy is an optical technique that utilizes molecular-specific, inelastic scattering of light photons to interrogate biological tissues (29, 30) and the signal is derived from molecular backbone structures and bond symmetry. The acquired Raman signal provides information about (i) composition (characteristic peaks), (ii) stress/strain (shift in frequency of peak), (iii) symmetry/orientation (polarization direction), (iv) amount (intensity of peak) and (v) quality (peak width). Other advantages include; (i) minimal or no sample preparation, (ii) sampling directly through glass containers, (iii) non-destructive analysis, which allows for further analyses with the same sample, and (iv) minimal water interference. By virtue of their unique Raman signal, biological molecules such as nucleic acids, proteins, lipids, and carbohydrates can help generate Raman spectral fingerprints of whole cells (31, 32).

## **CHALLENGES WITH RAMAN SPECTROSCOPY**

Surface-enhanced Raman scattering (SERS) is a related technique to Raman spectroscopy and was developed to address problems of low signal intensities with the latter. The SERS principle is based on the fact that particles in close proximity to a roughened metal substrate produce enhanced Raman signals by several orders ( $10^4 - 10^{16}$ ) of magnitude. The development of SERS, though highly useful, has been found to be highly irreproducible due to the random dispersion of the metal nanoparticles used in the technique. The results, a highly convoluted SERS spectra composed of contributions from bio-chemicals of diverse intracellular environments simultaneously (33). To harness the high intensities with SERS, there is the need to develop methods that allow control of the localization process of probes used in the scattering process. A new methodology, the peptide-guided surface enhanced scattering (pgSERS), has been employed in *E. coli* cells, where nanoparticles covalently linked to synthetic peptides functioned as probes to target the outer membrane (33). The revolutionary power with pgSERS was in its ability to deconvolute complex Raman spectra by the action of controlled localization of the SERS probes. To further utilize this technique of controlled dispersion of nanoparticles, molecular biology techniques could allow for *in vivo* assembly of the probes, making the process more cost-effective to synthetic peptide use.

## **HYPOTHESES**

The hypotheses of this research in regards to Raman spectroscopy as a real-time analytical method are that it can (i) detect phenotype changes of microbes upon butanol exposure, (ii) differentiate the response mechanisms of microbes upon exposure to different alcohols with the same carbon number (isomers), (iii) be used in conjunction with pgSERS probes to further

study the structure of different cellular locations in bacteria, and (iv) establish viability indicators from perfusion fluids of porcine organs (liver and heart).

## **DISSERTATION SUMMARY**

The first part of this dissertation (Chapters two and three) focus on phenotype changes of microbes when exposed to different four-carbon alcohols. Chapter two, which deals with exposure to 1-butanol, makes the argument for the use of Raman spectroscopy for real-time analysis by analyzing the same biological samples using various standardized techniques, such as GC-MS, fluorescence anisotropy, total protein assay and Raman spectroscopy. Following the comparative sample analyses, correlations were established for each standardized method in relation to Raman data, with good R values ( $> 0.75$ ). Similar trends were observed in most cases for comparisons of Raman data with (i) GC-MS data, (ii) fluorescence anisotropy (FA) data, and (iii) protein assay data. In the follow up experiment in Chapter three, the Raman experiment was repeated with four other 4-C alcohols; (i) 2-butanol, (ii) isobutanol, (iii) tert-butanol, and (iv) 1,4-butanediol. Having established good correlations previously with 1-butanol toxicity study, and identified ideal peak candidates for individual components, phenotype changes were once more investigated for (i) branching in alcohols and (ii) chain length in alcohols, towards their effects on the phenotypic response of microbes following exposure to the alcohols.

The second part, Chapter four, focuses on real-time analysis of perfused organs using Raman spectroscopy. Different porcine organs (liver, kidney, heart) were perfused *ex vivo* on the newly developed VasoWave<sup>®</sup> system under different experimental conditions. The experimental analysis were performed on six individual livers perfused under three duplicate conditions of time and temperature as follows (i) 110-70 mmHg & 25 C, (ii) 70-30 mmHg & 25 C, and (iii) 110-70 mmHg & 3 C.

Finally, the third part, Chapter five, is devoted to challenges of low sensitivity and convoluted Raman signatures in biological samples. Three different proteins selected exclusively for their target relocation upon release were cloned into *E. coli* DH5- cells under an inducible promoter. The protein sequence was engineered to attach a silver-binding protein (AgBP) tag at the C-terminus capable of binding to silver nanoparticles, which is the basis for SERS. FadL protein (outer membrane), malE protein (periplasm), and aroP protein (cytoplasm) were produced upon the induction from an arabinose inducible promoter and targeted to their corresponding subcellular location, allowing for targeted SERS analysis within microbial cells.

## REFERENCES

1. **Gygi SP, Rist B, Gerber SA, Turecek F, Gelb MH, Aebersold R.** 1999. Quantitative analysis of complex protein mixtures using isotope-coded affinity tags. *Nature biotechnology* **17**:994-999.
2. **Green LC, Wagner DA, Glogowski J, Skipper PL, Wishnok JS, Tannenbaum SR.** 1982. Analysis of nitrate, nitrite, and [<sup>15</sup>N] nitrate in biological fluids. *Analytical biochemistry* **126**:131-138.
3. **Fernie AR, Trethewey RN, Krotzky AJ, Willmitzer L.** 2004. Metabolite profiling: from diagnostics to systems biology. *Nature Reviews Molecular Cell Biology* **5**:763-769.
4. **Lisec J, Schauer N, Kopka J, Willmitzer L, Fernie AR.** 2006. Gas chromatography mass spectrometry-based metabolite profiling in plants. *Nature protocols* **1**:387-396.
5. **Zhang Z, Yang MJ, Pawliszyn J.** 1994. Solid-phase microextraction. A solvent-free alternative for sample preparation. *Analytical chemistry* **66**:844A-853A.
6. **de Fatima Alpendurada M.** 2000. Solid-phase microextraction: a promising technique for sample preparation in environmental analysis. *Journal of Chromatography A* **889**:3-14.
7. **Theodoridis G, Koster Ed, De Jong G.** 2000. Solid-phase microextraction for the analysis of biological samples. *Journal of Chromatography B: Biomedical Sciences and Applications* **745**:49-82.
8. **Han X, Gross RW.** 2003. Global analyses of cellular lipidomes directly from crude extracts of biological samples by ESI mass spectrometry a bridge to lipidomics. *Journal of lipid research* **44**:1071-1079.

9. **Koivusalo M, Haimi P, Heikinheimo L, Kostianen R, Somerharju P.** 2001. Quantitative determination of phospholipid compositions by ESI-MS: effects of acyl chain length, unsaturation, and lipid concentration on instrument response. *Journal of lipid research* **42**:663-672.
10. **Liu C, Hofstadler SA, Bresson JA, Udseth HR, Tsukuda T, Smith RD, Snyder AP.** 1998. On-line dual microdialysis with ESI-MS for direct analysis of complex biological samples and microorganism lysates. *Analytical chemistry* **70**:1797-1801.
11. **Carabias-Martínez R, Rodríguez-Gonzalo E, Revilla-Ruiz P, Hernández-Méndez J.** 2005. Pressurized liquid extraction in the analysis of food and biological samples. *Journal of Chromatography A* **1089**:1-17.
12. **Notingher I.** 2007. Raman spectroscopy cell-based biosensors. *Sensors* **7**:1343-1358.
13. **Administration. USEI.** 2011. International energy outlook 2011. U.S. Department of Energy, Washington, DC.
14. **Colin VL, Rodríguez A, Cristóbal HA.** 2011. The role of synthetic biology in the design of microbial cell factories for biofuel production. *Journal of Biomedicine and Biotechnology* **2011**.
15. **Colin VL, Rodriguez A, Cristobal HA.** 2011. The role of synthetic biology in the design of microbial cell factories for biofuel production. *Journal of biomedicine & biotechnology* **2011**:601834-601843.
16. **Jin C, Yao M, Liu H, Lee C-fF, Ji J.** 2011. Progress in the production and application of n-butanol as a biofuel. *Renewable and Sustainable Energy Reviews* **15**:4080-4106.

17. **Rakopoulos D, Rakopoulos C, Hountalas D, Kakaras E, Giakoumis E, Papagiannakis R.** 2010. Investigation of the performance and emissions of bus engine operating on butanol/diesel fuel blends. *Fuel* **89**:2781-2790.
18. **Atsumi S, Hanai T, Liao JC.** 2008. Non-fermentative pathways for synthesis of branched-chain higher alcohols as biofuels. *Nature* **451**:86-89.
19. **Rutherford BJ, Dahl RH, Price RE, Szmidt HL, Benke PI, Mukhopadhyay A, Keasling JD.** 2010. Functional genomic study of exogenous n-butanol stress in *Escherichia coli*. *Appl Environ Microbiol* **76**:1935-1945.
20. **Dunlop MJ, Dossani ZY, Szmidt HL, Chu HC, Lee TS, Keasling JD, Hadi MZ, Mukhopadhyay A.** 2011. Engineering microbial biofuel tolerance and export using efflux pumps. *Mol Syst Biol* **7**:487.
21. **Brynildsen MP, Liao JC.** 2009. An integrated network approach identifies the isobutanol response network of *Escherichia coli*. *Mol Syst Biol* **5**:277.
22. **Zhang Y, Hong H, Cai W.** 2010. Imaging with Raman spectroscopy. *Current pharmaceutical biotechnology* **11**:654.
23. **Becker GS, Elias JJ.** 2007. Introducing incentives in the market for live and cadaveric organ donations. *The Journal of Economic Perspectives* **21**:3-24.
24. **Lee JH, Hong SY, Oh CK, Hong YS, Yim H.** 2012. Kidney transplantation from a donor following cardiac death supported with extracorporeal membrane oxygenation. *Journal of Korean medical science* **27**:115-119.
25. **Perera MT, Bramhall SR.** 2011. Current status and recent advances of liver transplantation from donation after cardiac death. *World journal of gastrointestinal surgery* **3**:167-176.

26. **Bocklitz T, Walter A, Hartmann K, Rosch P, Popp J.** 2011. How to pre-process Raman spectra for reliable and stable models? *Analytica chimica acta* **704**:47-56.
27. **Nelson W, Manoharan R, Sperry J.** 1992. UV resonance Raman studies of bacteria. *Applied Spectroscopy Reviews* **27**:67-124.
28. **Das RS, Agrawal Y.** 2011. Raman spectroscopy: Recent advancements, techniques and applications. *Vibrational Spectroscopy* **57**:163-176.
29. **Crow P, Stone N, Kendall CA, Uff JS, Farmer JA, Barr H, Wright MP.** 2003. The use of Raman spectroscopy to identify and grade prostatic adenocarcinoma in vitro. *British journal of cancer* **89**:106-108.
30. **Mahadevan-Jansen A, Mitchell MF, Ramanujam N, Malpica A, Thomsen S, Utzinger U, Richards-Kortum R.** 1998. Near-infrared Raman spectroscopy for in vitro detection of cervical precancers. *Photochem Photobiol* **68**:123-132.
31. **Dutta RK, Sharma PK, Pandey AC.** 2009. Surface enhanced Raman spectra of *Escherichia Coli* cell using ZnO nanoparticles. *Dig. J. Nanomater. Biostruct* **4**:83-87.
32. **She C, Dinh N, Tu AT.** 1974. Laser raman scattering of glucosamine *N*-acetylglucosamine, and glucuronic acid. *Biochimica et Biophysica Acta (BBA)-General Subjects* **372**:345-357.
33. **Athamneh AI, Senger RS.** 2012. Peptide-guided surface-enhanced Raman scattering probes for localized cell composition analysis. *Applied and environmental microbiology* **78**:7805-7808.

## CHAPTER TWO

# Near real-time analysis of the phenotypic responses of *Escherichia coli* to 1-butanol exposure using Raman spectroscopy

(Manuscript accepted for publication to the Journal of Bacteriology)

Reprinted with permission from Theresah N. K. Zu, et al., Journal of Bacteriology (JB01590-14R1), 2014.

Theresah N. K. Zu<sup>1</sup>, Ahmad I. M. Athamneh<sup>1</sup>, Robert S. Wallace<sup>1</sup>, Eva Collakova<sup>2</sup>, and Ryan S. Senger<sup>1,#</sup>

<sup>1</sup>Biological Systems Engineering Department; Virginia Tech; Blacksburg, VA 24061

<sup>2</sup>Department of Plant Pathology and Weed Science; Virginia Tech; Blacksburg, VA 24061

#Corresponding author

Corresponding author email address: senger@vt.edu

Running Title: Bacterial phenotyping by Raman spectroscopy

# Near real-time analysis of the phenotypic responses of *Escherichia coli* to 1-butanol exposure using Raman spectroscopy

## ABSTRACT

Raman spectroscopy was used to study the time-course phenotypic responses of *Escherichia coli* (DH5- $\alpha$ ) to 1-butanol exposure (1.2% v/v). Raman spectroscopy is of interest for bacterial phenotyping because it can be performed: (i) in near real-time, (ii) with minimal sample preparation (label-free), and (iii) with minimal spectral interference from water. Traditional off-line analytical methodologies were applied to both 1-butanol treated and control cells to draw correlations with Raman data. Here, distinct sets of Raman bands are presented that characterize phenotypic traits of *E. coli* with maximized correlation to off-line measurements. In addition, the observed time-course phenotypic responses of *E. coli* to 1.2% v/v 1-butanol exposure included: (i) decreased saturated fatty acids levels, (ii) retention of unsaturated fatty acids and low levels of cyclopropane fatty acids, (iii) increased membrane fluidity following the initial response of increased rigidity, and (iv) no changes in total protein content or protein-derived amino acid composition. For most phenotypic traits, correlation coefficients between Raman spectroscopy and traditional off-line analytical approaches exceeded 0.75, and major trends were captured. Results suggest that near real-time Raman spectroscopy is suitable for approximating metabolic and physiological phenotyping of bacterial cells subjected to toxic environmental conditions.

## **INTRODUCTION**

### ***The role of product toxicity in biofuel production by microbes***

The quest for biofuels due to the scarcity and environmental concerns of non-renewable sources is well-established (1-5). In the US, production of 36 billion gallons of renewable fuel will be required by 2022, with about 44% to be obtained from cellulosic ethanol (6). Currently, approximately 90% of the renewable liquid biofuels market is represented by biodiesel and ethanol (5). However, 1-butanol has long been an alternative biofuel of interest. Unlike ethanol, 1-butanol has a similar energy content to gasoline (27 vs. 32 MJ/L), and its hygroscopicity allows for storage and transport with existing infrastructure (7, 8). In addition, advances in synthetic biology and *de novo* metabolic pathway engineering are enabling new routes to 1-butanol and other potential liquid biofuels, such as isobutanol, 2-methyl-1-butanol, alkanes, and fatty alcohols (2, 4, 5, 9-11). The broader approach involves the creation of microbial cell factories that are used as bio-refineries to produce advanced biofuels and value-added chemicals from renewable substrates (2, 12-14). Major obstacles to this approach, however, include product toxicity to the host microbe, ultimately resulting in low yields (3, 13, 15). For example, growth of *Escherichia coli* is arrested at concentrations as low as 1% (v/v) of isobutanol (16). In order to become a viable source for biofuels and chemicals, the host toxicity mechanisms of microbial products must be understood so that rational metabolic engineering strategies can be derived to confer adequate product tolerance and ultimately improve yield.

### ***Microbial toxicity mechanisms of alcohols***

Microbes turn on several genetic programs in response to changing environmental conditions (e.g., alcohol stress) in order to maintain homeostasis and optimize the use of resources (17-20). The cell membrane plays a significant role in the ability of the cell to sense

these changes as well as in the adaptation to stress by counteracting alcohol toxicity (15, 21). Both short (<4 C) and long (>4 C) chain alcohols are known to cause membrane disruption by mechanisms of desiccation (short chain alcohols) or intercalation (long chain alcohols) of lipophilic side chains into the membrane lipid bilayer (15, 16, 22). In general, increased membrane fluidity has been observed as a result of 1-butanol exposure for both *E. coli* and the natural 1-butanol-producer *Clostridium acetobutylicum* (23-26). This fluidizing effect has been proposed to result from several host response mechanisms including: (i) altered ratio of saturated to unsaturated fatty acids in the cell membrane (27), (ii) denatured protein structure and changed cell surface protein composition (26, 28), (iii) increased use of efflux pumps in several Gram-negative bacteria (17), (iv) disrupted protein-lipid interactions (25), (v) up-regulated synthesis of other protective metabolites and macromolecules (26, 28), and (vi) decreased central carbon metabolic activity by inhibition of glucose and nutrient transport (16, 21, 26, 28, 29). The general consensus is that long chain alcohols have the ability to intercalate further into the membrane lipid bilayer and disrupt hydrogen bonding between hydrophobic tails, causing relatively more toxicity than short chain alcohols (15, 23, 27, 30). However, this proposed mechanism does not always hold true for 1-butanol, for which toxicity appears to be strain dependent (31).

Major factors found to influence alcohol toxicity include: (i) solvent hydrophobicity, (ii) octanol-water partition coefficient ( $K_{ow}$ ), (iii) length of alkyl chain, and (iv) degree of saturation (15). Organic solvents with log  $K_{ow}$  values between 1.5 and 5.0 have been found to be extremely toxic to microbes, as they preferentially partition the cytoplasmic membrane by disorganizing structure and function (e.g., loss of ions, metabolites, lipids, protein, etc.), which leads invariably to cell lysis and death (27). The effect of alcohol on microbial cell membrane fluidity has also been studied widely (23, 30, 32, 33). It has been observed that *E. coli* responds to ethanol

exposure with an initial alteration of fatty acid composition as a short-term response allowing for *de novo* biosynthesis of membrane components as a permanent and long-term response (23, 27, 34, 35). A net increase in total protein from cells exposed to growth inhibitory levels of ethanol has also been observed (34). Commonly, biological studies of the phenotypic response to alcohol toxicity have been carried out using genetic and biochemical approaches that make use of standardized procedures such as thin-layer chromatography (TLC) (36) and gas chromatography-mass spectrometry (GC-MS) (36, 37). By nature, these methods require lipid extraction (cell destruction) and extensive sample preparation. While these methods have proven reliable, the time required for analysis is on the order of hours to days. Real-time methods of analysis are needed to further understand the dynamics of the microbial phenotypic responses to alcohol toxicity. With this information, it is likely that metabolic engineering and process control strategies can be developed to confer product tolerance and optimize cell productivity.

### ***Monitoring dynamic phenotypes with Raman spectroscopy***

Raman spectroscopy is a powerful analytical technique that can be applied to a wide variety of solid, liquid, and gas samples, including biological tissues (38-41). The sample is excited by a monochromatic laser, and the resulting spectrum shows the intensity of Raman scattered radiation (arising from chemical bond rotations, stretching, and bending) as a function of frequency (42). The Raman spectrum of a biological sample is usually complex and contains bands (i.e., peaks) that result from the thousands (or more) of molecules comprising the sample, each having its own specific Raman signature. Biological sample analysis by Raman spectroscopy can be performed on dried or liquid samples. Raman scanning of dried samples currently returns more reliable data than scanning liquid samples and has the significant advantages of: (i) sample preparation is minimal (involves drying microliters of sample on a

metal surface) and label-free, (ii) Raman data is returned in near real-time, and (iii) there is minimal spectral interference from water. Liquid phase scanning of bacterial cultures remains a topic of research and offers the additional advantages of: (iv) scanning directly through glass containers (enabling near real-time *in situ* analysis of living cultures) and (v) being non-destructive in nature, enabling continued single cell monitoring. By virtue of their unique Raman signals, biological molecules such as nucleic acids, proteins, lipids, and carbohydrates can also be used to generate fingerprints of whole cells (43, 44).

One of the challenges working with Raman data is the assignment of chemical species to spectral bands. Due to the complex nature of biological samples, most Raman bands result from the overlapping bands of several individual molecules. Researchers have often relied on literature sources for Raman band identification; however, (i) the interpretation of spectral data differs significantly among the various sources and (ii) band assignment remains ambiguous, as a single Raman band can have several assignments (42, 45, 46). Recently, a Raman database was published that reports the band assignments for several individual biological molecules (42). Though useful, expert user input is still required for accurate band assignments. For example, different band assignments (980, 1443, 1447, 1449, 1655 – 1680, 1656, 2883, 2900, 2915, and 2940  $\text{cm}^{-1}$ ) were reported for both proteins and lipids. De-convolution of a set of Raman spectra to obtain chemical composition information is not trivial and represents a unique challenge. With advancement in this area, Raman spectroscopy will ultimately be useful as a means of obtaining chemical composition data for biological samples in near real-time without disrupting the system.

### ***Studying the response of E. coli to 1-butanol exposure using Raman spectroscopy***

The practical use of Raman spectroscopy is demonstrated in this research as an analytical method for studying the phenotypic responses of *E. coli* cell to growth inhibitory 1-butanol exposure. Traditional methods of analysis including: (i) GC coupled with flame ionization detection (FID) and MS, (ii) ultra-performance liquid chromatography (UPLC), and (iii) fluorescence anisotropy were used to elucidate the 1-butanol toxicity responses of *E. coli*. By correlating these measurements with specific Raman bands, a methodology was developed that can monitor changing phenotypes and cell chemical composition in near real-time. Also, Raman bands were identified that characterize the fluidizing effect of 1-butanol on the *E. coli* cell membrane, thus connecting molecular changes to measurable physiological phenotypes. The use of Raman spectroscopy to monitor culture phenotypes is advantageous as it is relatively fast and non-invasive, unlike traditional analysis methods, which are both resource- and time-intensive. The methods described in this research have potentially wide-reaching applications for industrial and clinical microbiology; however, the Raman band assignments reported in this research should be considered valid for *E. coli* only until larger-scale studies are completed.

## **MATERIALS AND METHODS**

### ***Bacteria strain***

*E. coli* DH5- $\alpha$  cells were obtained from Invitrogen Life Technologies (Grand Island, NY) and used in all experiments. Frozen cells were stored as glycerol stocks at -80°C and were thawed and plated onto solid agar plates to select a single colony for experiments in liquid culture media.

### ***Chemicals and reagents***

All chemicals and reagents (1-butanol, methanol, chloroform, ethanol, 1 N methanolic HCl, borate buffer, yeast extract, tryptone, sodium chloride, *cis*-9, *cis*-12-octadecadienoic acid

(C18:2)) were purchased from Sigma-Aldrich (St. Louis, MO) or included as part of a kit. The *cis*-9, *cis*-12-octadecadienoic acid (C18:2) was used as an internal standard to account for losses during GC analysis of fatty acids as fatty acid methyl esters (FAMES). It was chosen because *E. coli* does not produce it natively. All solvents used for extractions were LC or GC grade.

### ***Culture media, growth conditions, and harvesting***

Overnight cultures were prepared by inoculating 15 mL liquid Luria-Burtani (LB) growth media with *E. coli* cells from a solid agar plate. Cultures were placed in an incubator with a rotary shaker set to 210 rpm and 37°C. For solid LB media, agar was used at 15g/L. Cell growth in liquid media was monitored by optical density measured at 600 nm (OD<sub>600</sub>). An aliquot sample was then used to prepare a subculture by diluting 10 mL of cell culture with 1 L fresh LB media in a sterilized culture flask. The culture was then grown to the start of the exponential growth phase (OD<sub>600</sub> of 0.4 – 0.5). At this point, the culture was split into two equal portions (~500 mL each), with one serving as the negative control. 1-Butanol was added to the experimental culture to a concentration of 1.2% v/v, and both cultures were incubated at 210 rpm and 37°C for 1 h prior to sampling. Sample volumes of 50 mL (for FAME analysis), 5 mL (for membrane leakage analysis), 1 mL (for cell viability analysis), and 1 mL (for analysis by Raman spectroscopy) were taken every half-hour from both cultures until a constant OD<sub>600</sub> reading was observed. Cells were harvested following centrifugation at 10,000 rpm at 4°C for 5 min. Cells were washed with ice-cold purified water (except those for membrane leakage analysis), and this procedure was repeated. Cells for Raman analysis were re-suspended in 1 mL of Type I purified water for analysis. Cells for FAME and metabolite analyses were frozen in liquid nitrogen and lyophilized.

### ***Raman spectroscopy***

To prepare samples for Raman analysis, 2  $\mu\text{L}$  of washed cells were dried on an aluminum surface at room temperature. Dried cells were analyzed using a Bruker Senterra dispersive Raman spectrometer equipped with a confocal microscope and objective lens of 100x magnification (Bruker Optics, Billerica, MA). Measurements were carried out using laser excitation of 532 nm (20 mW) for 25 seconds with spectral resolution of 9-15  $\text{cm}^{-1}$ . A similar method has been published (47). A minimum of 50 individual spectra was acquired per sample prior to data analysis. Software enabling data collection as well as data normalization and processing are discussed in the next section.

### ***Raman data processing***

Raman data was processed and analyzed using two different software platforms: (i) OPUS (Bruker Optics, Billerica, MA) and (ii) MATLAB (R2012A) (MathWorks, Natick, MA) using a custom Raman Data Analysis (RDA) Toolbox (manuscript under-review) containing functions for comparative peak analysis and multivariate statistics. The OPUS platform allowed for interaction with the Raman instrument and provided initial baseline correction of spectra. Raman spectra of biological samples are commonly corrupted by the influence of (i) background fluorescence, (ii) charge-coupled device background noise, (iii) Gaussian noise, and (iv) cosmic spikes (40). During acquisition, spectra with cosmic spikes were identified through manual inspection and discarded. The following spectra analysis was performed in MATLAB. The RDA Toolbox provided a more convenient graphical user interface, but it was not essential for this analysis. For consistency, data from all spectra (i.e., intensities at all wavenumbers) were normalized using vector normalization over the entire spectral range (300  $\text{cm}^{-1}$  – 3600  $\text{cm}^{-1}$ ). In vector normalization, the signal intensity at each wavenumber (i.e., band) was divided by the

norm of the spectrum intensities. This allowed intensities from several spectra to be compared directly. Thus, only the vector normalized intensities of specified bands were used for comparisons throughout.

#### ***Fatty acid analysis by GC-MS/FID***

Lipid extractions were performed on 1 mg of lyophilized cells by using biphasic chloroform/methanol/water extractions and 10 µg of C18:2 as an internal standard, according to standard protocol (48). Fatty acid methyl esters were prepared by trans esterification in the presence of methanolic HCl and analyzed on an Agilent 7890A series GC equipped with an FID (Agilent Technologies, Santa Clara, CA). The FAME separation was achieved on an Agilent 30-m DB-23 column (0.25 mm x 0.25 µm) and the identity of the individual fatty acids was confirmed by analyzing spectral information of FAME in selected samples on the same GC instrument coupled to an Agilent 5975C series MS (Agilent Technologies) (48).

#### ***Total protein content, protein hydrolysis and amino acid analysis by UPLC***

The total protein content of 1-butanol exposed and control cultures was determined by Coomassie Plus<sup>TM</sup> (Bradford) assay (Thermo Fisher Scientific, Rockford, IL) according to the manufacturer's protocol. Proteins and free metabolites are contained in the aqueous phase and insoluble pellet remaining after the removal and re-extraction of lipids used in FAME analysis. It was found that free amino acids are present at very low levels in *E. coli* cells and do not interfere with the analysis of protein-derived amino acids, so there was no need to separate proteins by acidic precipitation from the rest of the polar metabolites present in the aqueous phase. Because some proteins are not soluble in water and are present in the insoluble pellet, total protein hydrolysis was performed in the same tube as the extraction. The solvents (water and methanol) were dried and proteins hydrolyzed under vacuum at 110°C for at least 16 h in a

custom-made Teflon hydrolysis chamber containing 4 mL of 6N HCl. The resulting protein-derived amino acids were dissolved in 1 mL of water and 1  $\mu$ L of sample was derivatized in a 50  $\mu$ L total volume using the AccQ•Tag Ultra Amino Acid kit according to the manufacturer's recommendations (Waters Corporation, Milford, MA). The derivatized amino acid samples (0.5  $\mu$ L) were injected on an H-class Acquity UPLC and detected by fluorescence as described for analysis of protein hydrolysates (Waters Corporation, Milford, MA).

### ***Membrane fluidity***

Changes in membrane fluidity induced by 1-butanol were monitored by analyzing fluorescence anisotropy from *E. coli* cells labeled with the membrane probe 1,3-diphenyl-1,3,5-hexatriene (DPH), as described previously (49, 50). Stock 8 mM DPH solution in tetrahydrofuran was diluted 1000-fold in vigorously stirred 50 mM NaCl (50). The dispersion was mixed 1:1 with *E. coli* cells, washed three times with chilled phosphate buffered saline (pH 7.4), and re-suspended to an OD<sub>600</sub> of 4.0. Fluorescence anisotropy was measured at room temperature using a SpectraMax M5 plate reader (Molecular Devices, Sunnyvale, CA) using excitation and emission wavelengths of 360 and 428 nm, respectively. Background fluorescence from DPH-free *E. coli* cells was measured and subtracted from the DPH-labeled samples. The fluorescence anisotropy ( $r$ ) of a fluorescent probe is inversely proportional to cell membrane fluidity, as defined in Eq. 1.

$$r = \frac{I_{vv} - I_{vh}}{I_{vv} + 2I_{vh}} \quad (1)$$

Here,  $I_{vv}$  and  $I_{vh}$  represent fluorescence intensities measured through a polarizer oriented parallel and perpendicular, respectively, to the plane of polarization of the excitation beam (50). Fluorescence anisotropy results for 1-butanol treated cultures are presented as a percent change from control (i.e., un-treated) cultures (49).

## RESULTS

### *Raman spectroscopy of growing and growth inhibited cells*

The baseline corrected and vector normalized Raman spectra for *E. coli* cells at the start of 1.2% v/v 1-butanol treatment (time = 0 min) and at the end of the experiment (time = 180 min) for both the 1-butanol treated and control (untreated) cells are shown in Fig. 1. The three spectra were superimposed to show potential differences in the biologically relevant spectral region (600-1800  $\text{cm}^{-1}$ ) (Fig. 1a) and the CH region (2800-3100  $\text{cm}^{-1}$ ) (Fig. 1b) (40). No significant changes were noted in the CH region (Fig. 1b). However, noticeable signal intensities were observed (without the use of statistical analyses) in Fig. 1a for bands assigned to: (i) phosphodiester bonds in DNA ( $\sim 788 \text{ cm}^{-1}$ ) and in RNA ( $\sim 813 \text{ cm}^{-1}$ ) (indicative of nucleic acids) (42, 46); (ii) symmetric  $\text{PO}_2^-$  stretching of DNA ( $\sim 1070 - 1090 \text{ cm}^{-1}$ ) (indicative of nucleic acids); (iii) C-C chain stretch ( $\sim 1060 - 1075 \text{ cm}^{-1}$ ) (indicative of fatty acids) (45, 46); (iv) amide III bands, =CH bend, and nucleic acid bases (1220 – 1284  $\text{cm}^{-1}$ ) (indicative of proteins, lipids, and nucleic acids) (42, 51); (v) C-H deformation and guanine ( $\sim 1320 \text{ cm}^{-1}$ ) (indicative of lipids and nucleic acids) (42, 45, 46); (vi) C-H vibrations ( $\sim 1449 \text{ cm}^{-1}$ ) (indicative of proteins, lipids, and nucleic acids) (42, 46); and (vii) C=C bands ( $\sim 1607 \text{ cm}^{-1}$ ) (indicative of aromatics and unsaturated lipids) (42, 46).

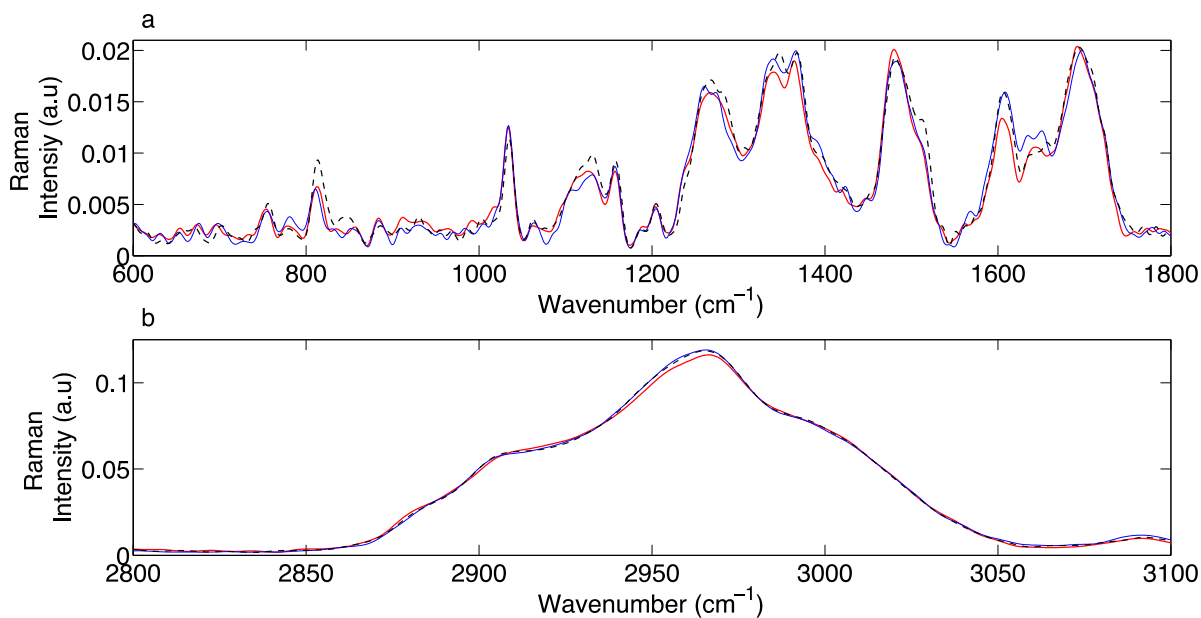


**Figure 1.** Raman spectra of (a) the biological region (600-1800 cm<sup>-1</sup>) and (b) the CH region (2800-3100 cm<sup>-1</sup>) at time equal to 0 min (before the application of 1-butanol) (solid heavy red line), time equal to 180 min for the control cells (solid thin blue line), and time equal to 180 min after treatment for the 1-butanol treated cells (dashed black line).

Significant changes in Raman spectra were observed between the 1-butanol treated and control cells with both time and treatment. Thus, Raman spectroscopy results suggest that cellular chemical composition and physiology changed significantly in response to both factors. The standard deviation of the averaged spectra (not shown in Fig. 1) was found to be very close to zero, confirming high reproducibility of scans.

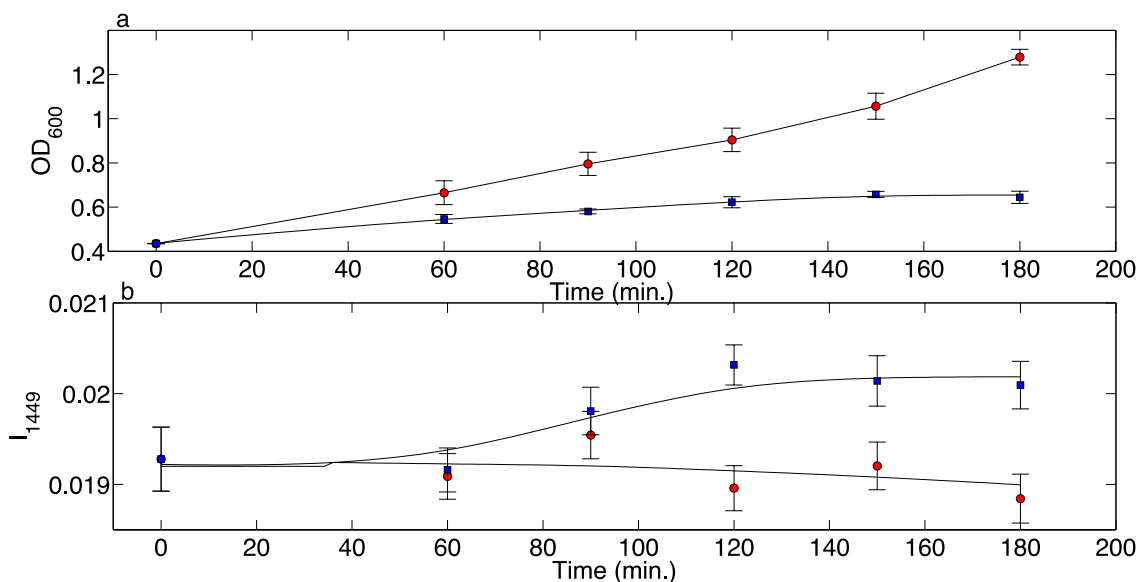


**Figure 2.** (a) Culture growth (OD<sub>600</sub>) and (b) Raman (I<sub>1449</sub>) measure of broader metabolic activity as functions of time for 1-butanol treated cells (blue squares) and control cells (red circles). 1-Butanol (1.2% v/v) was added to the treated cells at 0 min. Error bars represent 1 standard deviation among at least 3 biological replicates.

The time-course OD<sub>600</sub> measurements for both 1-butanol treated and control cultures are shown in Fig. 2a. Upon exposure to 1.2% v/v 1-butanol, *E. coli* cells showed arrested cell growth over time, consistent with expected toxicity responses. The Raman signal intensity at 1449 cm<sup>-1</sup> (I<sub>1449</sub>) over the time-course is shown in Fig. 2b. The Raman band at 1449 cm<sup>-1</sup> corresponds to C-H vibrations (42), which are abundant in all biomass components (e.g., lipids, proteins, nucleic acids, carbohydrates, etc.) of bacterial cells. The Raman signal intensity at 1449 cm<sup>-1</sup> can provide insight into the overall metabolic activity of the cells.

As seen in Fig. 2b, the Raman signal intensity at  $1449\text{ cm}^{-1}$  increased with 1-butanol exposure. This suggests the cells may have up-regulated several metabolic programs (i.e., a toxicity response) with 1-butanol treatment. Because Raman spectra were normalized, an increase in  $I_{1449}$  suggests that the number of molecules exhibiting C-H vibration signals (e.g., lipids, proteins, etc.) has increased per cell. This is also consistent with the increased nucleotide abundances (per cell) noted at  $788\text{ cm}^{-1}$  and  $813\text{ cm}^{-1}$ . Thus, with 1-butanol exposure, it is likely that metabolic activity shifts from growth-related functions to toxicity response programs for survival. The following analyses are aimed at identifying the changes in cell composition and phenotype brought on by these metabolic programs.

The Raman signal intensities for both 1-butanol treated and control cells were investigated for potential candidate bands that could explain the observed physiological changes. The current methodology for determining chemical composition of cells includes several off-line analytical measurements. These often involve long sample preparations, and analyses cannot be performed in real-time. In order to establish a new near real-time analysis protocol using Raman spectroscopy, it was necessary to correlate Raman results with the existing well-established methodologies. In this approach, correlations were determined by calculating the correlation coefficient (R) between time-course Raman signal intensities and off-line experimental measurements. Often, multiple Raman band assignments exist in the literature for a single phenotypic trait (e.g., unsaturated fatty acids content). The goal of this research was to determine the Raman band assignment(s) that best correlate with experimental measurements.

### ***Correlation of Raman spectroscopy and GC-FID for fatty acids analysis***

Time-course Raman signal intensities (at assigned bands taken from the literature (42, 45, 46, 52-54)) were correlated with the corresponding changes in membrane-derived fatty acid

levels and composition, determined by GC-FID. Correlation coefficients (R values) between these two methods are presented in Supplementary Table 1. Several, but not all, of the previously assigned Raman bands from the literature showed correlation with the actual changes in the composition of different fatty acid types. While GC-FID provides quantification of absolute levels of the individual fatty acids, Raman enabled the identification of three different classes of fatty acids that have great relevance to changes in membrane physical properties: (i) saturated, (ii) unsaturated, and (iii) cyclopropane fatty acids. From the results in Supplementary Table 1, Raman bands for saturated fatty acids ( $I_{2870}$ ) (i.e., the Raman signal intensity at  $2870\text{ cm}^{-1}$ ), unsaturated fatty acids ( $I_{1263}$ ), and cyclopropane fatty acids ( $I_{1554}$ ) showed high correlations with results obtained by GC-FID.

The correlation coefficients between Raman spectroscopy and GC-FID data were 0.78, 0.76, and 0.79, respectively. Time-course (over 180 minutes) Raman and FAME analysis data were plotted for both 1-butanol treated and control cells, and results are shown in Fig. 3. In general, the trends were conserved in all three cases; however, it was obvious that GC-FID analyses produced data with less experimental error and better-defined trends over the time-course. Relative to the control, the 1-butanol treated cells (i) produced fewer saturated fatty acids (Fig. 3a), (ii) conserved the presence of unsaturated fatty acids (Fig. 3b), and (iii) largely resisted the formation of cyclopropane fatty acids over the time-course (Fig. 3c). On the other hand, the untreated control cells reduced the amount of unsaturated fatty acids by about 75% over the time-course in favor of saturated fatty acids (~20% increase) and cyclopropane fatty acids (~250% increase). In summary, the dynamics of fatty acid composition were resolved well by GC-FID and were approximated with correlation coefficient levels greater than 0.75 using Raman

spectroscopy. While some accuracy is sacrificed with Raman measurements, results can be obtained in near real-time in a non-disruptive manner.

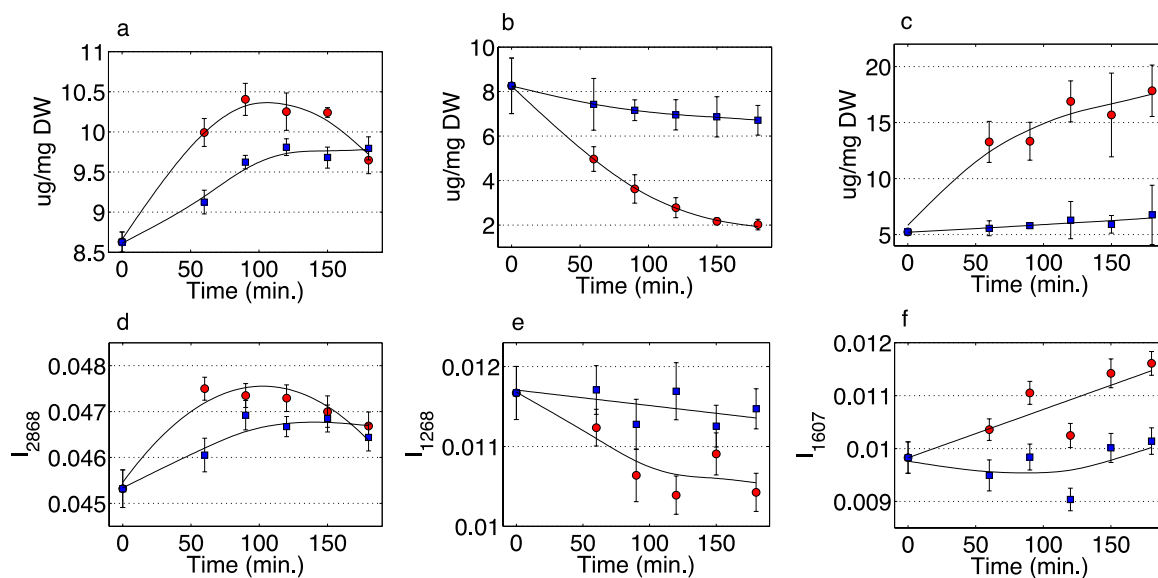


**Figure 3.** (a) Saturated fatty acids measured by GC-FID, (b) unsaturated fatty acids measured by GC-FID, (c) cyclopropane fatty acids measured by GC-FID, (d) saturated fatty acids measured by Raman (I2870), (e) unsaturated fatty acids measured by Raman (I1263), (f) cyclopropane fatty acids measured by Raman (I1554) as functions of time for 1-butanol treated cells (blue squares) and control cells (red circles). 1-Butanol (1.2% v/v) was added to the treated cells at 0 min. Error bars represent 1 standard deviation among at least 3 biological replicates.

### *Correlation of Raman spectroscopy and UPLC for amino acids analysis*

Total amino acid content and composition did not change in the control and 1-butanol treated cultures over the time-course when measured by UPLC. The steady-state levels of total amino acids are shown in Table 1. However, different amounts of each amino acid were observed, and these relative abundances remained constant in all samples. The same was observed when total protein was measured (Fig. 4). Raman band intensities (using previously

published bands for individual amino acids) were correlated with experimental UPLC measurements. In the literature (55, 56), between 9 and 29 distinct Raman bands (with medium to strong intensities) were cited for each amino acid (given in Supplementary Table 2). A unique set of Raman bands (one band for each amino acid) was identified computationally to fully characterize the amino acid composition of *E. coli* to be consistent with UPLC experimental results and published literature values (Table 1).

**Table 1.** Amino acid composition determined by Raman spectroscopy with an optimized set of bands and UPLC. The published amino acids composition of *E. coli* protein is also given.

<b>Amino Acids</b>	<b>Optimum Raman Bands (cm<sup>-1</sup>)</b>	<b>Amino Acid Composition Determined by Raman</b>	<b>Amino Acid Composition Determined by UPLC</b>	<b>Published Amino Acid Composition</b>
Ala	1308	0.111	0.111	0.0960
Arg	1199	0.0246	0.0339	0.0553
Asp/Asn	1695	0.0641	0.0898	0.0901
Cys	678	0.0124	0.0164*	0.0164
Glu/Gln	1319	0.108	0.0916	0.0984
Gly	1332	0.113	0.120	0.115
His	731	0.0216	0.00890	0.0177
Ile	1309	0.111	0.0876	0.0543
Leu	1243	0.0967	0.114	0.0842
Lys	1072	0.0344	0.0524	0.0641
Met	765	0.0114	0.00467	0.0287
Phe	1214	0.0578	0.0459	0.0346
Pro	843	0.00727	0.0102	0.0413
Ser	1010	0.0437	0.0442	0.0403
Thr	1116	0.0338	0.0626	0.0474
Trp	759	0.0141	0.0106*	0.0106
Tyr	798	0.0170	0.00390	0.0258
Val	1454	0.117	0.0922	0.0791
Sum	-	1	1	1

\* Values for Cys and Trp could not be resolved by the UPLC method. The published literature values were used for these cases.

\*\* Amino acid composition is defined as the fraction of each amino acid in *E. coli* total protein.

Given the large number of possible Raman bands per amino acid,  $1.4 \times 10^{21}$  possible band combinations exist. A set leading to good correlation with UPLC-derived data ( $R = 0.93$ ) was identified after examining  $5 \times 10^9$  possibilities in a stochastic simulation. The (i) optimum set of Raman bands, (ii) amino acid composition determined by Raman, (iii) amino acid composition determined by UPLC, and (iv) published amino acid composition (55) are given in Table 1. Good correlation was observed between Raman spectroscopy, UPLC, and published data suggesting that Raman spectroscopy may be used as a near real-time analytical method for determining total amino acid compositions of *E. coli* cells. Among the Raman band assignments listed in Table 1, the assignments for Ala ( $1308 \text{ cm}^{-1}$ ) and Ile ( $1309 \text{ cm}^{-1}$ ) overlap and result in the same amino acid composition values when determined by Raman spectroscopy. In addition, Trp ( $759 \text{ cm}^{-1}$ ) and Met ( $765 \text{ cm}^{-1}$ ) are also close to having overlapping bands. Thus, additional sets of amino acids band assignment solutions have been included in Supplementary Tables 3-5. Each of these band assignment solutions represents a different alternative that can be employed if specific amino acids are of critical interest. However, the band assignment set in Table 1 returned the overall optimum solution.

### ***Correlation of Raman spectroscopy and fluorescence anisotropy for cell membrane fluidity analysis***

Membrane fluidity has long been used to assess the effect(s) of solvents on the microbial cell membranes (15, 21, 23, 27), and membrane fluidity has been observed to increase in *E. coli* cells upon 1-butanol exposure (23). Previous research has also closely tied cell membrane fluidity with changes in fluorescence anisotropy (21, 23, 54). Experimental fluorescence anisotropy results obtained in this research are in agreement with this observation. However, an initial decrease in fluorescence anisotropy was observed before a short “lag” phase followed by

an increase long-term response. These results are shown in Fig. 4a. The molecular mechanisms behind this initial decrease and lag are unknown and remain a topic for further investigation. To assess membrane fluidity using Raman spectroscopy, three signal intensity ratios ( $I_{2870}/I_{2954}$ ,  $I_{2850}/I_{2880}$ , and  $I_{2852}/I_{2924}$ ) were analyzed based on previously published results (53, 54, 57, 58). The identification of Raman peaks corresponding to symmetric and asymmetric stretching of cell membranes was used to derive these ratios. In all three cases examined in this research, the signature decrease, lag, and the eventual increase in signal were observed. In addition, the  $I_{2852}/I_{2924}$  Raman signal intensity ratio was found to best correlate with fluorescence anisotropy results. The percent changes in fluorescence anisotropy between 1-butanol treated and control cells over the time-course are shown in Fig. 4a, and the percent change between  $I_{2852}/I_{2924}$  between 1-butanol treated and control cells is shown in Fig. 4c. While a perfect correlation was not observed, a strong resemblance in general trend was observed between changes in Raman peak intensities obtained in near real-time and off-line fluorescence anisotropy measurements. To determine if total cell protein was involved in the observed changes in membrane fluidity, the total cell protein content measured; no change was detected (Fig. 4b). These results corresponded with the Raman  $I_{2954}$ , as cited in the literature (54).

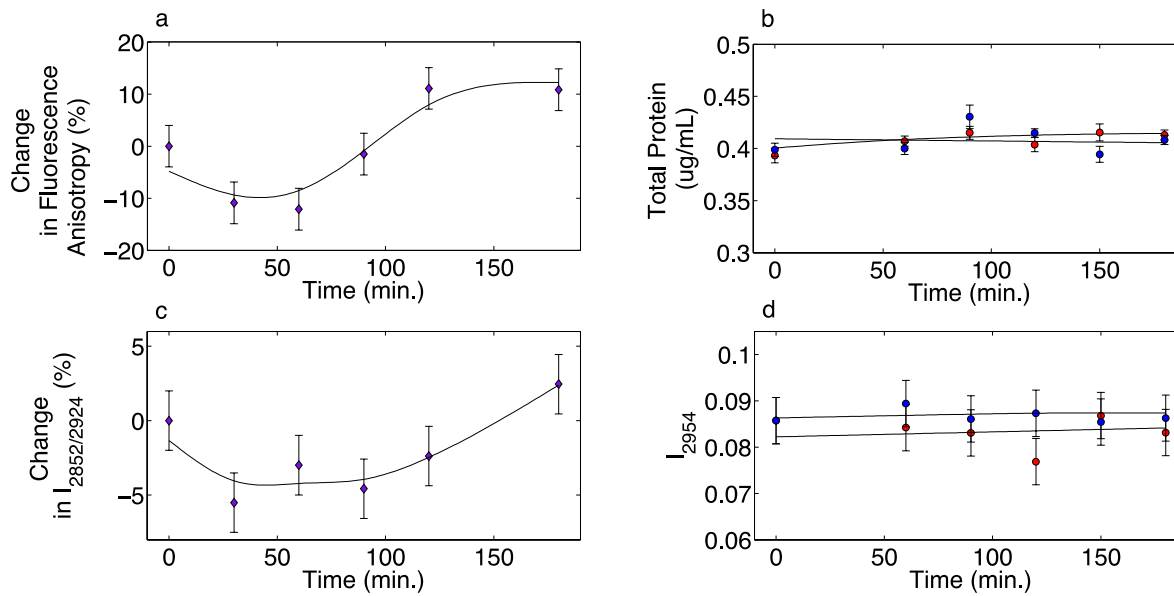


**Figure 4.** (a) Change in fluorescence anisotropy (%) for 1-butanol treated cells relative to the control cells, (b) experimentally measured total protein content, (c) membrane fluidity ( $I_{2852/2924}$ ) measured by Raman, and (d) total protein content measured by Raman ( $I_{2954}$ ) as functions of time for 1-butanol treated cells (blue circles), control cells (red circles), and percent change between 1-butanol treated and control cells (blue diamonds). 1-Butanol (1.2% v/v) was added to the treated cells at 0 min. Error bars represent 1 standard deviation among at least 3 biological replicates.

## DISCUSSION

### *Use of Raman spectroscopy to study cell physiology in near real-time*

In this research, the applicability of Raman spectroscopy for studying *E. coli* cell physiology and chemical composition in near real-time was demonstrated. It has been documented previously that upon exposure to solvents, bacteria initiate response mechanisms to revert induced physiological changes (17, 26). In bacteria, the physiological responses upon

alcohol exposure are often measured by (i) quantifying the fluidizing effects on the cell membrane and (ii) measuring the degree of saturation of membrane lipids. 1-Butanol exposure has been found to result in increased membrane fluidity of *E. coli* (23, 26). This observed increase has been shown to be a result of disruptions in fatty acid and protein structure of the cell membrane, which also affects protein-lipid interactions (26, 59). In the analysis presented here, exposure of *E. coli* to 1-butanol resulted in an increased level of saturated fatty acids, while maintaining a relatively constant level of unsaturated fatty acids. Low levels of cyclopropane fatty acids were also observed with 1-butanol exposure. These trends were first measured by established GC-FID methodology, and Raman bands were identified that showed good correlation with these results. In addition to fatty acid content, Raman bands were justified that showed good correlation with (i) cellular amino acid composition, (ii) fluorescence anisotropy (a measure of membrane fluidity), and (iii) total protein content of the cell. While “perfect” correlations were not identified in this research, several strong correlations were found, indicating that Raman spectroscopy can be successfully and reliably used as a diagnostic tool that has the distinct advantage of offering near real-time analyses. However, superior accuracy was obtained from elaborate standard methods of analysis.

### ***Peak assignment observations and discrepancies***

The main objective of this research was to further develop Raman spectroscopy as a near real-time measurement tool for a quick, reliable diagnosis of changes in metabolic and physiological phenotypes. Currently, researchers commonly rely on published Raman band assignments. However, band selection can be a daunting task as assignments are not always consistent within the published literature. Several published studies have compiled useful databases of band assignments for biological samples; however, questions regarding band

selection remain since assignments of the same molecule/group are often made to several Raman bands. In addition, current reported assignments do not differentiate between cyclopropane fatty acids and saturated fatty acids. To provide additional experimental evidence to select among the several Raman band assignments related to fatty acids, correlations were found among saturated, unsaturated, and cyclopropane fatty acids. Raman spectroscopy was found to be able to capture the induced variances due to 1-butanol treatment and bacterial cell development over time. Currently, the Raman band assignments identified in this research are limited to *E. coli*, and similar studies can be performed to establish useful sets of bands for other organisms. Ultimately, the goal of establishing a set of universally applied Raman bands will require a large-scale study involving several different organisms and treatments.

### ***Potential applications***

The applications of real-time analysis of biological samples with Raman spectroscopy are numerous, and the method is capable of delivering near real-time phenotyping. The results of this research demonstrate the power of Raman for phenotypic profiling of *E. coli* cells. As with the application of 1-butanol exposure in this research, Raman spectroscopy can be used to monitor cell culture responses to metabolically engineered products and be used to signal culture toxicity or even identify optimally productive cell states. In addition, real-time phenotypic monitoring has tremendous application to the field of biosensing, as cell composition changes may be observed in response to small quantities of environmental toxins as well as chemical or biological warfare agents. Future research will determine whether phenotypic profiling can exceed the sensitivity of novel methods, such as surface enhanced Raman spectroscopy of a sample directly.

## REFERENCES

1. **Lennen RM, Braden DJ, West RA, Dumesic JA, Pfleger BF.** 2010. A process for microbial hydrocarbon synthesis: Overproduction of fatty acids in *Escherichia coli* and catalytic conversion to alkanes. *Biotechnology and bioengineering* **106**:193-202.
2. **Atsumi S, Cann AF, Connor MR, Shen CR, Smith KM, Brynildsen MP, Chou KJ, Hanai T, Liao JC.** 2008. Metabolic engineering of *Escherichia coli* for 1-butanol production. *Metabolic engineering* **10**:305-311.
3. **Atsumi S, Hanai T, Liao JC.** 2008. Non-fermentative pathways for synthesis of branched-chain higher alcohols as biofuels. *Nature* **451**:86-89.
4. **Peralta-Yahya PP, Keasling JD.** 2010. Advanced biofuel production in microbes. *Biotechnology journal* **5**:147-162.
5. **Colin VL, Rodriguez A, Cristobal HA.** 2011. The role of synthetic biology in the design of microbial cell factories for biofuel production. *Journal of biomedicine & biotechnology* **2011**:601834-601843.
6. **Sissine F.** 2007.
7. **Jin C, Yao M, Liu H, Lee C-fF, Ji J.** 2011. Progress in the production and application of n-butanol as a biofuel. *Renewable and Sustainable Energy Reviews* **15**:4080-4106.
8. **Rakopoulos D, Rakopoulos C, Hountalas D, Kakaras E, Giakoumis E, Papagiannakis R.** 2010. Investigation of the performance and emissions of bus engine operating on butanol/diesel fuel blends. *Fuel* **89**:2781-2790.
9. **Connor MR, Atsumi S.** 2010. Synthetic biology guides biofuel production. *J Biomed Biotechnol* **2010**.

10. **Dellomonaco C, Fava F, Gonzalez R.** 2010. The path to next generation biofuels: successes and challenges in the era of synthetic biology. *Microb Cell Fact* **9**.
11. **Lee SK, Chou H, Ham TS, Lee TS, Keasling JD.** 2008. Metabolic engineering of microorganisms for biofuels production: from bugs to synthetic biology to fuels. *Curr Opin Biotechnol* **19**:556-563.
12. **Moon TS, Yoon SH, Lanza AM, Roy-Mayhew JD, Prather KL.** 2009. Production of glucaric acid from a synthetic pathway in recombinant *Escherichia coli*. *Applied and environmental microbiology* **75**:589-595.
13. **Dunlop MJ, Dossani ZY, Szmidt HL, Chu HC, Lee TS, Keasling JD, Hadi MZ, Mukhopadhyay A.** 2011. Engineering microbial biofuel tolerance and export using efflux pumps. *Mol Syst Biol* **7**:487.
14. **Leonard E, Nielsen D, Solomon K, Prather KJ.** 2008. Engineering microbes with synthetic biology frameworks. *Trends in biotechnology* **26**:674-681.
15. **Rutherford BJ, Dahl RH, Price RE, Szmidt HL, Benke PI, Mukhopadhyay A, Keasling JD.** 2010. Functional genomic study of exogenous n-butanol stress in *Escherichia coli*. *Appl Environ Microbiol* **76**:1935-1945.
16. **Brynildsen MP, Liao JC.** 2009. An integrated network approach identifies the isobutanol response network of *Escherichia coli*. *Mol Syst Biol* **5**:277.
17. **Dunlop MJ, Keasling JD, Mukhopadhyay A.** 2010. A model for improving microbial biofuel production using a synthetic feedback loop. *Syst Synth Biol* **4**:95-104.
18. **Freddolino PL, Tavazoie S.** 2012. Beyond homeostasis: a predictive-dynamic framework for understanding cellular behavior. *Annual Review Cell Developmental Biology* **28**:363-384.

19. **Nicolaou SA, Gaida SM, Papoutsakis ET.** 2010. A comparative view of metabolite and substrate stress and tolerance in microbial bioprocessing: From biofuels and chemicals, to biocatalysis and bioremediation. *Metabolic engineering* **12**:307-331.
20. **Sinensky M.** 1974. Homeoviscous adaptation--a homeostatic process that regulates the viscosity of membrane lipids in *Escherichia coli*. *Proceedings of the National Academy of Science U S A* **71**:522-525.
21. **Ingram LO.** 1976. Adaptation of membrane lipids to alcohols. *Journal of bacteriology* **125**:670-678.
22. **Papoutsakis ET.** 2008. Engineering solventogenic clostridia. *Curr Opin Biotechnol* **19**:420-429.
23. **Huffer S, Clark ME, Ning JC, Blanch HW, Clark DS.** 2011. Role of alcohols in growth, lipid composition, and membrane fluidity of yeasts, bacteria, and archaea. *Appl Environ Microbiol* **77**:6400-6408.
24. **Baer SH, Blaschek HP, Smith TL.** 1987. Effect of Butanol Challenge and Temperature on Lipid Composition and Membrane Fluidity of Butanol-Tolerant *Clostridium acetobutylicum*. *Appl Environ Microb* **53**:2854-2861.
25. **Borden JR, Papoutsakis ET.** 2007. Dynamics of genomic-library enrichment and identification of solvent tolerance genes for *Clostridium acetobutylicum*. *Appl Environ Microb* **73**:3061-3068.
26. **Reyes LH, Almario MP, Kao KC.** 2011. Genomic library screens for genes involved in n-butanol tolerance in *Escherichia coli*. *Plos One* **6**:e17678.

27. **Ramos JL, Duque E, Gallegos MT, Godoy P, Ramos-Gonzalez MI, Rojas A, Teran W, Segura A.** 2002. Mechanisms of solvent tolerance in gram-negative bacteria. Annual review of microbiology **56**:743-768.
28. **Minty JJ, Lesnefsky AA, Lin F, Chen Y, Zaroff TA, Veloso AB, Xie B, McConnell CA, Ward RJ, Schwartz DR, Rouillard JM, Gao Y, Gulari E, Lin XN.** 2011. Evolution combined with genomic study elucidates genetic bases of isobutanol tolerance in *Escherichia coli*. Microb Cell Fact **10**:18.
29. **Heipieper HJ, Neumann G, Cornelissen S, Meinhardt F.** 2007. Solvent-tolerant bacteria for biotransformations in two-phase fermentation systems. Applied microbiology and biotechnology **74**:961-973.
30. **Dombek KM, Ingram LO.** 1984. Effects of ethanol on the *Escherichia coli* plasma membrane. Journal of bacteriology **157**:233-239.
31. **Ingram LO, Buttke TM.** 1984. Effects of alcohols on micro-organisms. Advances in microbial physiology **25**:253-300.
32. **Ingram LO, Eaton LC, Erdos GW, Tedder TF, Vreeland NL.** 1982. Unsaturated fatty acid requirement in *Escherichia coli*: mechanism of palmitate-induced inhibition of growth of strain WN1. The Journal of membrane biology **65**:31-40.
33. **Ingram LO.** 1982. Regulation of fatty acid composition in *Escherichia coli*: a proposed common mechanism for changes induced by ethanol, chaotropic agents, and a reduction of growth temperature. Journal of bacteriology **149**:166-172.
34. **Chiou RY, Phillips RD, Zhao P, Doyle MP, Beuchat LR.** 2004. Ethanol-mediated variations in cellular fatty acid composition and protein profiles of two genotypically different strains of *Escherichia coli* O157:H7. Appl Environ Microbiol **70**:2204-2210.

35. **Segura A, Duque E, Mosqueda G, Ramos JL, Junker F.** 1999. Multiple responses of gram-negative bacteria to organic solvents. *Environ Microbiol* **1**:191-198.
36. **Kalscheuer R, Stolting T, Steinbuchel A.** 2006. Microdiesel: *Escherichia coli* engineered for fuel production. *Microbiology* **152**:2529-2536.
37. **Lu X, Vora H, Khosla C.** 2008. Overproduction of free fatty acids in *E. coli*: implications for biodiesel production. *Metabolic engineering* **10**:333-339.
38. **Crow P, Stone N, Kendall CA, Uff JS, Farmer JA, Barr H, Wright MP.** 2003. The use of Raman spectroscopy to identify and grade prostatic adenocarcinoma in vitro. *British journal of cancer* **89**:106-108.
39. **Mahadevan-Jansen A, Mitchell MF, Ramanujam N, Malpica A, Thomsen S, Utzinger U, Richards-Kortum R.** 1998. Near-infrared Raman spectroscopy for in vitro detection of cervical precancers. *Photochemistry and photobiology* **68**:123-132.
40. **Bocklitz T, Walter A, Hartmann K, Rosch P, Popp J.** 2011. How to pre-process Raman spectra for reliable and stable models? *Analytica chimica acta* **704**:47-56.
41. **Pilaniya K, Chandrawanshi HK, Pilaniya U, Manchandani P, Jain P, Singh N.** 2010. Recent trends in the impurity profile of pharmaceuticals. *J Adv Pharm Technol Res* **1**:302-310.
42. **Movasaghi Z, Rehman S, Rehman IU.** 2007. Raman spectroscopy of biological tissues. *Applied Spectroscopy Reviews* **42**:493-541.
43. **Dutta RK, Sharma PK, Pandey AC.** 2009. Surface enhanced Raman spectra of *Escherichia Coli* cell using ZnO nanoparticles. *Dig. J. Nanomater. Biostruct* **4**:83-87.

44. **She C, Dinh N, Tu AT.** 1974. Laser raman scattering of glucosamine *N*-acetylglucosamine, and glucuronic acid. *Biochimica et Biophysica Acta (BBA)-General Subjects* **372**:345-357.
45. **Wu H, Volponi JV, Oliver AE, Parikh AN, Simmons BA, Singh S.** 2011. *In vivo* lipidomics using single-cell Raman spectroscopy. *Proceedings of the National Academy of Sciences of the United States of America* **108**:3809-3814.
46. **Notingher I.** 2007. Raman spectroscopy cell-based biosensors. *Sensors* **7**:1343-1358.
47. **Collakova E, Aghamirzaie D, Fang Y, Klumas C, Tabataba F, Kakumanu A, Myers E, Heath LS, Grene R.** 2013. Metabolic and Transcriptional Reprogramming in Developing Soybean (*Glycine max*) Embryos. *Metabolites* **3**:347-372.
48. **Lu Y, Savage LJ, Larson MD, Wilkerson CG, Last RL.** 2011. Chloroplast 2010: a database for large-scale phenotypic screening of *Arabidopsis* mutants. *Plant physiology* **155**:1589-1600.
49. **Binenbaum Z, Klyman E, Fishov I.** 1999. Division-associated changes in membrane viscosity of *Escherichia coli*. *Biochimie* **81**:921-929.
50. **Shinitzky M, Barenholz Y.** 1974. Dynamics of the Hydrocarbon Layer in Liposomes of Lecithin and Sphingomyelin Containing Dicetylphosphate. *J. Biol. Chem.* **249**:2652-2657.
51. **Aronsson K, Ronner U, Borch E.** 2005. Inactivation of *Escherichia coli*, *Listeria innocua* and *Saccharomyces cerevisiae* in relation to membrane permeabilization and subsequent leakage of intracellular compounds due to pulsed electric field processing. *International journal of food microbiology* **99**:19-32.

52. **Kong K, Rowlands CJ, Elsheikha H, Notingher I.** 2012. Label-free molecular analysis of live *Neospora caninum* tachyzoites in host cells by selective scanning Raman microscopy. *The Analyst* **137**:4119-4122.
53. **Lee TH, Chang JS, Wang HY.** 2013. Rapid and *in vivo* quantification of cellular lipids in *Chlorella vulgaris* using near-infrared Raman spectrometry. *Analytical chemistry* **85**:2155-2160.
54. **Cherney DP, Conboy JC, Harris JM.** 2003. Optical-trapping Raman microscopy detection of single unilamellar lipid vesicles. *Anal Chem* **75**:6621-6628.
55. **Schultz ZD, Levin IW.** 2011. Vibrational spectroscopy of biomembranes. *Annual Review of Analytical Chemistry* **4**:343-366.
56. **Neidhardt FC, Ingraham JL, Schaechter M.** 1990. *Physiology of the bacterial cell: a molecular approach.* Sinauer Associates Sunderland, MA.
57. **Zhu G, Zhu X, Fan Q, Wan X.** 2011. Raman spectra of amino acids and their aqueous solutions. *Spectrochimica acta. Part A, Molecular and biomolecular spectroscopy* **78**:1187-1195.
58. **Gardikis K, Hatziantoniou S, Viras K, Wagner M, Demetzos C.** 2006. A DSC and Raman spectroscopy study on the effect of PAMAM dendrimer on DPPC model lipid membranes. *International journal of pharmaceutics* **318**:118-123.
59. **Mendelsohn R, Koch CC.** 1980. Deuterated phospholipids as Raman spectroscopic probes of membrane structure: phase diagrams for the dipalmitoyl phosphatidylcholine (and its d62 derivative)-dipalmitoyl phosphatidylethanolamine system. *Biochimica et Biophysica Acta (BBA)-Biomembranes* **598**:260-271.

60. **Wu Q, Hamilton T, Nelson WH, Elliott S, Sperry JF, Wu M.** 2001. UV Raman spectral intensities of *E. coli* and other bacteria excited at 228.9, 244.0, and 248.2 nm. *Analytical chemistry* **73**:3432-3440.
61. **Wu Q, Nelson WH, Elliot S, Sperry JF, Feld M, Dasari R, Manoharan R.** 2000. Intensities of *E. coli* nucleic acid Raman spectra excited selectively from whole cells with 251-nm light. *Analytical chemistry* **72**:2981-2986.
62. **Weber FJ, de Bont JA.** 1996. Adaptation mechanisms of microorganisms to the toxic effects of organic solvents on membranes. *Biochimica et biophysica acta* **1286**:225-245.

## CHAPTER THREE

# Assessment of *ex vivo* perfused liver health by Raman spectroscopy

(Manuscript under review by Journal of Raman Spectroscopy)

Reprinted with permission from Theresah N. K. Zu, et al., Journal of Raman Spectroscopy (Manuscript ID JRS-14-0160), 2014.

Theresah N. K. Zu<sup>1</sup>, Ahmad I. M. Athamneh<sup>1</sup>, Eva Collakova<sup>2</sup>, Chip Aardema<sup>4</sup>, Thomas Hawken<sup>3</sup>, John Robertson<sup>3,4</sup>, and Ryan S. Senger<sup>1,\*</sup>

<sup>1</sup>Department of Biological Systems Engineering; Virginia Tech; Blacksburg, VA 24061

<sup>2</sup>Department of Plant Pathology and Weed Science; Virginia Tech; Blacksburg, VA 24061

<sup>3</sup>Virginia-Maryland Regional College of Veterinary Medicine; Blacksburg, VA 24061

<sup>4</sup>School of Biomedical Engineering and Science; Blacksburg, VA 24061

\*Corresponding author

Corresponding author email address: senger@vt.edu

# Assessment of *ex vivo* perfused liver health by Raman spectroscopy

## ABSTRACT

Raman spectroscopy was applied in this research to monitor the overall health and degradation of porcine livers perfused *ex vivo* using the VasoWave<sup>®</sup> perfusion system. A novel Raman-based diagnostic analysis was developed that enables near real-time and label-free monitoring of organ health during *ex vivo* perfusion designed to extend the useful life of the organ for transplantation. A multivariate statistical analysis of Raman spectra of organ perfusate fluid, using a combination of principal component analysis and linear discriminant analysis, proved to be an effective technique to assess the degradation properties of the livers. Three livers (with replicates) were perfused *ex vivo* under different pressures and temperatures and were compared over a 24 h time-course. Results indicated that perfusion pressure was a more significant factor in organ degradation than was temperature. In addition, a non-linear degradation profile was identified for all three perfused livers, and this profile was different for individual livers, demonstrating the time-dependent transition from its initial “healthy” state towards a more “unhealthy” degenerative state at 24 h. The Raman spectroscopy based approach described here has potential applications in perfusion and diagnostic instrumentation that can be used in near real-time during organ transit and in operating rooms to help identify appropriately healthy organs for transplantation.

## INTRODUCTION

### Liver transplant statistics and challenges

#### *Statistics*

In this research, Raman spectroscopy was investigated as a diagnostic tool to monitor the health of livers awaiting transplantation. Donated organ preservation is needed desperately, as a shortage of transplantable organs exists. As of April 2014, the Organ Procurement and Transplantation Network reported more than 133,000 candidates in the US alone on the waiting list for an organ (kidney, liver, heart, or lung), and more than 16,000 were on the waiting list for a liver (1). Chronic liver disease and cancer caused by preventable hepatitis B and C infections affect 1-2% of the US population (and about 390 million people world-wide), is responsible for more than 16,000 deaths in the US annually (and about 1.1 million deaths world-wide), and significantly increases health care expenditures (2-4). In addition to viral infections, excessive alcohol consumption has been attributed to the rising cases of liver disease such as alcoholic fatty liver, alcoholic hepatitis, and alcoholic cirrhosis, all of which have life-threatening consequences (5, 6). Obesity also contributes in complex ways to all causes of liver dysfunction. Over the years, the list of patients awaiting liver transplantation has increased considerably, due to improved health care that has decreased immediate morbidity/mortality. Unfortunately, a scarcity of donors has also resulted. In the present research, a method of transplantable liver preservation by *ex vivo* perfusion was implemented. The perfusion fluid was monitored in near real-time by Raman spectroscopy, which was found to provide information about liver health. The new methodology was used to study the effects of *ex vivo* perfusion pressure and temperature by determining the rate of degradation of several livers over a 24 h time-course.

### ***Guidelines for liver transplantation***

Diagnosis of liver disease often follows liver biopsy and functional tests (7). For acute cases associated with hepatitis viral infections, immediate treatments involve the use of antiviral drugs before the disease progresses from fibrosis to cirrhosis (8, 9). Liver transplantation (like most other organ transplantation) is the last resort for a patient suffering from an end-stage disease, such as chronic cirrhosis (8, 10). This procedure is known to reduce the mortality rate of affected persons significantly, provided there is no recurrence (8). Liver injury (irrespective of cause), hepatitis virus, alcohol, nonalcoholic fatty liver disease, or cancer can lead to aberrant attempts at regeneration resulting in cirrhotic scarring (11). However, in severe cases, liver transplantation provides the best chances of survival. The current guiding principles for liver allocation follow those of urgency and utility. The urgency principle advocates treatment of the sickest persons on the Waiting List, based on the Model of End-Stage Liver Disease (MELD) score, while the utility principle focuses on maximizing the survival rate post-transplant (12). There are two main sources of donated livers: (i) donation after cardio-circulatory death (DCD) and, (ii) donation after brain-death (DBD), and the criteria for selection and allocation of livers have been reviewed comprehensively in the literature (13-15). In some countries, segmental donation of a portion of liver from living related donors is done.

### ***Methods of organ storage pending transplant***

For over two centuries, scientists and clinicians have experimented with organ preservation outside of the human body. In current protocols, following harvest, livers are stored on ice (static cold storage) for periods up to 8-12 hours before implantation. Recent developments with hypothermic machine perfusion of donated kidneys have shown superior performance in kidney preservation (16). Studies with kidneys have shown that hypothermic oxygenated perfusion (i.e.,

nutrient-rich, oxygenated blood substitute at sub-physiological temperature) was successful at sustaining the overall quality of perfused kidneys and improving outcomes following transplantation (17, 18). Major contributors to the success of kidney preservation *ex vivo* are reliable pumps, successful methods for keeping organ adequately oxygenated, and a reliable means of controlling temperature (19). Different types of pumping equipment have been used in machine pulsatile perfusion of organs, usually employing the University of Wisconsin (UW) preservation solution (20, 21). Hypothermic machine preservation is thought to help reduce or prevent ischemic injury, an unavoidable step following organ procurement and actual transplant when the blood supply is temporarily interrupted. Lengthy static cold storage (>24 hours) of kidneys is known to be detrimental (22). There have not been extensive studies of successful machine perfusion of other organs, such as liver and heart.

#### ***Description of VasoWave® technologies***

A new *ex vivo* organ perfusion system, the VasoWave® (Smart Perfusion; Denver, NC), was developed to preserve organs for transplantation. A unique feature of this system is that it closely mimics physiologic perfusion waveform characteristics of the human circulatory system. Pressurized perfusion fluid is delivered to an organ through the arterial/portal feeds and exits the organ via the venous line providing a closed loop circulation with highly controlled pressures, flow rates, and fluid temperature. The pulse regulator, a patented technology, is the major feature of the system, and it develops and supplies the cardiac waveform associated with the human heart. The VasoWave® system allows the user to instantaneously monitor and program the shape, duration, pulse, and pressure (systolic and diastolic) of a produced waveform. Current hypothermic machine perfusion systems in clinical use do not have the ability to monitor real-time parameters such as: (i) tissue viability, (ii) metabolic degradation products, (iii) oxygenation state, and (iv) nutrient

requirements for an organ undergoing perfusion. Most importantly, the use of the VasoWave<sup>®</sup> system allows lengthy *ex vivo* organ preservation (>12 hours) and repetitive sampling of the perfusion fluid bathing the excised organ. This sampling permits temporal measurements of tissue and perfusion fluid analytes that can be correlated with pathophysiology data and other metrics of organ quality. The research data presented here illustrates the use of Raman spectroscopy as a potential near real-time diagnostic tool to monitor total organ health during the perfusion process.

### ***Methods for assessment of liver quality***

Currently, methods to assess the “quality” of donated livers that may be transplanted consist of evaluation of donor characteristics (overall health, co-morbidities, laboratory tests), visual inspection of the potentially transplantable organ, and biopsy/histologic interpretation. Over 50% of potentially transplantable organs are discarded based on these evaluations (23). More complex tests, such as evaluation of metabolic activity and endogenous quantification of liver function in donors, are costly and impossible within the time-constraints of donation/implantation (8-12 hours).

### ***Raman spectroscopy and liver disease diagnosis***

Raman spectroscopy is gaining momentum in the study of cells, tissues, and organs (24-28). Major advantages of Raman spectroscopy for analysis of fluid samples include its (i) non-invasiveness, (ii) fast acquisition time, (iii) minimal sample preparation (i.e., no labeling) and (iv) low sensitivity to water. Relatively little research has been performed to date regarding analysis of liver perfusion fluid and tissue by Raman spectroscopy. A previous study using principal component analysis (PCA) of Raman spectra of human liver perfusion fluid found correlation with the oxidation reduction potential (ORP) of the fluid, which may have ties to organ viability (29). With biopsied liver tissue, an increase in the intensity of the following Raman bands have been

found to be associated with liver injury and fibrosis: 644  $\text{cm}^{-1}$  (Tyr), 853  $\text{cm}^{-1}$  (Pro, Tyr), 1004  $\text{cm}^{-1}$  and 1033  $\text{cm}^{-1}$  (Phe), 1083  $\text{cm}^{-1}$  (phospholipids), 1303  $\text{cm}^{-1}$  (collagen), 1248  $\text{cm}^{-1}$  (amide III, collagen, Tyr), and 1660  $\text{cm}^{-1}$  (amide I, collagen,  $\alpha$ -helix) (30). A decrease in Raman band intensity resulting from stretching vibration of the C-S bond of cysteine (660  $\text{cm}^{-1}$ ) has been associated with fibrosis in biopsied liver tissue. Similarly, liver tissue has been characterized using Raman spectroscopy according the intensity ratio of phospholipids and collagen (1450  $\text{cm}^{-1}$ ) to cysteine (1666  $\text{cm}^{-1}$ ) (30).

### ***Studying the effects of ex vivo perfusion on porcine liver health***

Hypothermic machine perfusion has been shown to be superior to simple cold storage in experiments with rat, canine, and porcine livers when livers were continuously perfused for up to 72 h (31, 32). In the current research, porcine livers were perfused using the VasoWave<sup>®</sup> system at different operating conditions of temperature and pressure. Raman spectroscopy was applied to study changes in the perfusion fluid in near real-time. Multivariate statistical analysis, specifically PCA followed by linear discriminate analysis (DA), was applied to Raman spectra to determine the rates and possible mechanisms by which the organs degraded under the different perfusion conditions. This multivariate statistical analysis approach was compared to a more traditional method of Raman spectra analysis in which the intensities of specific Raman bands (corresponding to functional groups of key molecules) are compared over a time-course and among samples. Results revealed a significant advantage to the multivariate approach that makes use of entire Raman spectra as opposed to specific Raman bands. The overall goal of this research is to establish a non-invasive diagnostic tool capable of near monitoring consisting of Raman spectroscopy and multivariate statistical analysis that can provide the first measure of overall *ex vivo* perfused liver health. Thus, the ability to monitor the health of livers in near real-time as they are perfused *ex*

*in vivo* may have significant value as donor organs are transported as well as in the operating room immediately prior to transplantation.

## **MATERIALS AND METHODS**

### ***Animals and liver conditioning***

Porcine liver procurement methods have been described elsewhere (33) and were used in this research with some modifications. Livers were obtained from humanely sacrificed mixed breed female pigs. Within 15 min of death, livers were harvested, flushed of whole blood with ice cold (4°C) modified Krebs-Henseleit solution, with added heparin anticoagulant, and stored on ice. Livers were stored for 2 h after procurement for transport to the laboratory to begin perfusion with the VasoWave<sup>®</sup> system, as described below. To facilitate connection with the perfusion system, Luer lock syringe connections were made with the portal vein, hepatic artery, and major hepatic vein. Livers were then perfused with Krebs-Henseleit solution on the VasoWave<sup>®</sup> system. The Krebs-Henseleit solution consisted of 118 mM NaCl, 4.7 mM KCl, 1.2 mM MgSO<sub>4</sub>·7H<sub>2</sub>O, 1.2 mM KH<sub>2</sub>PO<sub>4</sub>, 10 mM glucose, 2 mM CaCl<sub>2</sub>·2H<sub>2</sub>O, 4.2 mM NaHCO<sub>3</sub>, 200 mM sulphinpyrazone, and 10 mM HEPES buffer.

### ***Liver perfusion by VasoWave<sup>®</sup>***

The VasoWave<sup>®</sup> perfusion system (Smart Perfusion; Denver, NC) was used to perfuse livers *ex vivo* for a period of 24 h under different temperature and pressure profiles. The novelty of this system is its ability to produce a cardio-emulating pulse wave (competing technologies produce a sinusoidal pulse wave) that generates physiological systolic and diastolic pressures and flow rates within a perfused organ. The system also allows for direct control of oxygen content of perfusate. Active perfusion with Krebs-Henseleit solution was initiated on each liver following a

two-hour flush. Perfusion was continued for 24 h in a closed circuit. This circuit consisted of the following components: (i) perfusate reservoir bag, (ii) cardiovascular emulation system pump, (iii) heat exchanger, (iv) pressure regulator, (v) atrial line, (vi) perfused liver, (vii) ventricular line, and (viii) recycle stream. Samples of the perfusion fluid were collected at eight time points (0, 0.5, 1, 2, 4, 8, 16, and 24 h) for each liver. A total of six porcine livers were studied in this research, which allowed for three experimental conditions with replicates. The effects of temperature (3°C and 25°C) and pressure (70-30 mmHg and 110-70 mmHg) were studied. Specifically, (i) condition A used a perfusion systolic-diastolic pressure of 70-30 mmHg and temperature 3°C, (ii) condition B consisted of 110-70 mmHg pressure and 25°C, and (iii) condition C consisted of 70-30 mmHg pressure and 25°C. Fluid samples were also collected at selected time points from livers maintained only in static cold storage, for comparison with VasoWave® perfusion fluid samples.

### ***Raman spectroscopy***

Ten micro-liters (10 µL) of perfusate fluid was air dried on an aluminum surface at room temperature and analyzed by Raman spectroscopy. Samples were analyzed using a Bruker Senterra dispersive Raman spectrometer (Bruker Optics; Billerica, MA) equipped with a confocal microscope. The sample excitation was performed with a 532 nm laser set to 20 mW power and focused through a 100x objective lens. A scan time of 20 s and a spectral resolution of 9-15 cm<sup>-1</sup> were used for all measurements. For each sample, a minimum of 50 individual spectra (from different locations of the dried sample) were acquired and used in statistical analyses (discussed below). All spectra were baseline corrected and analyzed using OPUS 7.2 software (Bruker Optics, Billerica, MA). All spectra were further normalized using methods described below prior to multivariate statistical analyses.

### ***Fatty acid analysis***

Extraction of liver perfusate fatty acids was performed following a published protocol (34) with modifications detailed below. Fatty acids from liver perfusates (150  $\mu$ L) were extracted with 2 volumes of chloroform and 1 volume of methanol in the presence of 10  $\mu$ g of heptadecanoic acid (absent from liver perfusates) as an internal standard to account for analyte recovery. The chloroform phase was dried under a stream of nitrogen gas and fatty acids were then esterified to fatty acid methyl esters (FAME) in the presence of 1 N methanolic HCl. FAME were extracted with heptanes and analyzed by gas chromatography coupled with flame ionization detection (GC-FID) after the initial identification of FAME peak identities by mass spectroscopy (MS). FAME separation and analysis was done using an Agilent 7890A series GC and a 5975C series single quadrupole MS or FID (Agilent Technologies; Santa Clara, CA) equipped with a 30 m DB-column (0.25  $\mu$ m x 0.25 mm, Agilent Technologies) (34).

### ***Total protein measurements***

The amount of total protein in perfusion fluids was measured (triplicate per sample) using a Coomassie Plus<sup>TM</sup> (Bradford) Assay kit (Thermo Scientific; Rockford, IL) following the manufacturer's protocol. Perfusion fluids were used as is with no further treatment for total protein analysis. Data was acquired by measuring absorbance at 595 nm using a BioTek Synergy H4 Hybrid Multimode Microplate Reader (BioTek; Winooski, VT).

### ***Statistical methods***

Statistical analyses were performed to (i) identify correlations between relevant Raman spectral bands and measured fatty acid and protein data, (ii) identify sample outliers, and (iii) separate and cluster Raman spectra according to liver treatment parameters. All calculations were performed using MATLAB (R2012b) (MathWorks; Natick, MA). All spectra were vector

normalized over the entire wavenumber range of the spectra. First, correlations between Raman band intensities and experimentally measured FAME and total protein values were found by calculating the correlation coefficient (R) between experimental data points and Raman intensities at several wavenumbers. Multiple Raman band assignments have been made in the literature to different fatty acids and total protein, and this analysis was used to test which of those candidates produced an accurate representation of liver perfusate fluid. The entire list of candidates examined has been published previously (35). PCA was applied to all spectra simultaneously in order to first identify and remove spectral outliers. With the remaining Raman spectra, DA was applied in order to separate and cluster samples based on (i) the liver analyzed, (ii) temperature, (iii) pressure, and (iv) the time point of sampling. Instead of using the entire spectral range (600-3200  $\text{cm}^{-1}$ ) for DA, PCA was first performed to reduce the spectral dimensionality (i.e., the number of Raman intensity data points associated with each spectra). Dataset reduction was found to be important, in cases where DA was applied to a large number of spectra, in order to reduce computational cost and increase the probability of finding the best model that represents the data (i.e., avoiding overfitting). Spectral dataset reduction using PCA was performed using Raman intensities from the entire spectral region (600-3200  $\text{cm}^{-1}$ ). The resulting first 50 principal components of a spectrum were used as the reduced dataset and were inputs for DA analysis. This was based on a previously published finding (36).

## **RESULTS**

### ***Reproducibility and changes observed in Raman spectra***

Livers were perfused on the VasoWave<sup>®</sup> system under different pressures and temperatures and were compared (i) at several time points following perfusion onset and (ii) to un-perfused livers

undergoing cold static storage. For each set of the conditions (i.e., liver, pressure, temperature, and time point), a minimum of 50 Raman spectra of perfusion fluid (or of stagnant fluid of unperfused livers) were obtained, baseline corrected (using OPUS software), and vector normalized (in MATLAB). Averaged Raman spectra for a perfused liver at 0 h, 4 h, and 8 h are shown in Fig. 1a. Results were found to be highly reproducible, resulting in very low standard deviations (shown in Fig. 1b). Clear differences in Raman spectra appeared throughout the duration of perfusion. In particular, the overall signal intensity of the biological region of the Raman spectra (Fig. 1a) decreased with time; however, noticeable band shifts were observed and certain band intensities decreased faster than others, suggesting these result from metabolic changes of the liver itself. In addition, Raman scans of the initial blood cleared from the liver revealed no similarities with the perfusate scans (results not shown), which suggest the observed effects are not due to clearing of residual blood with time by perfusion. In addition, averaged Raman scans of perfusate sampled from livers perfused under conditions A (70-30 mmHg, 3°C), B (110-70 mmHg, 25°C), and C (70-30 mmHg, 3°C) at 8 h are shown in Fig. 2 for the (a) biological region (600-1800  $\text{cm}^{-1}$ ) and (b) – CH dominated region (2800-3100  $\text{cm}^{-1}$ ). Thus, perfusate conditions, in addition to time, were observed to significantly impact resulting Raman spectra. While Figs. 1 and 2 demonstrate the ability of Raman spectroscopy to detect the subtle changes in response to environmental conditions and duration of perfusion, more meaningful results were not extracted from the individual bands of these datasets. The molecular marker(s) of liver degradation have not yet been identified as distinct Raman bands in Figs. 1 and 2. Attempts to correlate individual Raman bands with fatty acids and total protein are discussed in a following section. However, to make meaningful conclusions, multivariate analysis involving PCA and DA with the entire Raman spectra was required. This is demonstrated in the following sections.

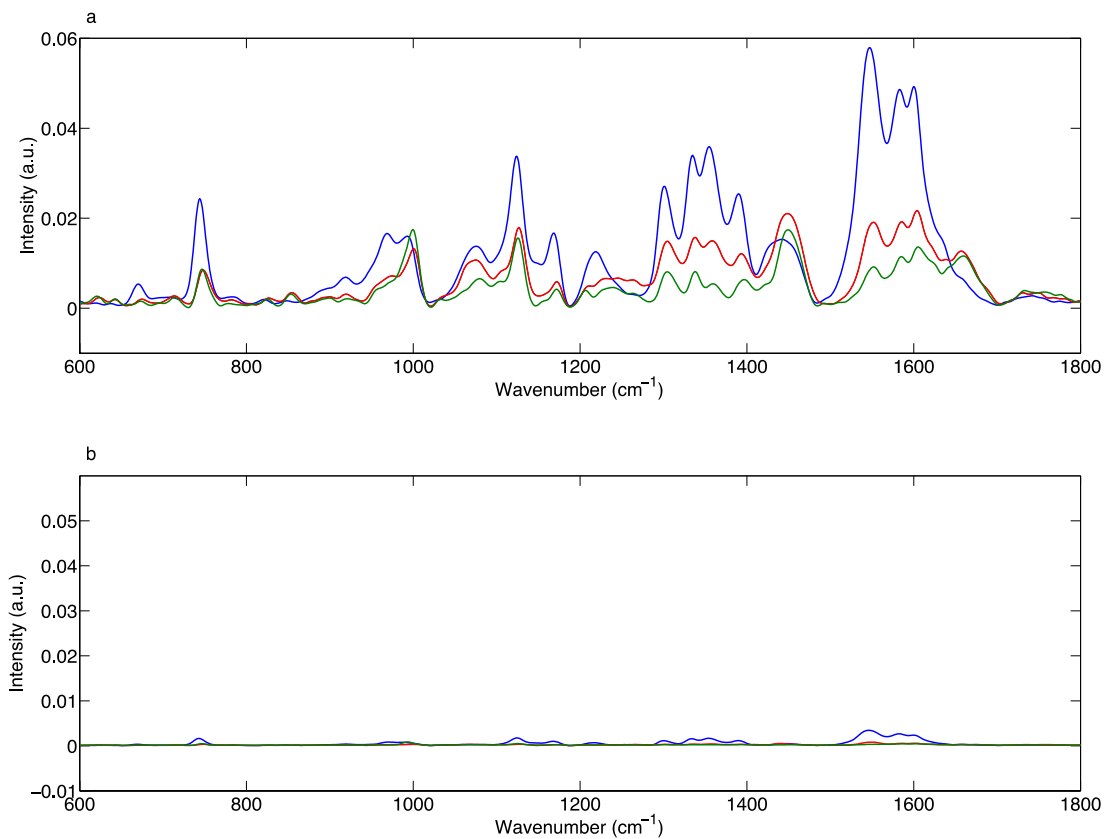


**Figure 1.** (a) Raman spectra of perfused porcine liver at the following time points: 2 hours before perfusion begins (blue line), 1 hour of perfusion (red line), and 8 hours of perfusion (green line). (b) The standard deviations of 50 replicate scans for each sample.

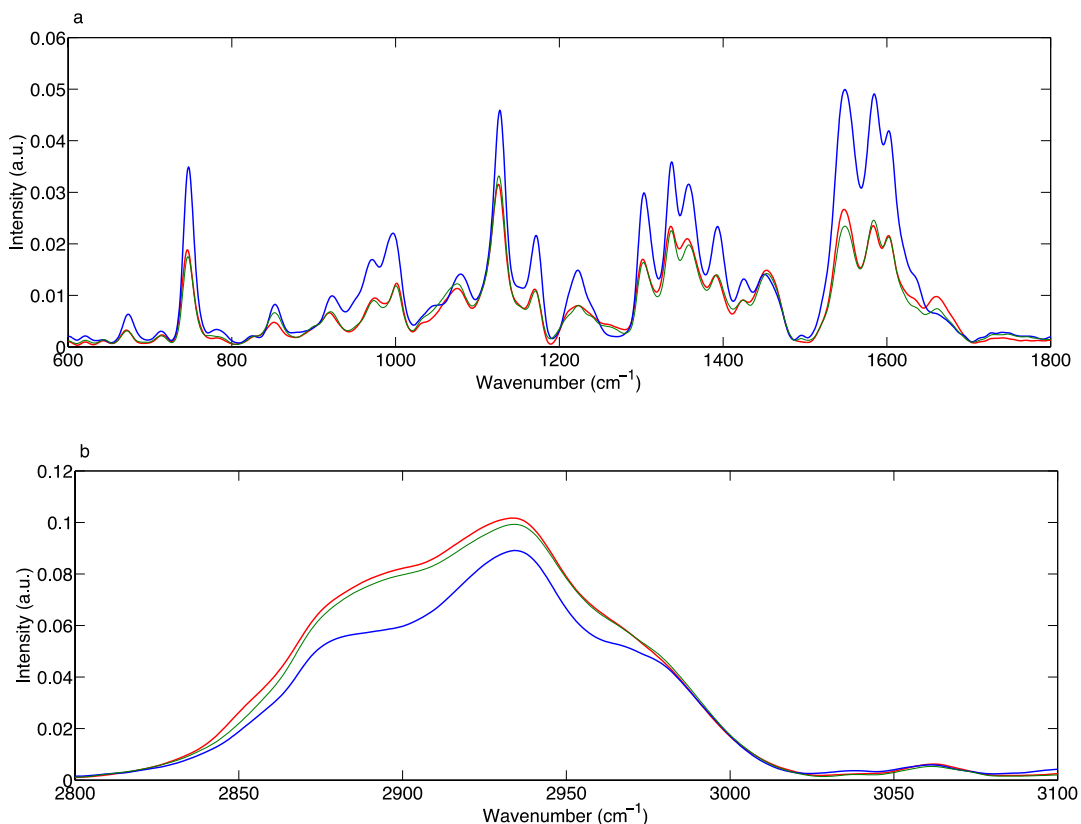


**Figure 2.** (a) Raman spectra of the biological region at 8h of perfusion for livers perfused under conditions A (red line), B (green line), and C (blue line). (b) Raman spectra of the  $-CH$  region for the three livers.

### ***Multivariate statistical analysis of Raman spectra***

DA was performed as described in the methods section on PCA reduced Raman spectra of sampled fluids from perfused and un-perfused livers. Results are shown in Fig. 3a for perfused and un-perfused samples taken at 0 h and 8 h. DA produced clear separation among the perfused samples; however, only a small separation was observed for the un-perfused samples. The un-perfused samples did not undergo the initial flush procedure, so the Raman signal was likely dominated by blood and stagnant fluid that changed in composition very little over the 8 h cold static incubation

period. However, this does not imply that the organ did not undergo significant degradation during this time. Having shown that DA could easily separate perfused and un-perfused samples, the next challenge was to establish separation based on perfusion conditions. Three sets of results were generated. The first set (shown in Fig. 3b-d) considers three livers perfused under perfusion Conditions A, B, and C. The second set (contained in the Supplementary Appendix as Figs. S1-S3) considers the replicate three livers under perfusion Conditions A, B, and C. The final set (Figs. S4-S6) provides the multivariate statistical results when all six livers are considered simultaneously. The three livers (and replicates) were subjected to different perfusion conditions (A (70-30 mmHg, 3°C), B (110-70 mmHg, 25°C), and C (70-30 mmHg, 25°C)) and were compared across one varied condition at a time. All Raman spectral data for all livers were combined and DA was first applied to discriminate according to pressure. Results are shown in Fig. 3b for the first three livers tested (without replicates). Clear separation was observed between livers from condition B (perfused at 110-70 mmHg) and conditions A and C (perfused at 70-30 mmHg). This indicates pressure was a significant factor in determining the differences among the reduced Raman spectra of the livers studied. Next, DA was applied to classify Raman spectra according to temperature of perfusion fluid, and results for the three livers are shown in Fig. 3c. While separation was still observed, significant overlap of clusters was also present. These results suggest that both pressure and temperature are important perfusion parameters. While the influence of temperature may be more intuitive, results show that changes in pressure directly influence the metabolic activity and degradation kinetics of an *ex vivo* perfused liver. This result has already been established and was the basis for the design of the VasoWave<sup>®</sup> instrumentation (37); however, it can now be measured and visualized by Raman spectroscopy and multivariate statistical analysis. Finally, the Raman spectra were classified using DA on the basis of time (hours

of perfusion). Results are shown in Fig. 3d (again, for the three livers) and establish a trend showing the overall progression from the initial sample (0 h) to the final sample (24 h). Of course, this trend comprises both pressure and temperature conditions. These results suggest that a DA model can be used to determine how far a perfused liver has degraded from its initial state. These analyses were repeated for the three liver replicates (Figs. 4-6) and for the set of all six livers considered simultaneously (Figs. 7-9).

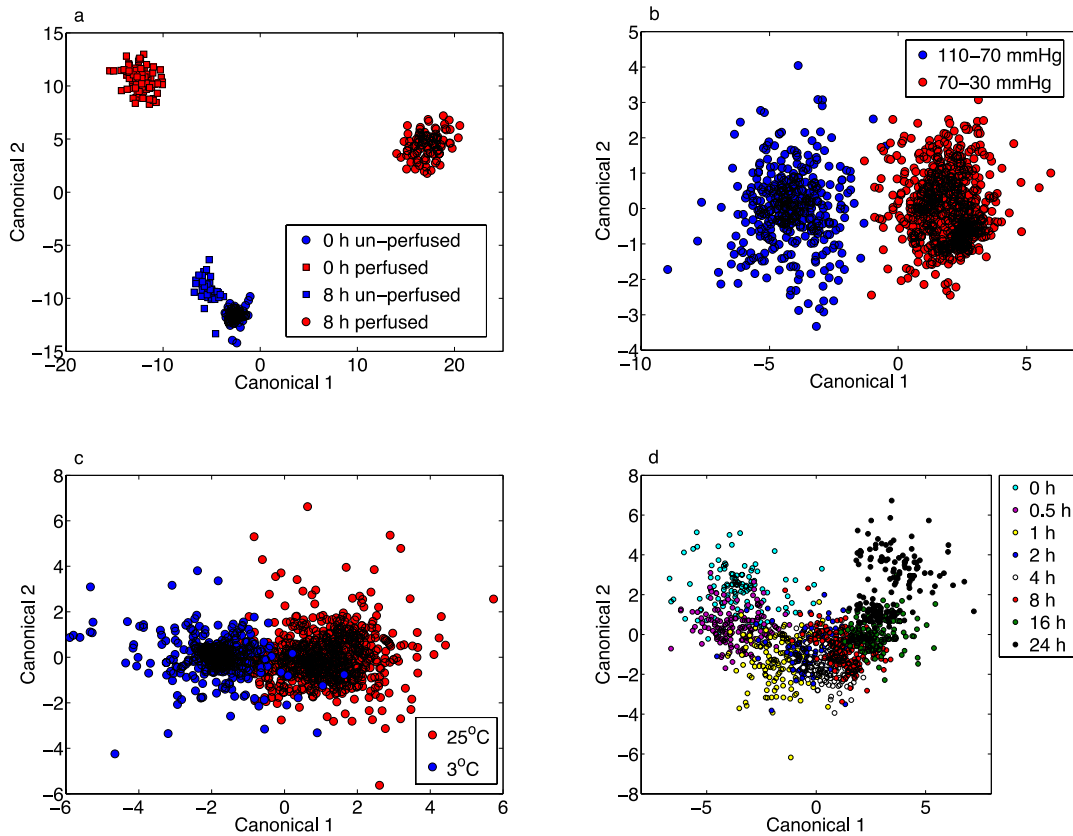


**Figure 3.** Discriminant analysis results of (a) un-perfused and perfused livers at 0 h and 8 h, (b) all data points for livers perfused under conditions A, B, and C discriminated by pressure, (c) all data points for livers perfused under conditions A, B, and C discriminated by temperature, and (d) all data points for livers perfused under conditions A, B, and C discriminated by time.

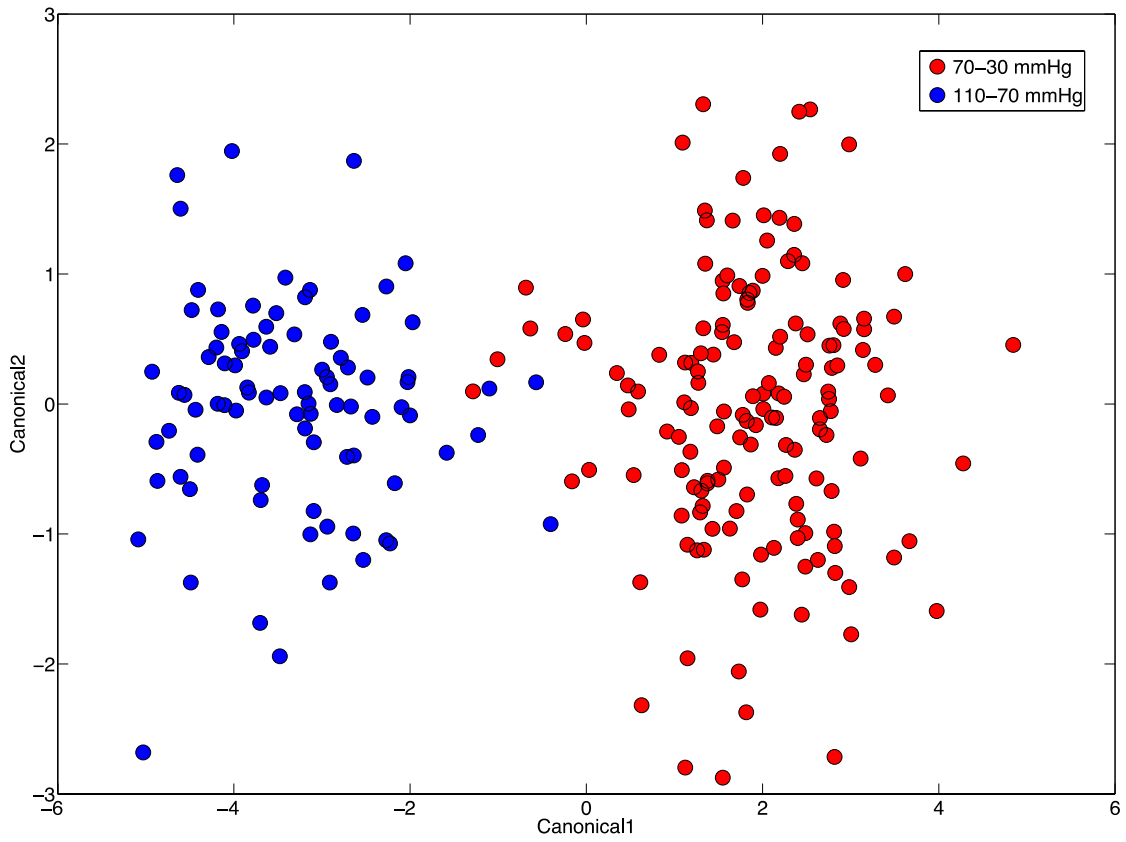


**Figure 4.** Multivariate statistical analysis of the 2<sup>nd</sup> set of three livers. All data points for livers perfused under conditions A, B, and C discriminated by pressure.

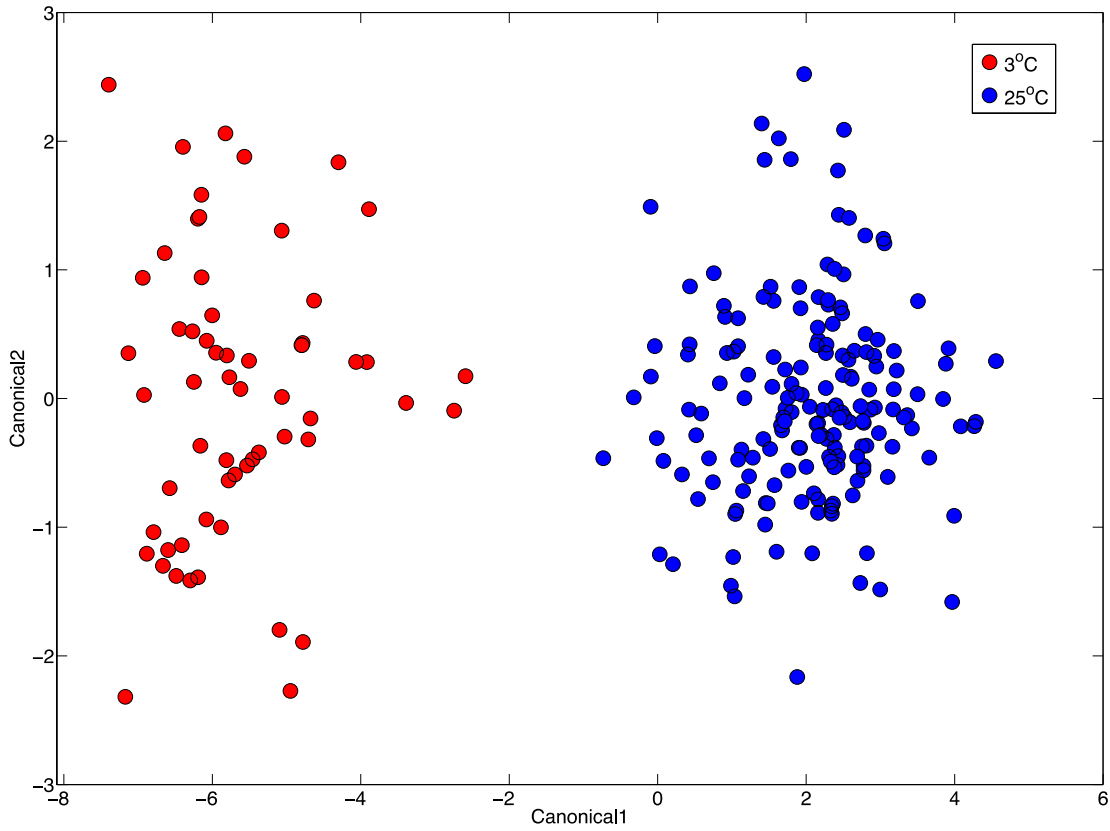


**Figure 5.** Multivariate statistical analysis of the 2<sup>nd</sup> set of three livers. All data points for livers perfused under conditions A, B, and C discriminated by temperature.

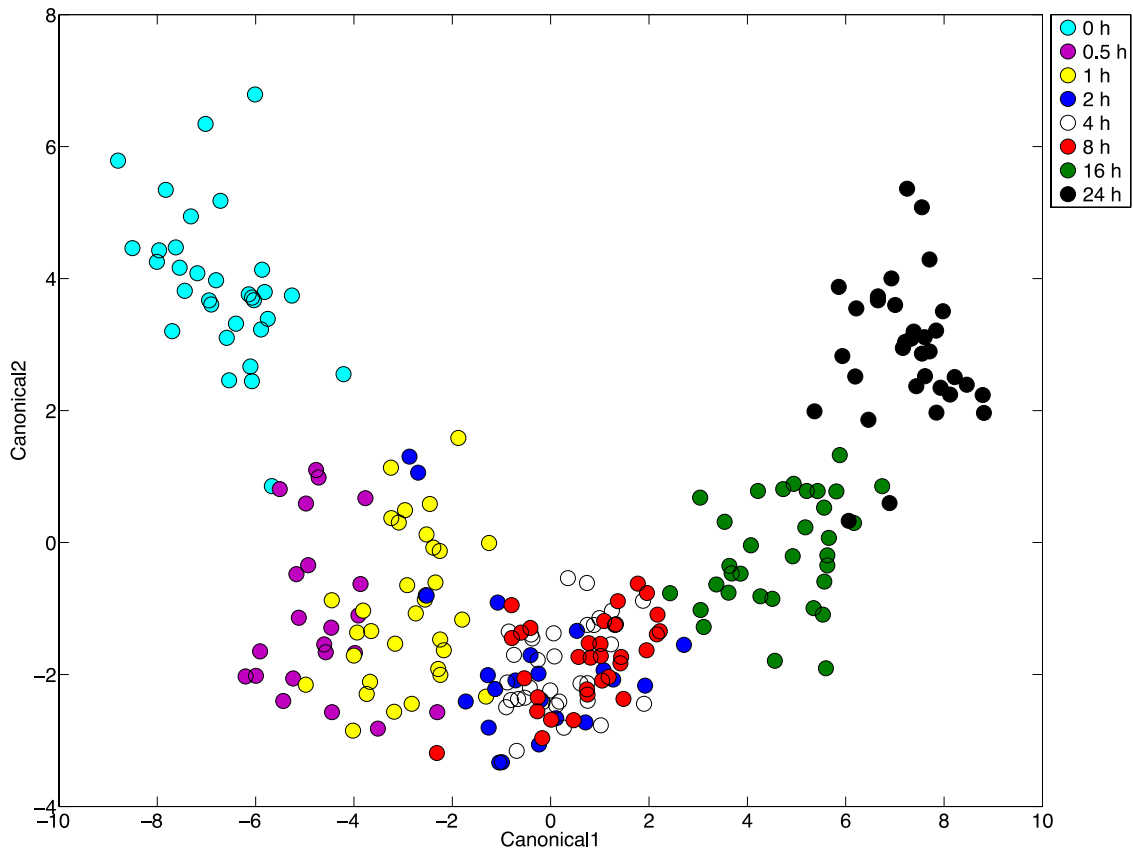


**Figure 6.** Multivariate statistical analysis of the 2<sup>nd</sup> set of three livers. All data points for livers perfused under conditions A, B, and C discriminated by time.

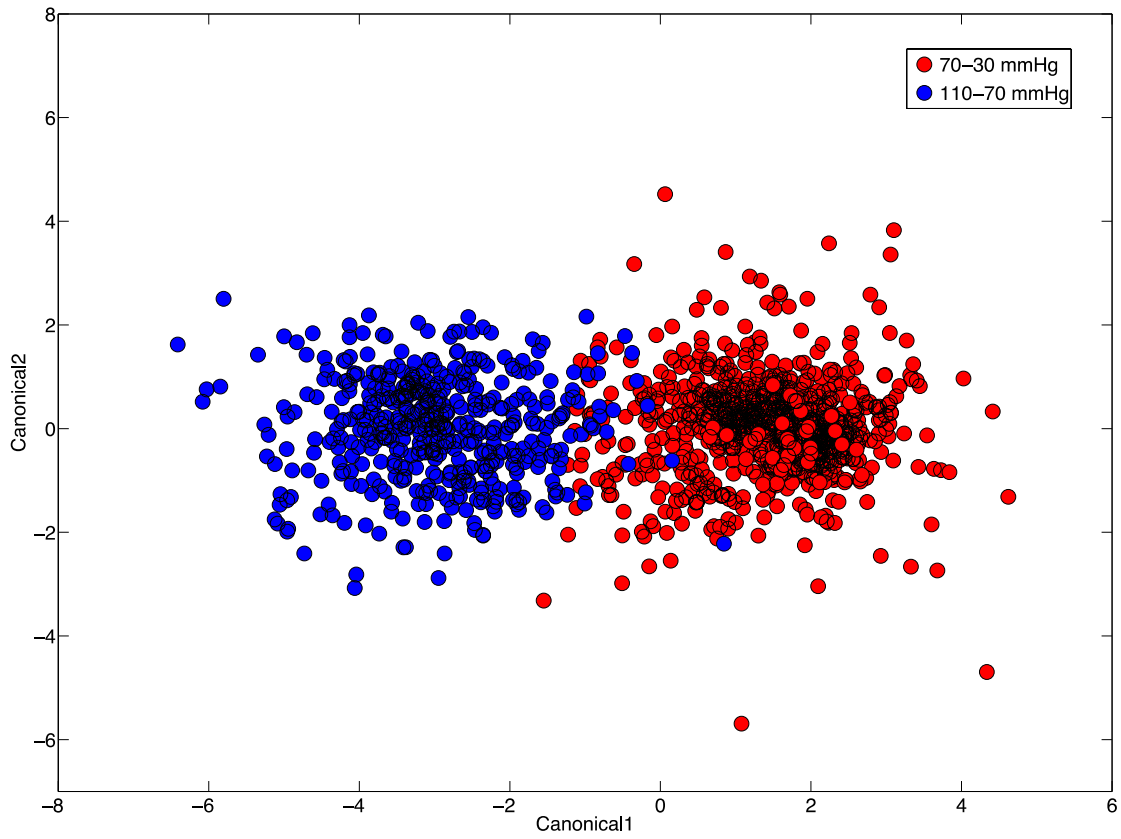


**Figure 7.** Multivariate statistical analysis of all livers. All data points for livers perfused under conditions A, B, and C discriminated by pressure.

Results showed a clear influence of both pressure and temperature for the additional three livers (Figs. 4-6), and similar degradation kinetics were revealed compared to the first three livers (Figs. 6 and 3d). When all six livers were considered simultaneously, the perfusion pressure had a larger influence than temperature (Figs. 7-9); although, this was not seen with the second set of three livers (Figs. 4-6). In addition, the degradation kinetics were similar for the livers considered simultaneously as when they were considered individually (Fig. 9).

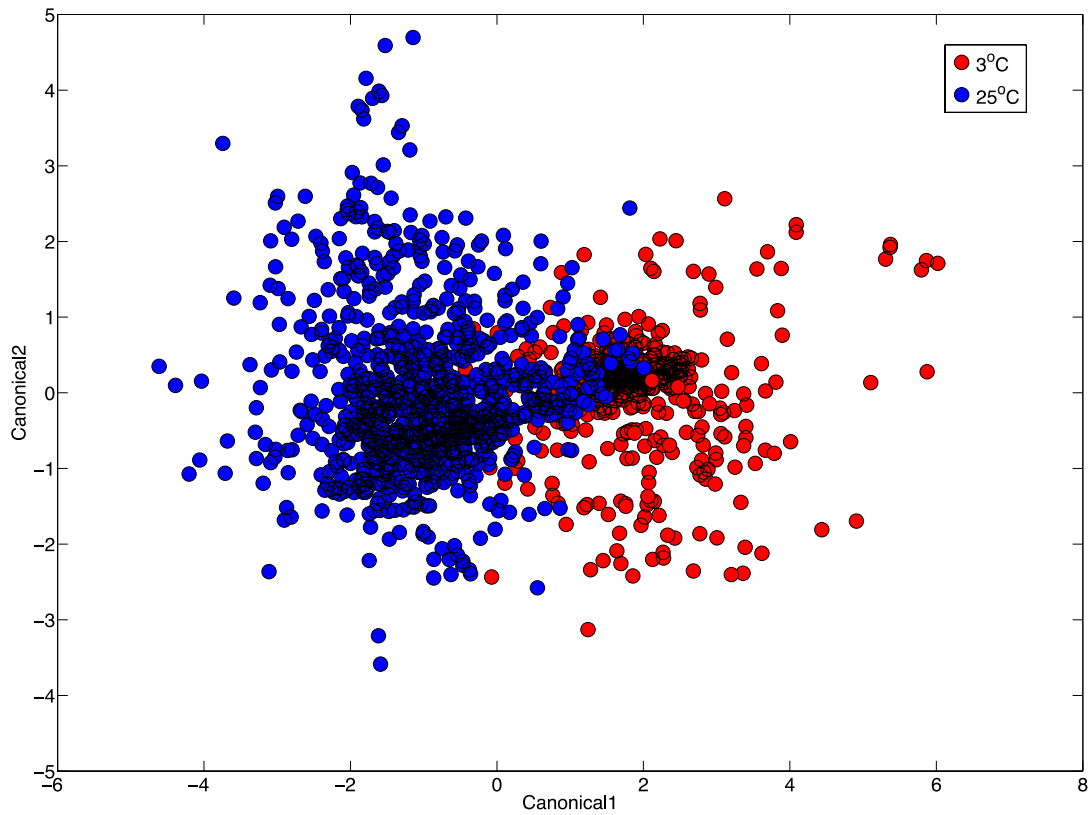


**Figure 8.** Multivariate statistical analysis of all livers. All data points for livers perfused under conditions A, B, and C discriminated by temperature.

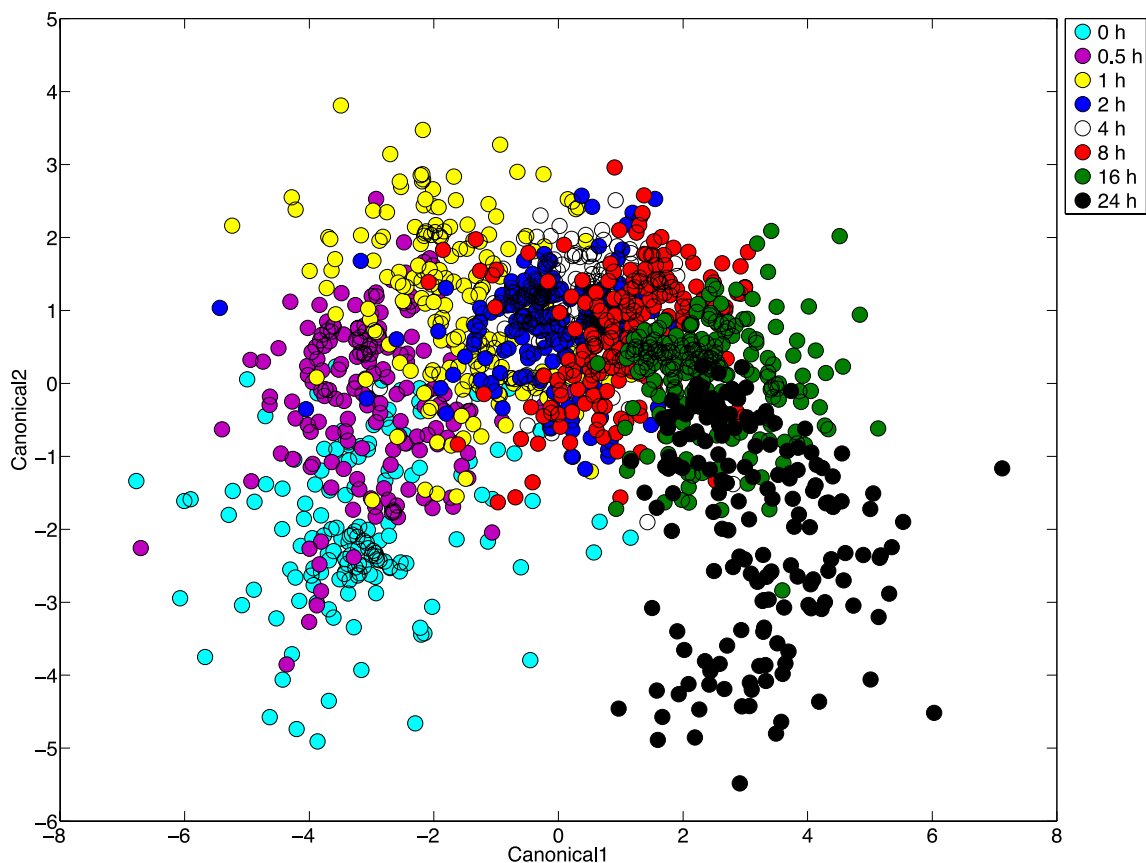


**Figure 9.** Multivariate statistical analysis of all livers. All data points for livers perfused under conditions A, B, and C discriminated by time.

### *Establishing a measure of time-dependent liver health*

The combination of PCA spectral reduction and DA was performed with respect to time along one-dimension (as opposed to the two-dimension analysis of Fig. 3d) for the initial three livers exposed to perfusion conditions A (70-30 mmHg, 3°C), B (110-70 mmHg, 25°C), and C (70-30 mmHg, 25°C). The purpose of this analysis was to quantify the rate(s) at which each liver transitioned between its initial and final states. The average of each cluster was calculated along the one-dimensional space, and its distance was calculated from the averaged value from the initial and final time points. This allowed calculation of the “fraction of degradation,” which is defined

as the distance of a sample from the initial time point per the distance between the initial and final time points. This provides a time-dependent progression of each liver from its initial state (i.e., 0 h) to its final state (i.e., 24 h). DA with time, given clear initial and final organ states (i.e., 0 and 24 h), revealed the dynamics of how the liver changed with respect to time. Clear trends were established and significant differences were observed with treatment conditions. The liver from condition A (70-30 mmHg, 3°C) degraded rapidly, with the sample at 2 h nearly mimicking the sample at 16 h, and both were located much closer to the 24 h sample than the 0 h sample (Fig. 10a). In particular, the sample taken at 4 h revealed 76% degradation of the liver from its initial state (0 h) to its final state (24 h). Until proper metrics are established, it can be assumed that 0 h represents a “healthy” state and the 24 h sample represents an “unhealthy” liver. The liver from condition B (110-70 mmHg, 25°C) showed slower degradation relative to the liver of condition A (70-30 mmHg, 3°C). The sample from the liver under condition B (110-70 mmHg, 25°C) taken at 4 h revealed 63% degradation from the initial to final state (Fig. 10b). Finally, liver of condition C (70-30 mmHg, 25°C) showed a prolonged period of time where the liver more closely resembled the initial “healthy” state rather than the final “unhealthy” state (Fig. 10c). In this case, only 23% degradation was observed at 4 h. However, it must be noted, that this analysis only shows the dynamics of the degradation of a liver from its initial to final state. The final states of the three livers are all different, and their initial states are different as well, since all three livers came from separate animals. In fact, the analyses of Figs. 3b and 3c indicate the final states of the livers perfused with conditions A (70-30 mmHg, 3°C) and C (70-30 mmHg, 25°C) are more closely matched than the livers perfused with conditions B (110-70 mmHg, 25°C) and C (70-30 mmHg,

25°C), despite the fact that the livers with conditions A (70-30 mmHg, 3°C) and C (70-30 mmHg, 25°C) underwent significantly different rates of degradation.

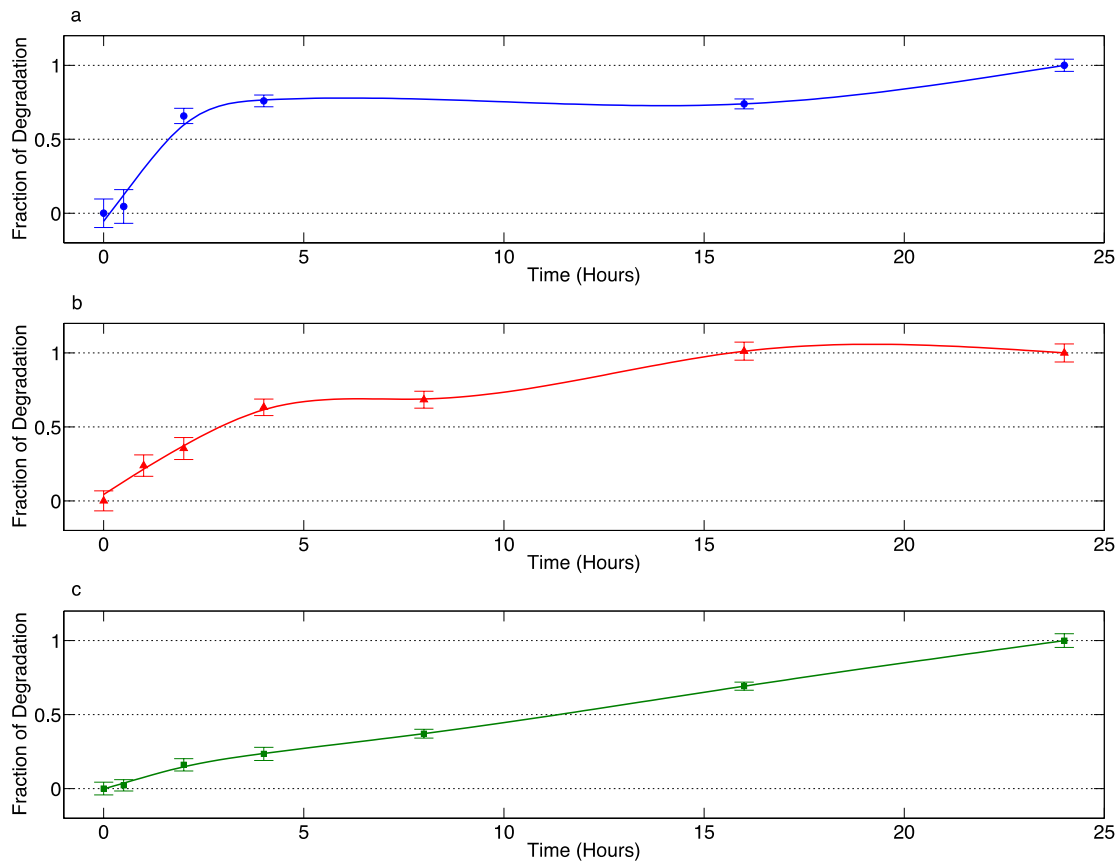


**Figure 10.** One-dimensional linear discriminant analysis by time for livers perfused under conditions (a) A, (b) B, and (c) C. The initial state of each liver is denoted by the “Fraction of Degradation” equal to 0, and the final state has a value equal to 1.

### ***Correlating Raman bands with GC-FID FAME analysis results***

FAME analysis data were collected for the time-course perfusate samples taken from a representative liver from all three sets of perfusion conditions. Changes were observed for saturated and unsaturated fatty acids content of the perfusate fluid for the three livers analyzed.

Results are shown in Fig. 11a for saturated fatty acids and Fig. 11b for unsaturated fatty acids. The overall saturated and unsaturated fatty acid content remained relatively constant for livers perfused under conditions B (110-70 mmHg, 25°C) and C (70-30 mmHg, 25°C). The liver perfused with condition A (70-30 mmHg, 3°C) exhibited a higher fatty acid content, and 3-4 fold increases were observed over the time-course. This is also consistent with its elevated rate of degradation (Fig. 10a). Correlations of these data with Raman spectra were sought. Similar comparisons were performed for bacteria and high correlations ( $R > 0.85$ ) were identified between Raman and GC-FID data (35). In the case of perfusate fluid, the Raman band intensities showing correlation after 4 h of perfusion were: (i)  $2850\text{ cm}^{-1}$  (indicative of  $\text{CH}_2$  symmetric stretch of lipids (38)) for saturated fatty acids (Fig. 11d) and (ii)  $1655\text{ cm}^{-1}$  (indicative of  $\text{C}=\text{C}$  bonds (38)) for unsaturated fatty acids (Fig. 11e). While perfect correlations were not obtained (especially before 4 h), general trends were captured after 4 h of perfusion, and the liver perfused with condition A (70-30 mmHg, 3°C) was shown by both FAME analysis and Raman band analysis to have higher amounts of both saturated and unsaturated fatty acids in the perfusates. However, the Raman band analysis failed to effectively capture trends prior to 4 h of perfusion and overall correlation coefficients between FAME and Raman data were low ( $R < 0.5$ ). However, Raman spectroscopy shows promise for tracking the presence of saturated and unsaturated fatty acids in liver perfusate after 4 h in near real-time.

### ***Correlating Raman bands with total protein measurements***

In addition to fatty acids, protein is another major constituent of liver tissue that was expected to accumulate in the perfusion fluid with organ degradation. A comparison of the total protein content of perfusion fluid from livers of each set of perfusion conditions may provide further indication of their physical states. Livers exposed to condition B (110-70 mmHg, 25°C)

were perfused at higher pressure and temperature and showed slightly higher protein content in the perfusion fluid; however, livers from all three sets showed increases in perfusate protein content of ~50% over the course of 24 h (Fig. 11c). Raman signatures were also sought with good correlation to total protein measurements. Results are shown in Fig. 11f for the Raman band intensity at  $1450\text{ cm}^{-1}$ , which has been associated with C-H deformation in amino acid side chains (38). Similar to the results for fatty acids, good overall trends were observed between protein content measured using standard experimental procedure and Raman spectroscopy, but low correlation coefficients were observed (average  $R = 0.32$ ). These results suggest that time-course Raman band analysis can provide only a low confidence estimate of total protein in liver perfusate. However, this measurement can be obtained in near real-time, which is significant for time-sensitive applications such as organ transplantation. Analyses for specific protein markers indicative of liver failure may yield better correlation with Raman data, but these have not yet been investigated.

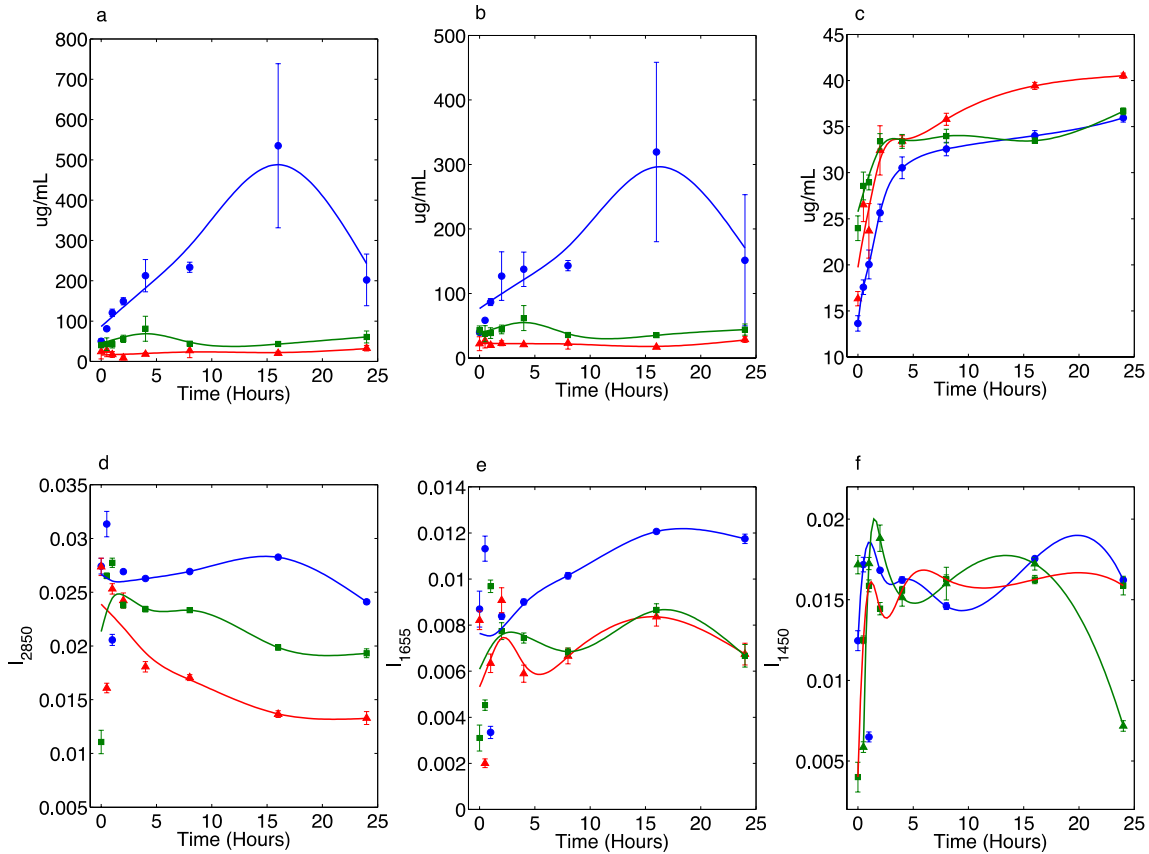


**Figure 11.** (a) Saturated fatty acids measured by GC-FID, (b) unsaturated fatty acids measured by GC-FID, (c) experimental measurements of total protein, (d) saturated fatty acids measured by Raman spectroscopy using peak intensity at 2850 cm<sup>-1</sup>, (e) unsaturated fatty acids measured by Raman spectroscopy using peak intensity at 1655 cm<sup>-1</sup>, (f) total protein measured by Raman spectroscopy using peak intensity at 1450 cm<sup>-1</sup>. Livers perfused under conditions A (blue-solid line), B (red line) and C (green line) are represented in each plot.

## DISCUSSION

Raman spectroscopy as a diagnostic tool for near real-time analysis of cells, tissues, and organs has many potential applications. Here, Raman spectroscopy was applied to monitor porcine liver health during *ex vivo* perfusion using the VasoWave<sup>®</sup> system. Clear distinctions were

observed between perfused and un-perfused organs, and significant changes were detected in the perfusate based on perfusion conditions (i.e., pressure and temperature) and over the 24 h perfusion time-course. It is suspected that the Raman spectra of the un-perfused samples remained dominated by stagnant blood; whereas, perfused livers were quickly cleared of residual blood and debris and Raman spectra of perfusate was likely characterized by metabolic byproducts of organ degradation. We have noted similar results in cardiac tissue and kidney perfusate samples (unpublished results). Donor livers preserved for transplantation are known to have a limited lifetime that is on the order of hours. Continuous real-time monitoring of overall organ health is critical because often the transplantation window does not allow for comprehensive off-line analytical analyses to determine if an organ is a good candidate for transplantation. In addition, real-time diagnostics have the potential to allow for continuous monitoring while the organ is in transit as well as in the operating room. The dynamics of organ degradation over the first few hours of *ex vivo* perfusion may very well provide critical information regarding the long-term viability of the transplanted organ and patient. The Raman-based diagnostic tool presented here provides “near” real-time analysis. The time delay is on the order of seconds ( $< 240$  s) and consists of (i) drying time for a 10  $\mu$ L spot sample, (ii) Raman scanning of several points of the sample, and (iii) computations. It is anticipated that Raman technologies capable of repeatable liquid phase analysis will further reduce this time delay, but liquid measurements led to inconsistent results in this research (data not shown). The use of a 532 nm laser was also required to produce reliable results. Great care must be taken when operating at higher energies due to the risk of graphitization (39). This was managed by (i) using a short integration time (10 s), (ii) scanning different areas of the sample, and (iii) looking for a wide graphitization band around  $1500\text{ cm}^{-1}$  in the Raman spectra.

In this research, a perfused porcine liver was compared with a non-perfused liver and six additional livers were subjected to three sets of perfusion pressures and temperatures and monitored over the time-course of *ex vivo* perfusion using the VasoWave<sup>®</sup>. While significant differences were detected and trends were repeatable in replicates, the sample size is too small to make conclusive statements regarding the effects of perfusion conditions. However, the purpose of this study was to develop and demonstrate Raman spectroscopy with multivariate statistical analysis as a potential near real-time diagnostic tool for monitoring organ health by analyzing perfusate. Since inherent variability exists in different livers, it is likely that individual liver characteristics played a role in its rate of degradation, along with the varied perfusion parameters of the VasoWave<sup>®</sup>. Large-scale studies are underway and will be used along with clinical diagnostics to distinguish between “healthy” and “unhealthy” organs for transplantation.

The use of Raman spectroscopy as a near real-time diagnostic tool requires significant raw data processing and statistical analysis. In the case of complex biological fluids, as observed in liver degradation during *ex vivo* perfusion, we argue for the use of a multivariate statistical analysis approach that makes use of entire Raman spectra rather than comparing intensities of individual bands. Individual band analysis assumes no interference from molecules with similar chemical structures and functional groups. This is ideal for closed systems where all possibilities are known; however, the chemistry of a diseased and/or degrading liver can be extremely complex. Raman bands identified for fatty acids and protein in this research must be further verified in large-scale studies and may ultimately yield less useful information than a holistic multivariate analysis since this approach takes into account all molecular signatures that are changing among all Raman spectra. Thus, it is anticipated that the multivariate statistical analysis approach will best characterize a changing complex system. Regardless of whether Raman band analysis for fatty

acids or multivariate statistical analysis proves more beneficial in large-scale studies, both may ultimately have use in time-sensitive applications, such as in organ transplantation. As shown with the Raman band correlations with fatty acid and protein data, sacrificing accuracy for near real-time information is required, but this trade-off may be worthwhile. Furthermore, it is reasonable to speculate that further advances in Raman spectroscopy instrumentation, measurement techniques, and data analysis methods will enhance the accuracy of near real-time measurements.

Even though Raman spectroscopy proved valuable in monitoring the differentiation of porcine liver perfusate fluid in near-real time, challenges still remain to definitively link these changes with organ health. However, the ability to monitor changes in the complex chemistry of a dynamic system, such as a degrading liver, is novel and has significant future medical applications. As additional porcine and human livers are analyzed, a database will be constructed linking Raman signatures to the clinical pathophysiology of these organs. With this information, additional multivariate statistical measures and artificial intelligence models will enable the linking of the changes in Raman spectra to true measures of organ health. This is critical near real-time information that will ultimately be used by surgeons and clinicians when making the critical decision of whether an organ is sufficiently healthy for transplantation into a recipient patient.

## REFERENCES

1. **US Department of Health & Human Services** 2014, posting date. <http://optn.transplant.hrsa.gov/latestData/rptData.asp>. [Online.]
2. **Mitchell AE, Colvin HM, Palmer Beasley R.** 2010. Institute of Medicine recommendations for the prevention and control of hepatitis B and C. *Hepatology* **51**:729-733.
3. **Centers for Disease Control and Prevention** 2014, posting date. *Viral Hepatitis Statistics & Surveillance*. [Online.]
4. **World Health Organization** 2014, posting date. Media Center: Hepatitis B and Hepatitis C. [Online.]
5. **Mann RE, Smart RG, Govoni R.** 2003. The epidemiology of alcoholic liver disease. *Alcohol Research and Health* **27**:209-219.
6. **Nahon P, Kettaneh A, Tengher-Barna I, Ziol M, de Ledinghen V, Douvin C, Marcellin P, Ganne-Carrie N, Trinchet JC, Beaugrand M.** 2008. Assessment of liver fibrosis using transient elastography in patients with alcoholic liver disease. *Journal of hepatology* **49**:1062-1068.
7. **Ratziu V, Charlotte F, Heurtier A, Gombert S, Giral P, Bruckert E, Grimaldi A, Capron F, Poynard T.** 2005. Sampling variability of liver biopsy in nonalcoholic fatty liver disease. *Gastroenterology* **128**:1898-1906.
8. **Akamatsu N, Sugawara Y.** 2012. Liver transplantation and hepatitis C. *International journal of hepatology* **2012**:686135.
9. **Crippin JS, McCashland T, Terrault N, Sheiner P, Charlton MR.** 2002. A pilot study of the tolerability and efficacy of antiviral therapy in hepatitis C virus-infected patients

- awaiting liver transplantation. Liver transplantation : official publication of the American Association for the Study of Liver Diseases and the International Liver Transplantation Society **8**:350-355.
10. **Sano MB, Neal RE, 2nd, Garcia PA, Gerber D, Robertson J, Davalos RV.** 2010. Towards the creation of decellularized organ constructs using irreversible electroporation and active mechanical perfusion. Biomedical engineering online **9**:83.
  11. **Canbay A, Higuchi H, Bronk SF, Taniai M, Sebo TJ, Gores GJ.** 2002. Fas enhances fibrogenesis in the bile duct ligated mouse: a link between apoptosis and fibrosis. Gastroenterology **123**:1323-1330.
  12. **Keeffe EB.** 2001. Liver transplantation: current status and novel approaches to liver replacement. Gastroenterology **120**:749-762.
  13. **Le Dinh H, de Roover A, Kaba A, Lauwick S, Joris J, Delwaide J, Honore P, Meurisse M, Detry O.** 2012. Donation after cardio-circulatory death liver transplantation. World journal of gastroenterology : WJG **18**:4491-4506.
  14. **Duffy JP, Vardanian A, Benjamin E, Watson M, Farmer DG, Ghobrial RM, Lipshutz G, Yersiz H, Lu DS, Lassman C.** 2007. Liver transplantation criteria for hepatocellular carcinoma should be expanded: a 22-year experience with 467 patients at UCLA. Ann Surg **246**:502.
  15. **Kamath PS, Wiesner RH, Malinchoc M, Kremers W, Therneau TM, Kosberg CL, D'Amico G, Dickson ER, Kim W.** 2001. A model to predict survival in patients with end-stage liver disease. Hepatology **33**:464-470.
  16. **Taylor MJ, Baicu SC.** 2010. Current state of hypothermic machine perfusion preservation of organs: the clinical perspective. Cryobiology **60**:S20-S35.

17. **Dutkowski P, de Rougemont O, Clavien PA.** 2008. Machine perfusion for 'marginal' liver grafts. *American journal of transplantation : official journal of the American Society of Transplantation and the American Society of Transplant Surgeons* **8**:917-924.
18. **Monbaliu D, Brassil J.** 2010. Machine perfusion of the liver: past, present and future. *Current opinion in organ transplantation* **15**:160-166.
19. **Fuller BJ, Lee CY.** 2007. Hypothermic perfusion preservation: the future of organ preservation revisited? *Cryobiology* **54**:129-145.
20. **Moers C, Smits JM, Maathuis MH, Treckmann J, van Gelder F, Napieralski BP, van Kasterop-Kutz M, van der Heide JJ, Squifflet JP, van Heurn E, Kirste GR, Rahmel A, Leuvenink HG, Paul A, Pirenne J, Ploeg RJ.** 2009. Machine perfusion or cold storage in deceased-donor kidney transplantation. *The New England journal of medicine* **360**:7-19.
21. **Wight JP, Chilcott JB, Holmes MW, Brewer N.** 2003. Pulsatile machine perfusion vs. cold storage of kidneys for transplantation: a rapid and systematic review. *Clinical transplantation* **17**:293-307.
22. **Taylor MJ, Baicu SC.** 2010. Current state of hypothermic machine perfusion preservation of organs: The clinical perspective. *Cryobiology* **60**:S20-35.
23. **Gerber D, Orlando G.** 2013. Personal communications to Dr. John Robertson.
24. **Haka AS, Shafer-Peltier KE, Fitzmaurice M, Crowe J, Dasari RR, Feld MS.** 2005. Diagnosing breast cancer by using Raman spectroscopy. *Proc Natl Acad Sci U S A* **102**:12371-12376.
25. **Frank CJ, McCreery RL, Redd DC.** 1995. Raman spectroscopy of normal and diseased human breast tissues. *Anal Chem* **67**:777-783.

26. **Chan JW, Taylor DS, Zwerdling T, Lane SM, Ihara K, Huser T.** 2006. Micro-Raman spectroscopy detects individual neoplastic and normal hematopoietic cells. *Biophys J* **90**:648-656.
27. **Krishna CM, Sockalingum GD, Kegelaer G, Rubin S, Kartha VB, Manfait M.** 2005. Micro-Raman spectroscopy of mixed cancer cell populations. *Vibrational Spectroscopy* **38**:95-100.
28. **Mahadevan-Jansen A, Mitchell MF, Ramanujam N, Malpica A, Thomsen S, Utzinger U, Richards-Kortum R.** 1998. Near-infrared Raman spectroscopy for in vitro detection of cervical precancers. *Photochemistry and photobiology* **68**:123-132.
29. **Bar-Or R, Rael LT, Curtis CG, Mains CW, Slone DS, Bar-Or D.** 2009. Raman spectral signatures of human liver perfusates correlate with oxidation reduction potential. *Molecular medicine reports* **2**:175-180.
30. **Ramser K.** 2012. Raman spectroscopy of single cells for biomedical applications. *Applications of Raman spectroscopy to biology-from basic studies to disease diagnosis*],(Ghomi, M., Ed.), IOS Press, Amsterdam:106-147.
31. **Pienaar BH, Lindell SL, Van Gulik T, Southard JH, Belzer FO.** 1990. Seventy-two-hour preservation of the canine liver by machine perfusion. *Transplantation* **49**:258-260.
32. **Yamamoto N, Konishi Y, Wakashiro S, Takayasu T, Tatsumi Y, Shimahara Y, Tanaka K, Yamaoka Y, Ozawa K.** 1991. Seventy-two-hour preservation of porcine liver by continuous hypothermic perfusion with UW solution in comparison with simple cold storage. *The Journal of surgical research* **51**:288-292.

33. **Sano MB, Neal R, Garcia P, Gerber D, Robertson J, Davalos R.** 2010. Towards the creation of decellularized organ constructs using irreversible electroporation and active mechanical perfusion. *Biomedical engineering online* **9**:83.
34. **Collakova E, Aghamirzaie D, Fang Y, Klumas C, Tabataba F, Kakumanu A, Myers E, Heath LS, Grene R.** 2013. Metabolic and Transcriptional Reprogramming in Developing Soybean (*Glycine max*) Embryos. *Metabolites* **3**:347-372.
35. **Zu TN, Athamneh AI, Wallace RS, Collakova E, Senger RS.** 2014. Near real-time analysis of the phenotypic responses of *Escherichia coli* to 1-butanol exposure using Raman spectroscopy. *Journal of bacteriology*.
36. **Athamneh AI, Alajlouni RA, Wallace RS, Seleem MN, Senger RS.** 2014. Phenotypic profiling of antibiotic response signatures in *Escherichia coli* using Raman spectroscopy. *Antimicrobial agents and chemotherapy* **58**:1302-1314.
37. **Yuan X, Theruvath AJ, Ge X, Floerchinger B, Jurisch A, Garcia-Cardena G, Tullius SG.** 2010. Machine perfusion or cold storage in organ transplantation: indication, mechanisms, and future perspectives. *Transplant international : official journal of the European Society for Organ Transplantation* **23**:561-570.
38. **Movasaghi Z, Rehman S, Rehman IU.** 2007. Raman spectroscopy of biological tissues. *Applied Spectroscopy Reviews* **42**:493-541.
39. **Puppels GJ, Olminkhof JH, Segers-Nolten GM, Otto C, de Mul FF, Greve J.** 1991. Laser irradiation and Raman spectroscopy of single living cells and chromosomes: sample degradation occurs with 514.5 nm but not with 660 nm laser light. *Experimental cell research* **195**:361-367.

## CHAPTER FOUR

# **A study of the phenotypic responses of *Escherichia coli* to multiple 4-carbon alcohols using Raman spectroscopy**

(Manuscript to be submitted to Journal of Bacteriology in October 2014)

Theresah N. K. Zu<sup>1</sup>, Ahmad I. M. Athamneh, and Ryan S. Senger<sup>1,#</sup>

<sup>1</sup>Department of Biological Systems Engineering; Virginia Tech; Blacksburg, VA 24061

#Corresponding author

Corresponding author email address: senger@vt.edu

# A study of the phenotypic responses of *Escherichia coli* to multiple 4-carbon alcohols using Raman spectroscopy

## ABSTRACT

The phenotypic responses of *E. coli* cells exposed to 1.2% (v/v) of 1-butanol, 2-butanol, isobutanol, tert-butanol, and 1,4-butanediol were studied in near real-time using Raman spectroscopy. A novel method of “chemometric fingerprinting” was developed that uses multivariate statistics (principal component analysis and linear discriminant analysis) to identify phenotypic changes over a 180-min time course. A toxicity study showed extreme variability among the reduction in culture growth, with 1-butanol showing the greatest toxicity and 1,4-butanediol showing relatively no toxicity. Chemometric fingerprinting showed distinct phenotype clusters according to the type of alcohol: (i) 1-butanol and 2-butanol (straight chain alcohols), (ii) isobutanol and tert-butanol (branched chain alcohols), and (iii) control and 1,4-butanediol (no terminal alkyl end) treated cells. While the isobutanol- and tert-butanol-treated cells showed similar phenotypes, isobutanol was significantly more toxic than tert-butanol. In addition, the phenotypic response was found to take place largely within 60 min of culture treatment; however, significant responses (especially for 1,4-butanediol) were still occurring at 180 min post-treatment. The methodology described here identified different phenotypic responses to seemingly similar 4-carbon alcohols and can be used to study phenotypic responses of virtually any cell type under any set of environmental conditions or genetic manipulations.

## INTRODUCTION

### *Phenotyping with Raman spectroscopy*

Recently, the power of Raman spectroscopy for near real-time phenotyping was demonstrated by the analysis of *Escherichia coli* DH5 $\alpha$  cells exposed to 1.2% 1-butanol (1). Raman spectral data for control and butanol-exposed cultures were correlated with GC-MS/FID analyses of fatty acids. Consistent trends were observed for changes in saturated, unsaturated, and cyclopropane fatty acids with butanol exposure over time. Raman bands (i.e. spectral peaks) were correlated with results from other standard analytical methods, including: (i) fluorescence anisotropy measurements of membrane fluidity, (ii) total protein content, and (iii) total amino acid content. Although some accuracy was sacrificed with analysis by Raman spectroscopy, these phenotyping results were obtained in near real-time within seconds. The analysis required minimal sample preparation and was label-free. In the current research, the study was expanded to include several 4-carbon alcohols: (i) 1-butanol, (ii) 2-butanol, (iii) isobutanol, (iv) tert-butanol, and (v) 1,4-butanediol. In addition, multivariate statistics (i.e., principal component analysis (PCA) and linear discriminant analysis (LDA)) were included with the data analysis to identify similar and significantly different phenotypic responses of *E. coli* cells exposed to different alcohols.

### *Conventional uses of Raman spectroscopy to analyze biological samples*

Cellular chemical composition includes free solutes and macromolecules (e.g., proteins, DNA/RNA, lipids, cell walls, and carbon storage polymers) that change significantly in response to environmental perturbations (2-4). Furthermore, conventional analytical techniques (e.g., chromatography) must (i) be performed off-line, (ii) require significant time and resources, and (iii) cause destruction of the sample. Raman spectroscopy has demonstrated the capability to measure phenotypic responses of *E. coli* cell culture to 1-butanol toxicity in near real-time (1).

Raman spectroscopy has also been applied to other purposes, including (among many others) (i) species characterization (5), (ii) distinction of stem cells from differentiating cells (6), (iii) identification of multidrug resistance phenotype in cancer cells (7), and (iv) identification of the mechanism of action of antimicrobial compounds (8). Extensive Raman band assignment libraries and intensities for biological molecules are available (9-16). However, these databases often differ in assignments for the same Raman band (e.g. the bands at 1449, 1660, and 2940  $\text{cm}^{-1}$  have been assigned to both proteins and lipids). This is often the case with biological samples where band overlap is present, making the band assignments highly ambiguous. Recently, a new database was published that consists of a large compilation from a broad spectrum of the literature (17). However, most band assignments cited in this database were obtained from organs and tissues, and it is unclear how well they apply to bacteria. This represents a significant challenge in Raman spectroscopy research. Thus, the approach is to use the entire Raman spectrum (instead of individual Raman bands) as a “chemometric fingerprint” of a cell and use multivariate statistics for clustering and classification of phenotypes. This approach is designed to avoid some of the ambiguity associated with Raman band assignments.

### ***Toxicity mechanisms of alcohols***

Toxicity is a major impediment in the alcohol biofuel fermentation process, as alcohols significantly inhibit microbial growth (18-20). For example, during the production of isobutanol in *E. coli*, growth is retarded by concentrations as low as 1% (v/v) (21). In the presence of an alcohol, the *E. coli* cell membranes change radically in fatty acid composition. This is significant, considering that the inner plasma membrane consists of about 75% lipids and 25% protein by weight. Toxicity is thought to be inversely proportional to fatty acid chain length, and the same is true for the concentration of alcohol needed to cause an observable change in fatty acid

composition of the cell (22). This is in an agreement with the argument that alcohol toxicity can be predicted by its octanol-water partition coefficient ( $K_{OW}$ ) (23). Hydrophobic molecules have high  $K_{OW}$  values, and organic solvents with  $\log K_{OW}$  values greater than 1.5 have proven to be extremely toxic to microbes as they partition the cytoplasmic membrane, resulting in a loss of membrane structure and function as well as membrane leakage (24). It has been proposed that the cell membrane bears the most impact with the addition of organic solvents and plays a significant role in the cellular adaptation to stress. In addition, short-chain alcohols cause desiccation by absorbing water, while long-chain alcohols that do not mix with water penetrate the lipid bilayers of membranes (23). Alcohol toxicity causes increased cell membrane fluidity, altered regulation of internal pH, disruption of protein-lipid interactions, electron transport chain that generates ATP, respiration, and decreased energy generation by the inhibition of glucose and nutrient transport (21, 25, 26). Microbes use several regulatory feedback mechanisms to respond to alcohol toxicity and optimize the use of resources in an attempt to maintain homeostasis (27). The following alcohol toxicity responses have been elucidated: (i) altered cytoplasmic membrane as well as cell surface properties; (ii) altered cell envelope protein composition; (iii) changed peptidoglycan, membrane lipid, and lipopolysaccharide (LPS) compositions; and (iv) synthesis of protective metabolites and solvent efflux pumps (25, 26).

### ***Phenotypic responses to 4-carbon alcohols***

Four different butanol isomers (1-butanol, 2-butanol, isobutanol, and *tert*-butanol) along with 1,4-butanediol are shown in Fig. 1. 1-Butanol is produced natively through fermentation by *Clostridium* (e.g. both *C. acetobutylicum* and *C. beijerinckii*) (28, 29). Metabolic pathway engineering enabled the production of isobutanol (30) and 1,4-butanediol (31). The present study builds on the published study with 1-butanol (1) by incorporating additional phenotypic responses

with other 4-carbon alcohols and by introducing multivariate statistics (PCA and DA) for identifying phenotypic responses by chemometric fingerprinting. *E. coli* cultures at the onset of the exponential growth phase were subjected to 1.2% v/v of the different 4-carbon alcohols, and sampling was performed over a 180-minute period. *E. coli* cells have a very complex and dynamic physiology that changes constantly over the growth period and respond to environmental stimuli. Capturing these changes using current off-line experimental methods has been challenging. Analysis by Raman spectroscopy allows for a near real-time analysis, but challenges remain in deconvoluting complicated Raman spectra into their chemical compositions. This is complicated by the ambiguity of Raman band assignments that appear in the literature. The chemometric fingerprinting approach presented here provides a new way to use Raman spectroscopy in phenotyping. No Raman band assignments are considered. Instead, the entire Raman spectrum of a sample is used in the characterization of the phenotype of the cell. Knowledge of phenotypes of cells representing a “healthy state” and “stressed state” are used in clustering analysis, which is particularly useful in phenotype characterization. The purpose was to develop a new methodology for tracking phenotypic changes in microbes in near real-time. The study was performed with 4-carbon alcohols because of the wide ranges of toxicity exhibited and their importance to renewable biofuel and chemical production.

## **MATERIALS AND METHODS**

### ***Bacteria strain and chemicals***

*E. coli* DH5 $\alpha$  cells were used in all experiments and were obtained from Invitrogen Life Technologies (Grand Island, NY). Frozen stock cultures were plated onto solid agar plates prior

to experiments or otherwise were stored in glycerol at  $-80^{\circ}\text{C}$ . All chemicals were purchased from Sigma-Aldrich (St. Louis, MO) and were of at least 99% purity.

### ***Culture conditions***

*E. coli* cells were grown in LB media containing tryptone (10 g/L), yeast extract (5 g/L), and sodium chloride (10 g/L) as previously described (1). Cultures were grown at  $37^{\circ}\text{C}$  and agitated in a rotary shaker at 210 RPM. Culture optical density was measured at 600 nm ( $\text{OD}_{600}$ ). Subcultures were prepared by diluting 100  $\mu\text{L}$  of culture with 25 mL fresh LB media. At the onset of the exponential growth phase ( $\text{OD}_{600}$  of 0.4 – 0.5), the culture was split into six equal portions (5 mL each), with one serving as the negative control. The different alcohols: 1-butanol, 2-butanol, isobutanol, tert-butanol, and 1,4-butanediol were added to the respective cultures to a concentration of 1.2% v/v. All cultures were re-incubated for 60 min prior to sampling. Samples (250  $\mu\text{L}$ ) were taken every 30 min from all cultures for a total of 180 min. Cells were centrifuged at 10,000 rpm at  $4^{\circ}\text{C}$  for 5 min and washed with ice cold deionized water. This process was repeated five times. The cells were re-suspended in 250  $\mu\text{L}$  of purified water for Raman analysis.

### ***Raman spectroscopy***

Raman spectroscopy was performed as published previously (1, 8), except that the analysis required 50  $\mu\text{L}$  of washed cells. In short, cells were dried at room temperature on an aluminum surface and analyzed using a Bruker Senterra dispersive Raman spectrometer, which was attached to a confocal microscope (100x magnification) and equipped with OPUS software (Bruker Optics, Billerica, MA). Laser excitation of 532 nm (20 mW) was applied for 10 seconds and had spectral resolution of 9-15  $\text{cm}^{-1}$ . Each sample was scanned at least 50 times and spectra were averaged. All data analysis was carried out in OPUS (baseline correction) and MATLAB (R2012A) (MathWorks, Natick, MA). Each sample group (minimum 50 individual scans), was vector normalized over the

entire wavelength range of the spectra (400 – 3200  $\text{cm}^{-1}$ ) (1). PCA allowed for identification of outlier data points, which were then excluded. PCA was then used to reduce the dataset for DA. DA was then applied to the top 9 principal components of the dataset, as described previously (8), in order to separate and cluster samples based on the different phenotypic responses to 4-carbon alcohol exposure.

## RESULTS

### *4-Carbon alcohol toxicity and inhibition of culture growth*

*E. coli* cells were subjected to a 1.2% v/v 1-butanol challenge at the start of the exponential phase ( $\text{OD}_{600} = 0.5-0.6$ ) and showed significantly reduced growth compared to the control (1). To test relative toxicity of different 4-carbon alcohols, 1-butanol and other 4-carbon alcohols, specifically isobutanol, 2-butanol, tert-butanol, and 1,4-butanediol, were applied to *E. coli* cultures at the same levels (1.2% v/v), and the culture  $\text{OD}_{600}$  values were monitored for 180 min. Results are shown in Fig. 1 and dramatic changes in toxicity are apparent. 1-Butanol showed the greatest toxicity, followed by isobutanol, 2-butanol, tert-butanol, and 1,4-butanediol respectively. *E. coli* was tolerant to 1,4-butanediol and tert-butanol, as a small reduction in final  $\text{OD}_{600}$  readings was observed relative to the control culture, to which no alcohol was added. In addition, a clear separation was observed for the more tolerated alcohols (1,4-butanediol and tert-butanol) compared to the more toxic 4-carbon alcohols (1-butanol, isobutanol, and 2-butanol). This suggests that different phenotypic responses are present, and these were investigated further by using Raman spectroscopy.

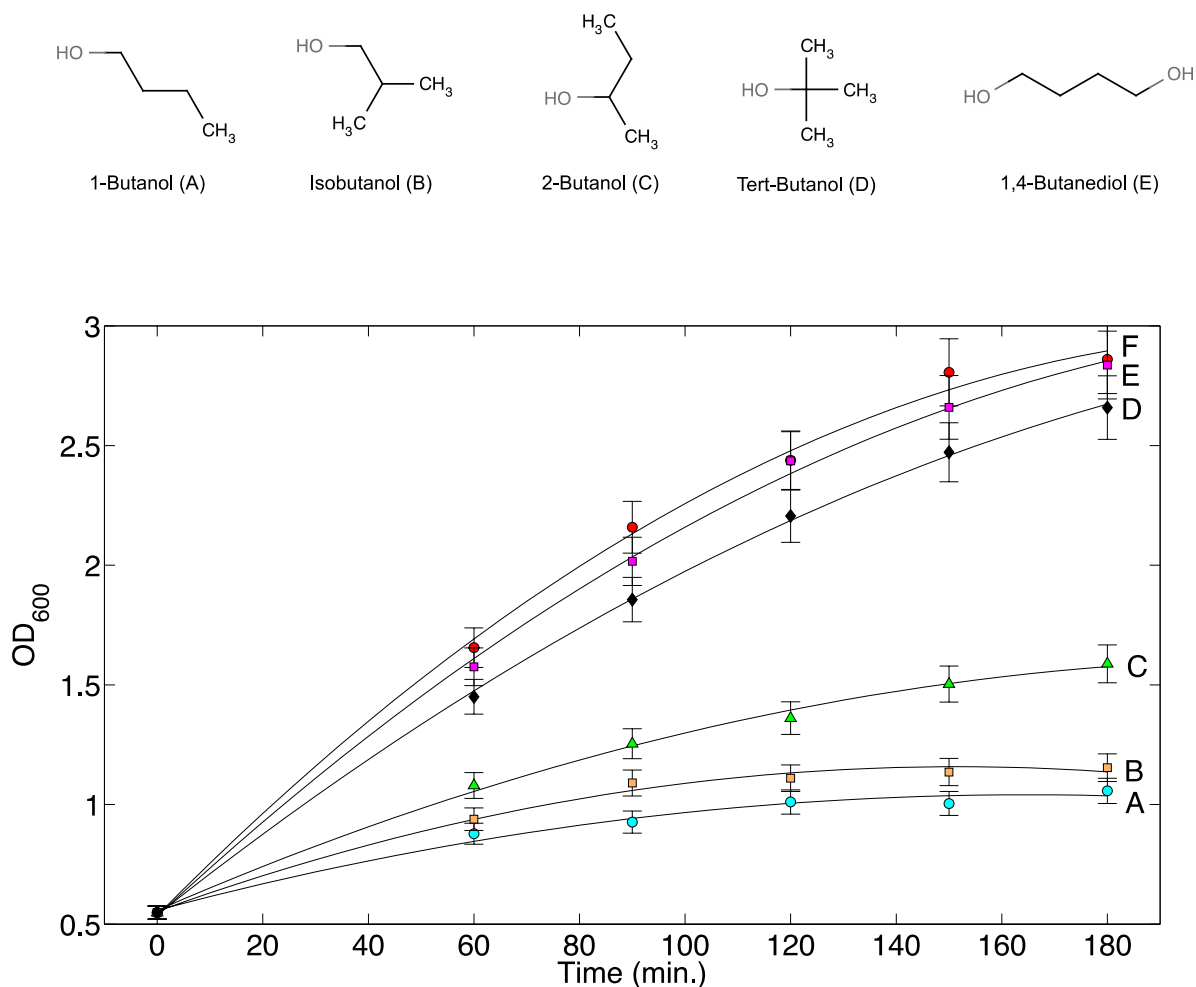


**Figure 1.** Chemical structures of 4-carbon alcohols and *E. coli* growth inhibition. Each alcohol was added to 1.2% v/v at 0 min. Each curve label (A-E) corresponds to the alcohol above. The control culture is labeled F.

### *Normalized Raman spectra*

The different 4-carbon alcohols had different toxicity towards *E. coli* cells and showed different levels of growth inhibition. Highly toxic alcohols are expected to cause significant changes in cellular structure that is expected to have pronounced effects on growth rates. To

associate alcohol toxicity with the changes in cell structure, Raman spectra of cells treated with 1.2% (v/v) of different 4-carbon alcohols were compared to the spectra of control cells (Fig. 2). A visual inspection of the superimposed spectral data (with no statistical analysis), showed differences in regions corresponding to nucleic acids ( $\sim 1070 - 1090 \text{ cm}^{-1}$ ), proteins ( $1449 \text{ cm}^{-1}$ ,  $1655 - 1680 \text{ cm}^{-1}$ ), and lipids ( $1320 \text{ cm}^{-1}$ ,  $1607 \text{ cm}^{-1}$ ) (17) within the biological region (Fig. 2a) and shifts in the CH region (Fig. 2b). The spectral results of Fig. 2 point to the observations that (i) the general shape of the spectra is conserved with exposure to all 4-carbon alcohols and (ii) the differences among the spectra occur in wavenumber ranges assigned in the literature to macromolecules that largely determine specific phenotypes. In the previous study (1), individual Raman peaks were identified and correlated with results from traditional experimental measurements. In this analysis, however, multivariate statistics is used to analyze entire spectra as chemometric fingerprints.

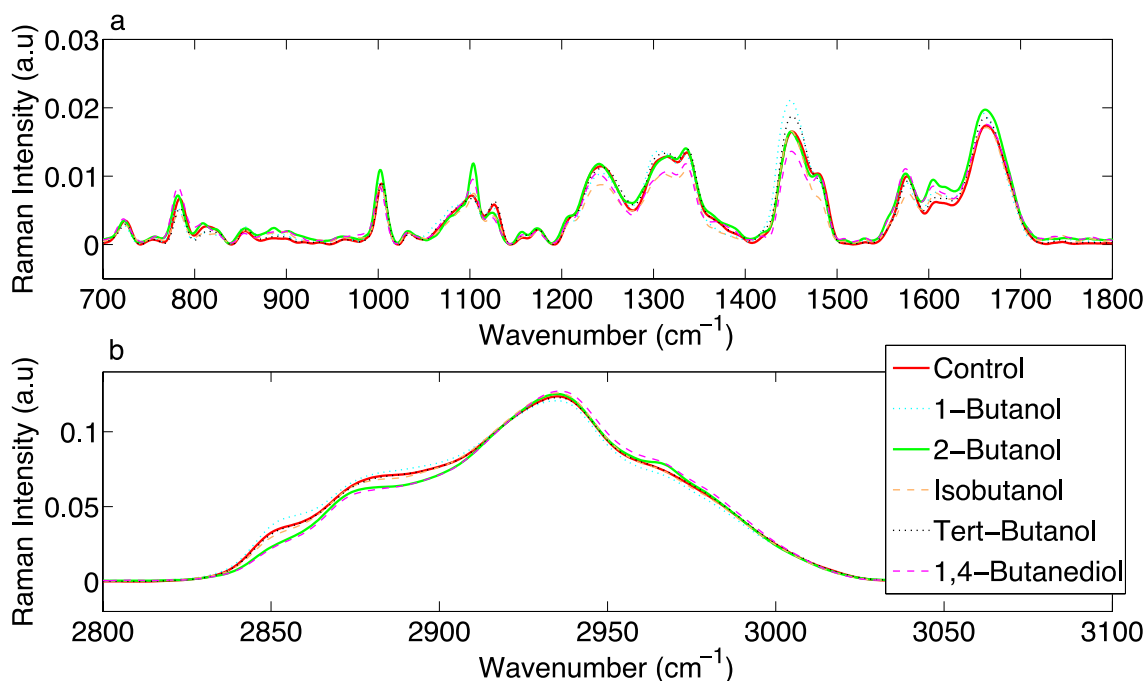


**Figure 2.** Normalized and averaged Raman spectra of the control and alcohol-treated cultures at 180 min over (a) the biological range (700-1800 cm<sup>-1</sup>) and (b) the CH range (2800-3100 cm<sup>-1</sup>).

### *Discriminate analysis by alcohol*

In order to investigate the effect of alkyl chain and branching of the 4-carbon alcohols as relates to toxicity, the Raman spectral dataset was first reduced using PCA to remove outlier scans. Then PCA was used to further reduce the dataset into its top nine principal components for analysis by DA. The DA was first applied for discrimination by alcohol. . Each data point in Fig. 3 represents an entire Raman spectrum. This contains all information about chemical composition in the cell and is a good representation of the cells changing phenotype. Each spectrum has been reduced to its top principal components and then classified by DA to be represented on a 2D canonical plot. Next, DA was performed with respect to alcohol in Fig. 3 to determine the effects of alkyl chain and branching. This means that all time points are represented and grouped

according to the type of alcohol exposure only. Of particular interest in Fig. 3 is that the six datasets (treatment by five alcohols and a non-treated control) separate into 3 clusters on the 2D canonical plot: (i) 1-butanol and 2-butanol (linear chain alcohols), (ii) isobutanol and tert-butanol (branched chain alcohols), and (iii) 1,4-butanediol and the control (no terminal alkyl end). The first cluster (1-butanol and 2-butanol) is intuitive since these are both toxic to *E. coli* cultures (Fig. 1). The third cluster (1,4-butanediol and the control) is also intuitive because little difference is observed in Fig. 1 for these two. The second cluster consists of isobutanol and tert-butanol. Isobutanol showed significant toxicity, while tert-butanol showed much less toxicity to isobutanol (Fig. 1). However, the phenotypes of exposed *E. coli* cells seen as clustered data points in a DA canonical plot were shown to be similar in Fig. 3. This is non-intuitive and suggests that very small molecular changes may be responsible for the differences in toxicity of isobutanol and tert-butanol.

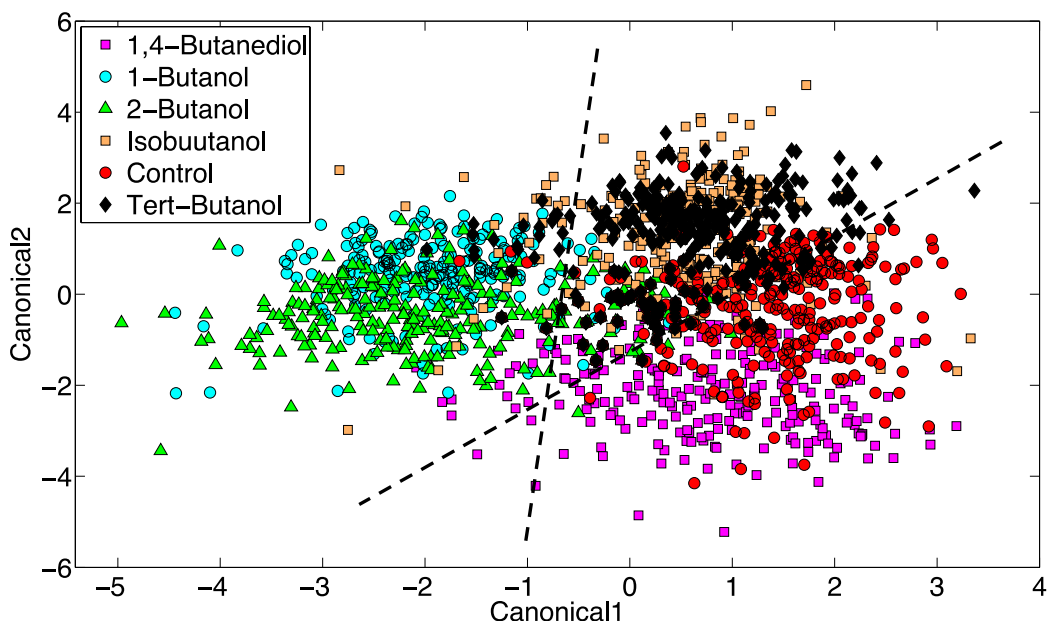


**Figure 3.** DA results by alcohol. Three clusters are identified and consist of (1) 1-butanol and 2-butanol, (2) isobutanol and tert-butanol, and (3) the control and 1,4-butanediol treated cultures.

### *Discriminate analysis by time*

Next, DA was applied to the dataset with respect to time to investigate progression of the observed phenotypic changes. Results are shown in Fig. 4. In this DA, phenotypes resulting from exposure to all alcohols at a specified time point are represented in a 2D canonical plot (Fig. 4). The initial time point (0 min) corresponds to the point, at which the 4-carbon alcohols were added to the culture (during exponential growth). Interestingly, results revealed that the culture toxicity response was almost immediate and was easily detectable within the first 60 minutes following exposure (Fig. 4). From there, though minimal, continued movement of data point clusters away from the initial time point (0 min) was observed, with the final time point (180 min) cluster being

the furthest distance from the initial time point. This analysis provides a means of monitoring the dynamics of phenotype changes when the entire chemical composition of a culture (i.e., the entire Raman spectrum) is considered simultaneously. While this analysis considers all 4-carbon alcohols, the procedure can also be performed on individual time points and alcohols.

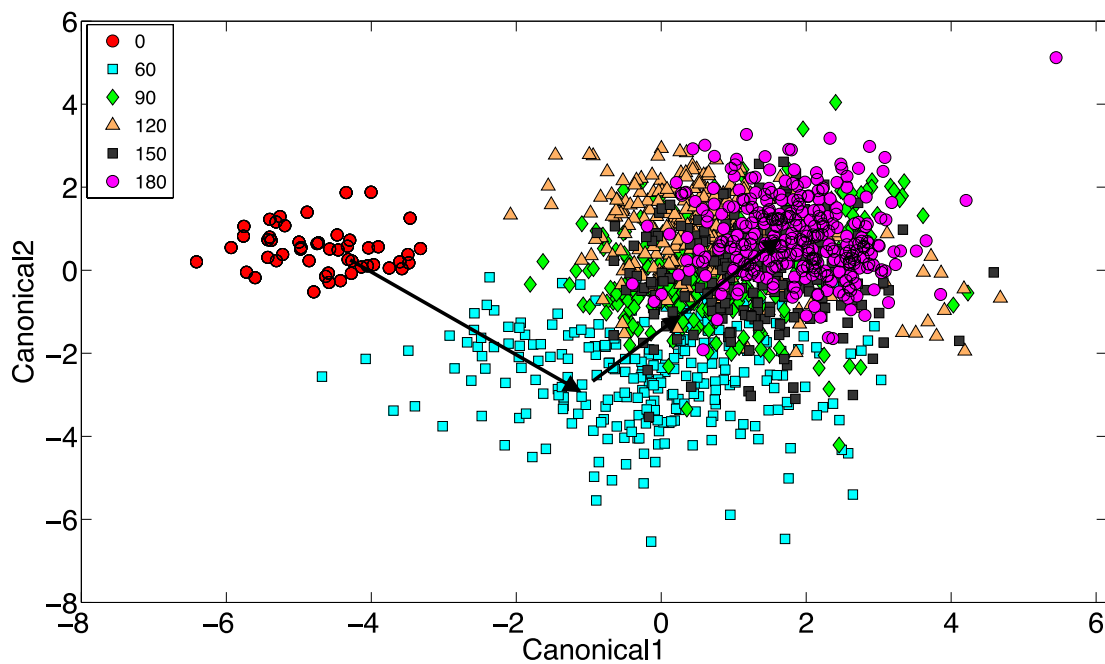


**Figure 4.** DA results by time. The times given in the legend refer to minutes past the addition of an alcohol.

### ***Discriminant analysis by alcohol at multiple time points***

To further illustrate the 4-carbon alcohol induced response mechanism(s), DA was applied with respect to alcohol at single time points (60 and 180 min), as shown in Fig. 5. At 60 min (Fig. 5a), the control and 1,4-butanediol-treated cells are similar as the corresponding data points cluster together. However, at 180 min (Fig. 5b), data points have separated completely on the 2D canonical plot, suggesting a distinctive long-term response compared to data points at 60 min, even though toxicity was not detected (Fig. 1). It is unclear why this is located farther from the control culture than resulting from toxic 1-butanol exposure in Fig. 5b. The short-term response (60 min, Fig. 5a) shows significant separation of 1-butanol, 2-butanol, isobutanol, and tert-butanol, suggesting a significant toxicity response. However, none of these clustered together, which suggests the phenotypic responses to all 4-carbon alcohols are different in the short-term response to the alcohols. It is noted that a significant short-term phenotype response was observed for tert-butanol treated cells (Fig. 5a), but toxicity was much less compared to 1-butanol (Fig. 1).

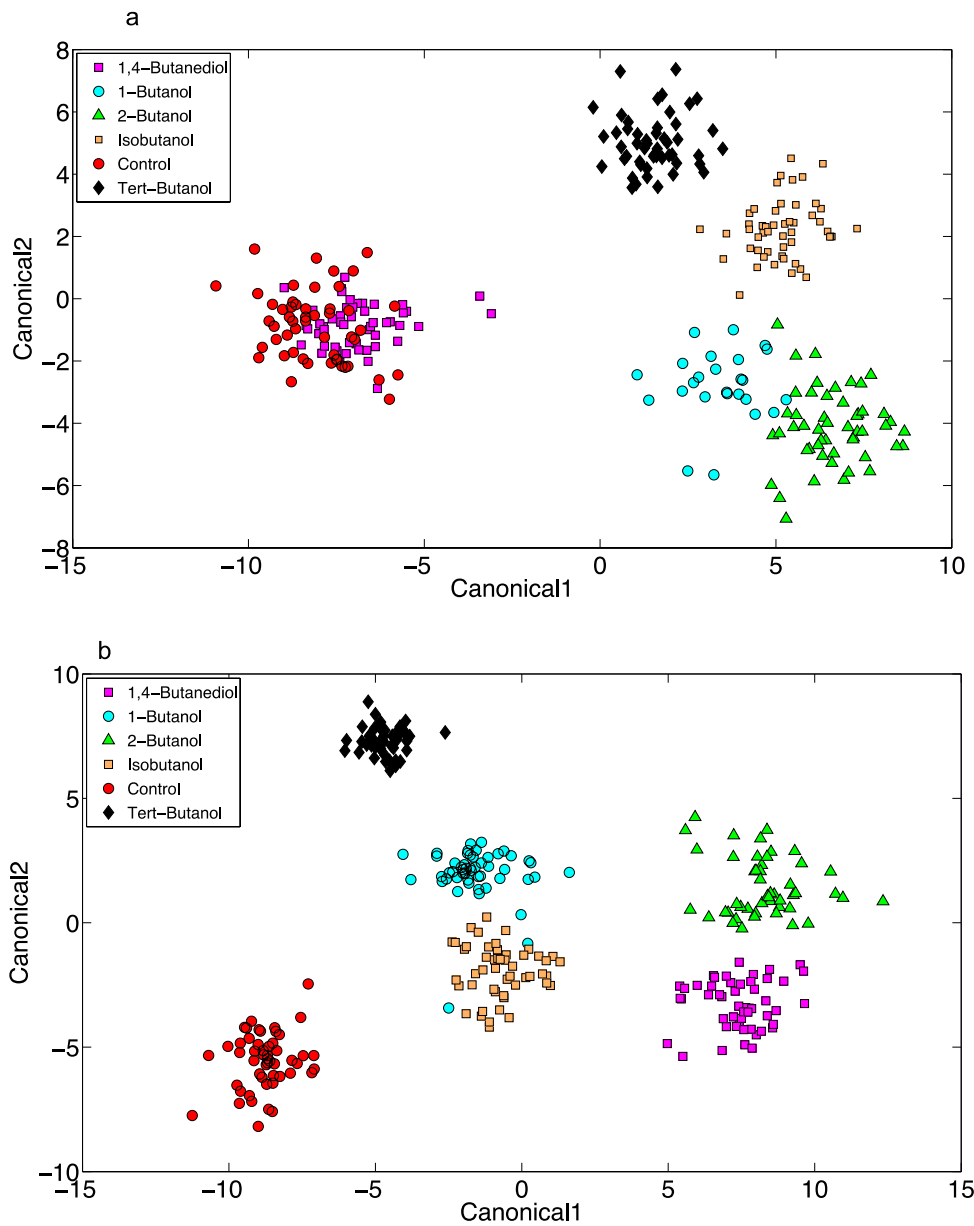


**Figure 5.** DA results by alcohol at (a) 60 min and (b) 180 min

## DISCUSSION

### *Monitoring phenotypic changes in near real-time*

The methods presented here provide a way of monitoring phenotypic changes of microbes in near real-time using Raman spectroscopy. In our previous publication (1), the effect of 1-

butanol toxicity on the *E. coli* cells was studied by extracting the intensity of specific bands from Raman spectra and correlating these with phenotypic traits such as: (i) membrane fatty acids composition, (ii) cell membrane fluidity, and (iii) amino acids composition. Here, a different approach was taken, as multivariate statistical analyses were used to make use of an entire Raman spectrum in an approach termed “chemometric fingerprinting.” A Raman spectrum includes contributions from all chemicals comprising a sample. When performed on a cell, the Raman spectrum is complex (Fig. 2) and can contain contributions from thousands of molecules. Thus, an entire Raman spectrum actually contains very detailed information about the cell-wide phenotype, and the Raman spectroscopy based methodology presented here uses this information to compare and distinguish among microbial phenotypes. In the application presented in this paper, the phenotypic responses resulting from treatment of *E. coli* with different 4-carbon alcohols was studied. The alcohols differed in location of the alcohol group and alkyl chain length. These resulted in significantly different toxicity levels (Fig. 1), which was expected based on previously published results with 1-butanol toxicity study (Zu, et al, 2014). However, the observed cell responses among the treated cultures were found to be different and dynamic.

### ***Effects of terminal alkyl chain length***

The results of this study confirm that 4-carbon alcohols with longer terminal alkyl chains have greater toxicity (primary alcohols > secondary alcohols > tertiary alcohols) to *E. coli* cells when applied at 1.2% (v/v). 1,4-Butanediol does not have a terminal alkyl chain, since both ends are capped with alcohol groups. Thus, it was expected that the hydrophilic *E. coli* cell membrane head groups would interact with this alcohol, but prevent penetration of the membrane into the hydrophobic center. Also, interactions with polar parts of membrane proteins sticking out could potentially impact on the effect of these proteins. These results were confirmed as minimal toxicity

was observed (Fig. 1), and the results of DA (over all time points) revealed clustering between the control and 1,4-butanediol-treated (Fig. 3). This indicates that there was relatively no phenotype change with the addition of 1,4-butanediol. However, if phenotype changes are studied at 180 min only, clear separation is observed between the control and 1,4-butanediol treated cells. Thus, it can be concluded that cell phenotypes do in fact respond to 1,4-butanediol, but this happens very late (around 180 min) resulting in minimal toxicity. Overall, 1-butanol and 2-butanol produce similar phenotypes (Figs. 3 and 5a), but 1-butanol is more toxic (Fig. 1). However, at 180 min (Fig. 5b), the 2-butanol treated phenotypes showed more similarity to the 1,4-butanediol phenotypes, suggesting multiple possible responses over time. Finally, isobutanol and tert-butanol clustered together in Fig. 3, suggesting similarities in phenotypic responses over time. This is interesting because isobutanol proved to be much more toxic than tert-butanol (Fig. 1). With similar phenotypes, the dramatic change in toxicity levels can be attributed to the molecular structures of the alcohols themselves, which both contain branched alkyl groups. However, the length of the terminal alkyl chain from the terminal alcohol is 3 carbons for isobutanol and only 2 carbons for tert-butanol. This suggests that the branched alkyl group played a role in the phenotypic response to the 4-carbon alcohols, but even an increase in the terminal alkyl chain length by 1 carbon can determine whether this phenotypic response thrives or fails when faced with potential toxicity. Clearly more research is needed to determine how microbes sense their environment and induce phenotypic changes. But it does appear that several phenotype response programs are in place with different levels of actions based on molecular factors such as the alkyl chain length and branching patterns.

### ***Potential uses***

The chemometric fingerprinting approach developed here to study dynamic phenotypic responses in near real-time has very broad applicability. One of the drawbacks of Raman-based analyses of complex biological systems (i.e., a cell) is the ambiguity that can exist with Raman band assignments. The approach presented here eliminates that, as entire Raman spectra (not individual bands) are used in the analysis. While this may not have applicability to extract specific chemical information (e.g., fatty acids, amino acids, etc.), the approach can be used to compare among phenotypes and study the dynamics of phenotypic responses. Thus, this approach can be applied to all microbes and treatments and has additional applicability to eukaryotes and biomedical research. Observed responses from this study with different 4-carbon alcohols could prove very useful for engineering of alcohol tolerance in bacteria. By studying the observed clustering patterns, one can discern cell response mechanisms that are attributed to improved tolerance.

## REFERENCES

1. **Zu TNK, Athamneh AIM, Wallace RS, Collakova E, Senger RS.** 2014. Near real-time analysis of the phenotypic responses of *Escherichia coli* to 1-butanol exposure using Raman spectroscopy. Accepted to J Bacteriol.
2. **Pramanik J, Keasling JD.** 1998. Effect of *Escherichia coli* biomass composition on central metabolic fluxes predicted by a stoichiometric model. *Biotechnology and bioengineering* **60**:230-238.
3. **Senger RS, Papoutsakis ET.** 2008. Genome-scale model for *Clostridium acetobutylicum*: Part II. Development of specific proton flux states and numerically determined subsystems. *Biotechnology and bioengineering* **101**:1053-1071.
4. **Senger RS.** 2010. Biofuel production improvement with genome-scale models: The role of cell composition. *Biotechnology journal* **5**:671-685.
5. **Kirschner C, Maquelin K, Pina P, Thi NN, Choo-Smith L-P, Sockalingum G, Sandt C, Ami D, Orsini F, Doglia S.** 2001. Classification and identification of enterococci: a comparative phenotypic, genotypic, and vibrational spectroscopic study. *J Clin Microbiol* **39**:1763-1770.
6. **Chan JW, Lieu DK, Huser T, Li RA.** 2009. Label-free separation of human embryonic stem cells and their cardiac derivatives using Raman spectroscopy. *Anal Chem* **81**:1324-1331.
7. **Krishna CM, Kegelaer G, Adt I, Rubin S, Kartha VB, Manfait M, Sockalingum GD.** 2006. Combined Fourier transform infrared and Raman spectroscopic approach for identification of multidrug resistance phenotype in cancer cell lines. *Biopolymers* **82**:462-470.

8. **Athamneh AI, Alajlouni RA, Wallace RS, Seleem MN, Senger RS.** 2014. Phenotypic profiling of antibiotic response signatures in *Escherichia coli* using Raman spectroscopy. *Antimicrobial agents and chemotherapy* **58**:1302-1314.
9. **Chan JW, Winhold H, Corzett MH, Ulloa JM, Cosman M, Balhorn R, Huser T.** 2007. Monitoring dynamic protein expression in living *E. coli*. Bacterial cells by laser tweezers Raman spectroscopy. *Cytometry. Part A : the journal of the International Society for Analytical Cytology* **71**:468-474.
10. **Wu CY, Huang CC, Jhang JS, Liu AC, Chiang CC, Hsieh ML, Huang PJ, Tuyen le D, Minh le Q, Yang TS, Chau LK, Kan HC, Hsu CC.** 2009. Hybrid surface-enhanced Raman scattering substrate from gold nanoparticle and photonic crystal: maneuverability and uniformity of Raman spectra. *Optics express* **17**:21522-21529.
11. **Wu H, Volponi JV, Oliver AE, Parikh AN, Simmons BA, Singh S.** 2011. *In vivo* lipidomics using single-cell Raman spectroscopy. *Proceedings of the National Academy of Sciences*.
12. **Notingher I.** 2007. Raman spectroscopy cell-based biosensors. *Sensors* **7**:1343-1358.
13. **Li H, Hanson C, Fuchs JA, Woodward C, Thomas Jr GJ.** 1993. Determination of the pKa values of active-center cysteines, cysteines-32 and-35, in *Escherichia coli* thioredoxin by Raman spectroscopy. *Biochemistry* **32**:5800-5808.
14. **Bocklitz T, Walter A, Hartmann K, Rösch P, Popp J.** 2011. How to pre-process Raman spectra for reliable and stable models? *Anal Chim Acta* **704**:47-56.
15. **De Gelder J, De Gussem K, Vandenabeele P, Moens L.** 2007. Reference database of Raman spectra of biological molecules. *Journal of Raman Spectroscopy* **38**:1133-1147.

16. **Gao C, Jin YZ, Kong H, Whitby RL, Acquah SF, Chen G, Qian H, Hartschuh A, Silva S, Henley S.** 2005. Polyurea-functionalized multiwalled carbon nanotubes: synthesis, morphology, and Raman spectroscopy. *The Journal of Physical Chemistry B* **109**:11925-11932.
17. **Movasaghi Z, Rehman S, Rehman IU.** 2007. Raman spectroscopy of biological tissues. *Applied Spectroscopy Reviews* **42**:493-541.
18. **Stephanopoulos G.** 2007. Challenges in engineering microbes for biofuels production. *Science* **315**:801-804.
19. **Qureshi N, Ezeji TC.** 2008. Butanol, 'a superior biofuel' production from agricultural residues (renewable biomass): recent progress in technology. *Biofuels, Bioproducts and Biorefining* **2**:319-330.
20. **Dunlop MJ, Dossani ZY, Szmids HL, Chu HC, Lee TS, Keasling JD, Hadi MZ, Mukhopadhyay A.** 2011. Engineering microbial biofuel tolerance and export using efflux pumps. *Molecular systems biology* **7**.
21. **Brynildsen MP, Liao JC.** 2009. An integrated network approach identifies the isobutanol response network of *Escherichia coli*. *Molecular Systems Biology* **5**:277.
22. **Ingram LO.** 1976. Adaptation of membrane lipids to alcohols. *Journal of bacteriology* **125**:670-678.
23. **Rutherford BJ, Dahl RH, Price RE, Szmids HL, Benke PI, Mukhopadhyay A, Keasling JD.** 2010. Functional genomic study of exogenous n-butanol stress in *Escherichia coli*. *Applied and environmental microbiology* **76**:1935-1945.

24. **Ramos JL, Duque E, Gallegos MT, Godoy P, Ramos-Gonzalez MI, Rojas A, Teran W, Segura A.** 2002. Mechanisms of solvent tolerance in gram-negative bacteria. Annual review of microbiology **56**:743-768.
25. **Reyes LH, Almario MP, Kao KC.** 2011. Genomic library screens for genes involved in n-butanol tolerance in *Escherichia coli*. PLoS One **6**:e17678.
26. **Minty JJ, Lesnefsky AA, Lin F, Chen Y, Zaroff TA, Veloso AB, Xie B, McConnell CA, Ward RJ, Schwartz DR, Rouillard JM, Gao Y, Gulari E, Lin XN.** 2011. Evolution combined with genomic study elucidates genetic bases of isobutanol tolerance in *Escherichia coli*. Microbial cell factories **10**:18.
27. **Dunlop MJ, Keasling JD, Mukhopadhyay A.** 2010. A model for improving microbial biofuel production using a synthetic feedback loop. Systems and synthetic biology **4**:95-104.
28. **Milne CB, Eddy JA, Raju R, Ardekani S, Kim PJ, Senger RS, Jin YS, Blaschek HP, Price ND.** 2011. Metabolic network reconstruction and genome-scale model of butanol-producing strain *Clostridium beijerinckii* NCIMB 8052. BMC systems biology **5**:130.
29. **Senger RS, Papoutsakis ET.** 2008. Genome-scale model for *Clostridium acetobutylicum*: Part I. Metabolic network resolution and analysis. Biotechnology and bioengineering **101**:1036-1052.
30. **Atsumi S, Hanai T, Liao JC.** 2008. Non-fermentative pathways for synthesis of branched-chain higher alcohols as biofuels. Nature **451**:86-89.
31. **Yim H, Haselbeck R, Niu W, Pujol-Baxley C, Burgard A, Boldt J, Khandurina J, Trawick JD, Osterhout RE, Stephen R, Estadilla J, Teisan S, Schreyer HB, Andrae**

**S, Yang TH, Lee SY, Burk MJ, Van Dien S.** 2011. Metabolic engineering of *Escherichia coli* for direct production of 1,4-butanediol. *Nature chemical biology* **7**:445-452.

## CHAPTER FIVE

# **Peptide-guided silver nanoparticles for spatio-temporal surface-enhanced Raman spectroscopy (SERS) analysis of target cellular locations in the *E. coli* bacterium**

(Manuscript to be submitted to a peer-reviewed Journal by December 2014)

Theresah N.K. Zu, Benjamin G. Freedman, Imen Tanniche, Ahmad I.M. Athamneh, Ryan S. Senger<sup>#</sup>

# Corresponding author address

301C HABB1

Department of Biological Systems Engineering

Virginia Tech

Phone: 540-231-9501

Email: senger@vt.edu

Running Title: pgSERS analysis of *E. coli*

# Peptide-guided surface-enhanced Raman scattering (pgSERS) for localized subcellular analysis of *E. coli*

## ABSTRACT

The technology of peptide-guided surface enhanced Raman scattering (pgSERS) was further explored in this research. In particular, pgSERS probes consist of peptides bound covalently to silver nanoparticles (Ag-NPs) that then localize in specified subcellular locations of microbes. pgSERS probes were assembled *ex vivo* that effectively targeted the cell interior of *E. coli* and produced localized cell chemical composition information when analyzed by Raman spectroscopy. In addition, a novel technique of *in vivo* pgSERS probe assembly was demonstrated, in which a target protein of interest was overexpressed and fused with a silver binding-domain (AgBP<sub>2</sub>). Three different proteins with different known subcellular localizations were expressed with a bound AgBP<sub>2</sub> domain: (i) FadL (an outer membrane protein), (ii) MalE (a periplasm bound protein) and (iii) AroP (a cytoplasm bound protein). When the cell was flooded with unbound Ag-NPs, the particles were drawn to the AgBP<sub>2</sub> domain, creating SERS “hot spots” in specific locations. Analysis by Raman spectroscopy revealed location-specific chemical composition information, and these were used to study 1-butanol toxicity to *E. coli*.

## INTRODUCTION

### *Advances in microbial phenotyping using Raman spectroscopy*

The chemical composition of a cell is very complex and analysis is usually performed with several off-line analytical techniques (1). A recent approach showed that Raman spectroscopy analysis of 1-butanol treated and untreated *E. coli* cultures closely mirrored results obtained by extractions and chromatographic analyses (2). Raman spectroscopy has been shown to be a good candidate for microbial phenotyping and has been applied to samples of different phases (i.e., solid, liquid, and gas) (3-6), as well as cells, tissues, and organs (7, 8). The major advantages of using Raman spectroscopy for analyses biological systems include: (i) near real-time analyses, (ii) non-destructiveness to the sample, (iii) lack of interference from water, and (iv) minimal sample preparation. We introduce a novel technology that allows obtaining a Raman signal of specific subcellular locations in an *E. coli* cell. While similar achievements have been made in eukaryotes (9), bacterial cells have proven difficult because of their relative size. The technology developed here has a broad applicability to all organisms and is based on our previously developed technology of peptide-guided surface-enhanced Raman scattering (pgSERS) probes (10).

### *Surface-enhanced Raman scattering (SERS)*

Raman spectroscopy produces low signal intensities, which can present challenges to the analysis of cells and other biological samples. Because of this, surface-enhanced Raman scattering (SERS) has gained popularity for the analysis of cellular components (11, 12). SERS has been shown to enhance Raman signal intensities by orders of magnitude ( $10^4 - 10^{16}$ ) (13), making the technique sensitive down to the single molecule level (13-15). SERS requires the presence of metal nanoparticles (usually silver or gold), and the Raman signals from molecules in the proximity of these nanoparticles undergo the amplification (13). Enhancement of the Raman signal, however,

is non-specific, posing a challenge for analysis in cells, where the intracellular structure and chemical composition are highly complex and heterogeneous (2). This associated complexity makes it difficult to interpret SERS signals from cells, as SERS signals are highly irreproducible when metal nanoparticles are flooded into a cell uniformly to generate SERS signals (15, 16). The irreproducibility and non-specificity of SERS for cell analysis result in random dispersion of the SERS probes inside the cell, resulting in convoluted signals arising from contributions from potentially all molecules of the intracellular environment (17). As such, there is the need for reproducibility of the SERS signal. This is achieved by targeting nanoparticles to a specific intracellular location.

Multiple approaches to localize nanoparticles for SERS analysis of subcellular locations have been published (4, 14, 17). Most are largely limited to analysis of a single intracellular environment and only one has been tailored for microbial phenotyping as it involves synthetic peptides bound covalently to silver nanoparticles (Ag-NPs). The initial application of this technology was to target the outer membrane of *E. coli* and show significant differences in SERS signals between (i) randomly dispersed Ag-NPs and (ii) localized pgSERS probes (10). Though very useful, this approach requires relatively expensive custom synthesized peptides, *ex vivo* assembly of peptides and Ag-NPs, and that the pgSERS probes can penetrate cell membranes. To assess a general usefulness of this approach, three different *ex vivo* assembled pgSERS probes were analyzed. We also introduce a new approach of *in vivo* assembly of pgSERS probes.

### ***In vivo assembly of pgSERS probes***

Methods regarding the *ex vivo* pgSERS assembly process and analysis are available (10). The *in vivo* assembly process involves (i) genetically combining a silver-binding domain with a protein of interest, (ii) expressing this chimeric protein in an organism of interest, and (iii)

introducing unlabeled Ag-NPs to the cell. The Ag-NPs then localize to the specific silver binding domain of the protein, giving rise to a localized SERS signal. Three proteins were chosen based on their known final intracellular localization in *E. coli* following production (i) FadL (outer membrane), (ii) MalE (periplasm), and (iii) AroP (cytoplasm).

***FadL: An outer membrane protein***

Several Gram-negative bacteria can use long-chain fatty acids (LCFAs) as a carbon and energy source (18, 19); however, the outer membrane of a bacterium is generally impermeable to hydrophobic LCFAs compounds (20, 21). In order to traverse the outer membrane, LCFAs depend on membrane bound accessory proteins. The fatty acid degradation enzyme FadL (22) is a member of a conserved family of outer membrane proteins involved in the transport of LCFAs (23). FadL has an additional function as a receptor for the bacteriophage T2 and is likely associated with peptidoglycan (24). FadL of *E. coli* consists of 448 amino acids (molecular weight of 48.8 KDa) (25). It has been crystallized (26, 27), and its 3-D structure contains a beta-barrel for LCFA transport. The N-terminus extends through the barrel structure and occupies a position on the extracellular side of the membrane (Fig. 1) (28). These characteristics, along with the localization of FadL in the outer membrane, guided the protein design to linking the silver binding domain to FadL N-terminus in order to target Ag-NPs on the *E. coli* cell surface.

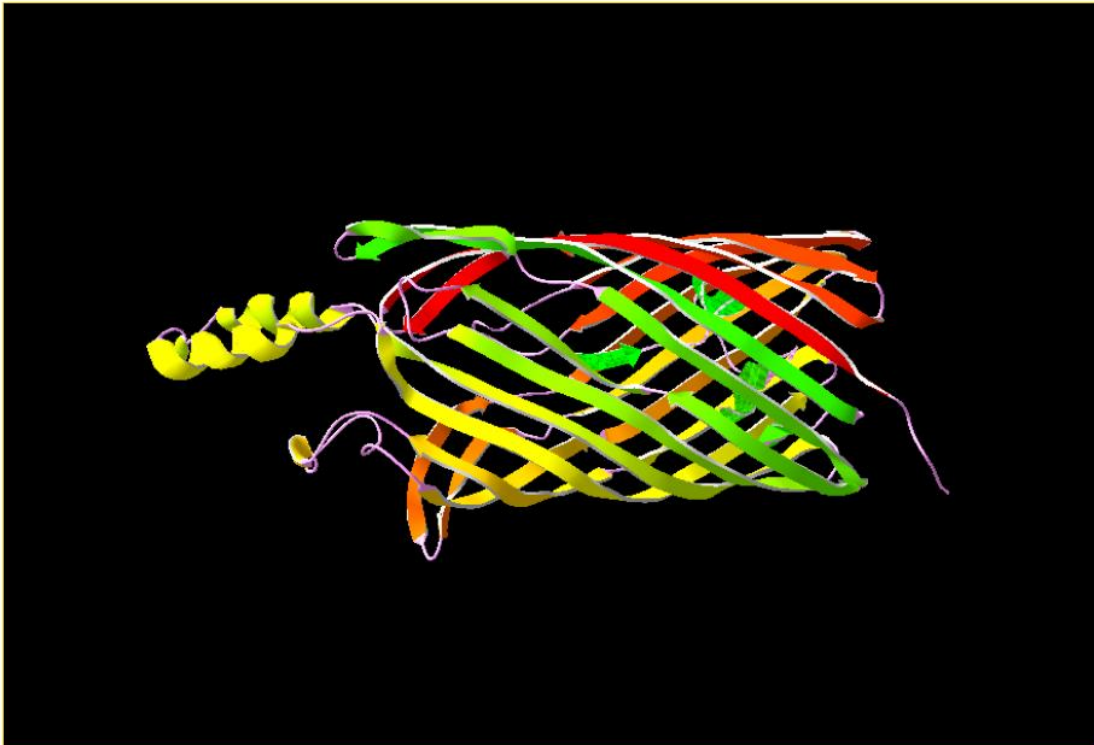


**Figure 1.** The protein 3D structure for FadL (1T6 in the protein database (PDB)) (26)

***MalE: A periplasm localized protein***

The maltose binding protein (MalE) is a soluble protein located in the periplasm of Gram-negative bacteria and is involved in the active transport of maltose and maltodextrins across the cytoplasmic membrane of *E. coli* and promotes chemotaxis (29). The mature MalE folds into a highly stable, protease-resistant, tertiary structure (Fig. 2) (30). MalE is a monomeric protein with a molecular mass of 40.6 kDa (31). The structure consists of two globular domains that are separated by a deep groove or cleft. The maltose binding site is situated within the central cleft between the two domains (32, 33).

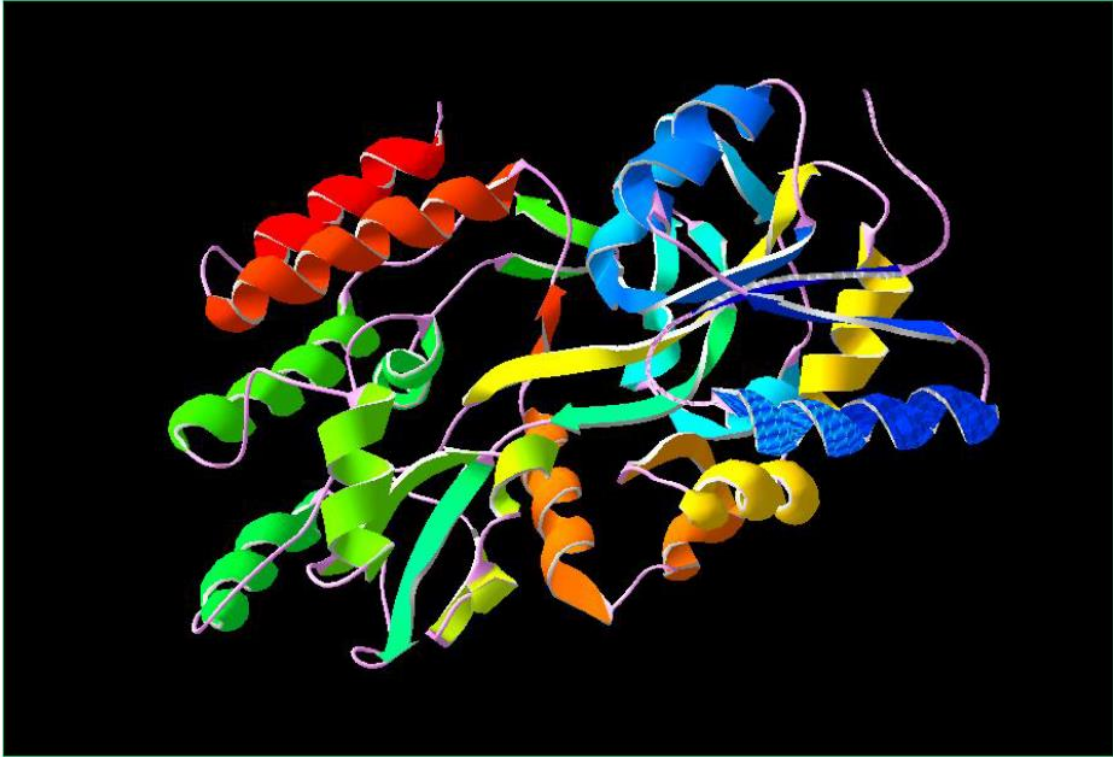


**Figure 2.** The protein 3D structure for MaleE (1FQA in the PDB) model from protein database (32).

***AroP: A cytoplasm localized protein***

The three aromatic amino acids phenylalanine, tryptophan, and tyrosine can be actively transported across the inner membrane of *E. coli* by a number of specific and distinct transport systems. They can also pass through the cytoplasmic membrane via the general aromatic transporter, AroP (34, 35). It is an integral cytoplasmic 37 kDa membrane protein that targets intracellular contents close to the inner membrane on the cytoplasmic side (32). AroP consists of two equivalent domains arranged in 12 membrane-spanning regions of approximately 21 amino acids connected by hydrophilic loops of various lengths (Fig. 3) (36-38).



**Figure 3.** The protein 3D structural prediction for AroP (P15993 in the Protein Model Portal (39)).

***AgBP<sub>2</sub>: Silver binding domain***

The increased use of Ag-NPs in multiple applications has raised concerns about the lasting environmental impacts and potential toxicity to microbes (40). Bacterial tolerance to Ag-NPs has been investigated by altering the protein binding and transport domains that adhere to these particles. A library search approach identified the short peptide AgBP<sub>2</sub> (EQLGVRKELRGV) exhibiting significant binding to silver (40). When fused to the maltose binding protein the silver binding domain increased cell survival by a factor of 1000 upon incubation in silver doped media; however, the mechanism of tolerance was not fully elucidated in the published study (40).

### ***pgSERS for subcellular targeting of E. coli***

The *ex vivo* and *in vivo* pgSERS assemblies were investigated for site specific targeting and analysis within the *E. coli* bacterium. The *ex vivo* assembly method followed an established protocol (10), and demonstrated the ability to target the interior of the *E. coli* cell. The *in vivo* assembly method is shown here for the first time and three specific locations of the *E. coli* cell were targeted using FadL, MBP, and AroP proteins expressed with a fused AgBP<sub>2</sub> domain. Ag-NPs were found to effectively bind these proteins and create SERS “hot spots” of aggregated Ag-NPs at specified intracellular locations. Aggregating Ag-NPs are characteristic of pgSERS probes, and these were visualized by transmission electron microscopy (TEM) to verify localization of Ag-NPs.

Our *in vivo* pgSERS assembly approach is novel and allows for continuous and controlled production of individual proteins, allowing for chemical composition analysis of outer membrane, periplasmic, or cytoplasmic locations of the *E. coli*. This technique has a broad applicability to virtually any organism, and the protein sequence can be modified as necessary.

## **MATERIALS AND METHODS**

### ***Bacterial strain, media, and growth conditions***

Proteins were expressed in *E. coli* ER2566 (New England Biolabs (NEB); Ipswich, MA). Cultures were grown at 37°C in liquid Luria-Bertani (LB) media with 100 mg/L ampicillin and agitation at 210 rpm. Overnight cell cultures were prepared by inoculating four 15 mL tubes of liquid LB growth media with *E. coli* cells from a solid agar plate containing: (i) an empty pBAD24 plasmid, (ii) cells with the *fadL* gene inserted on the pBAD24 plasmid (*E. coli* pBAD-*fadL*), (iii) cells with *malE* inserted on a pBAD24 plasmid (*E. coli* pBAD-*malE*), and (iv) cells with *aroP*

inserted on a pBAD24 plasmid (*E. coli* pBAD-*aroP*). Cultures were incubated and monitored by optical density measurements at 600 nm (OD<sub>600</sub>). Aliquot samples were then used to prepare subcultures by diluting 10 mL of cell culture with 15 mL fresh pre-warmed LB media in a sterilized culture flask and grown to the start of the exponential phase (OD<sub>600</sub>: 0.4 – 0.6), at which point the first sample (2 mL) from control culture was taken to serve as the positive control and stored in a microcentrifuge tube. The sub-cultures were then induced with 0.1 M L-arabinose solution for at least 3 hours. At the end of the induction time, samples were taken for: (i) SDS-page protein gel analysis (50 µL), (ii) *in vivo* assembly with Ag-NPs and TEM imaging (1 mL), and (iii) analysis by Raman spectroscopy (10 µL).

### ***PCR and cloning***

Genomic DNA extraction, plasmid DNA purification, and PCR product purification were performed using the Generation<sup>TM</sup> capture column (Qiagen, Valencia, CA), GenJet Plasmid Miniprep Kit (Fisher Scientific, Pittsburgh PA), and GenJet PCR Purification Kit (Fisher Scientific, Pittsburgh PA), respectively. All enzymes were purchased from NEB. *E. coli* K12 10B genomic DNA was used as a template for PCR amplification of *FadL*, *MalE*, and *AroP*. Each gene was amplified using the primer sets listed in Table 1, which also contained the AgBP<sub>2</sub> silver binding domain and *EcoR* I and *Hind* III restriction sites for cloning.

**Table 1.** PCR primers used to amplify the *fadL*, *malE*, and *aroP* genes for over-expression.

<b>Primer Name</b>	<b>Sequence (5'→3')</b>
<i>fadL</i> (forward)	TAG <b>GAATTC</b> CATGAGCCAGAAAACCCTGTTTACAA
<i>fadL</i> (reverse)	TAG <u><b>AAGCTT</b></u> TTAAACACCACGCAGTTCTTTACGAACACCCAGCT GTT <b>C</b> GAACGCGTAGTTAAAGTTAGTACCG
<i>malE</i> (forward)	TAG <b>GAATTC</b> CATGAAAATAAAAAACAGGTGCACGCATC
<i>malE</i> (reverse)	TTCA <u><b>AAGCTT</b></u> TTAAACACCACGCAGTTCTTTACGAACACCCAGCTG TTCCTTGGTGATACGAGTCTGCGCG
<i>aroP</i> (forward)	TAG <b>GAATTC</b> CATGATGGAAGGTCAACAGCACGG
<i>aroP</i> (reverse)	TAG <u><b>AAGCTT</b></u> TTAAACACCACGCAGTTCTTTACGAACACCCAGCT GTT <b>C</b> CATGCGCTTTTACGGCTTTGGC
<b>Plasmid check primers</b>	
pBAD24-f	AAATAAACAAATAGGGGTT GCTCATGAGCCCGAAGTG
pBAD24-r	AGGCGCCC AAACAAAAGAGTTTGTAGAAACGC

\*Underline: The AgBP<sub>2</sub> silver binding domain

\*Bold: The *EcoR* I restriction site

\*Bold and Underline: The *Hind* III restriction site

Primers were synthesized by Integrated DNA Technologies (IDT; Coralville, IA). PCR was performed with Q5 High-Fidelity PCR Polymerase (NEB) according to the manufacturer's instruction. PCR products were digested with *EcoR* I and *Hind* III and combined with a similarly digested and dephosphorylated pBAD24 plasmid (41). All ligation reactions were performed using the Quick Ligation<sup>TM</sup> Sticky-End Master Mix (NEB) using reaction conditions specified by the manufacturer. Each of the plasmids was transformed into *E. coli* ER2566 chemically competent cells (NEB). Transformants were selected on LB agar plates with 100 µg/ml ampicillin. Colony PCR was used to verify cloning and was performed using the plasmid check primers in Table 1 and the Quick-Load Taq 2X Master Mix (NEB) following to the manufacturer's protocol. Resulting PCR products were visualized by gel electrophoresis.

### ***Protein induction***

The recovered protein samples, were separated and analyzed on 12% polyacrylamide gels.

### ***Ex vivo pgSERS probe assembly***

Existing methods for *ex vivo* pgSERS probe assembly were used (10). The following custom peptides were synthesized (Peptide 2.0; Chantilly, VA) and covalently bound to SFNPs: (i) CGRKKRRQRRR and (ii) CEEEEEEEEEE. With the N-terminal Cys, the covalent attachment to Ag-NPs is spontaneous and occurs by incubating 40 nm Ag-NPs (0.02 mg/mL) with the synthetic peptide (1 mg/mL) in a 5:1 ratio at room temperature for 2 h. The pgSERS probes were then added to exponentially growing *E. coli* cells (OD<sub>600</sub>: 0.4 – 0.6).

### ***In vivo pgSERS probe assembly***

Cells were harvested from 1 mL of culture by centrifugation at 10,000 rpm and 4°C for 5 min. Cells were washed 3 times with equal-volumes (1 mL) of phosphate-buffered saline (PBS), and the supernatant was discarded after each wash. The washed cells were re-suspended in 100 µL purified water and diluted with 1,000 µL of 40 nm Ag-NPs (0.02 mg/mL) and incubated at room temperature for 2 h.

### ***TEM imaging***

Following the incubation, the cells were recovered by centrifugation at 10,000 rpm and 4°C for 5 min while discarding excess unbound SNP. The resulting cells with bound SNP were then resuspended in 50 µL purified water and fixed in 500 µL of Karnovsky fixative as per recommendation of the imaging lab. The prepared slides with samples, were then visualized and analyzed on a JOEL 1400 transmission-electron microscopy located in the Morphology Service Laboratory at the Virginia-Maryland Regional College of Veterinary Medicine, Blacksburg, VA.

### ***pgSERS analysis and data processing***

Cells incubated with Ag-NPs were brought up in 10  $\mu\text{L}$  Type I purified water and 2  $\mu\text{L}$  was dried on an aluminum surface at room temperature. The dried cells were analyzed with a Bruker Senterra dispersive Raman spectrometer equipped with a confocal microscope and objective lens of 100X magnification (Bruker Optics, Billerica, MA) as described previously (10). Measurements were carried out using 532 nm laser excitation (10 mW) for 5 seconds with spectral resolution of 9-15  $\text{cm}^{-1}$ . At least 10 individual spectra were acquired per sample. Following data acquisition, the data were pre-processed (i.e., baseline correction, error detection) using OPUS software (Bruker Optics; Billerica, MA) and further analysis done with MATLAB (R2012A) software (MathWorks; Natick, MA). All spectra were vector normalized over the entire spectral range (300  $\text{cm}^{-1}$  – 3600  $\text{cm}^{-1}$ ) (2, 10, 42).

## **RESULTS**

### ***Ex vivo pgSERS assembly***

The methods regarding assembly of pgSERS probes *ex vivo* (10) were followed to create two additional sets of pgSERS probes capable of aggregating in the *E. coli* cell interior and producing a SERS signal. In particular, the pgSERS probes designed were based on including hydrophilic amino acids in the pgSERS peptide. In the previous study (10), a hydrophobic peptide resulted in aggregation at the cell membrane, and un-bound Ag-NPs distributed evenly throughout the cell. Results of the hydrophilic pgSERS probes are shown in Fig. 4. Of particular significance is that both hydrophilic pgSERS probes aggregated in the cell interior. The averaged normalized Raman spectrum for each of the pgSERS probes is also presented in Fig. 4. The pgSERS spectra

are largely different for the two probes, which is indicative of the heterogeneous intracellular environment.

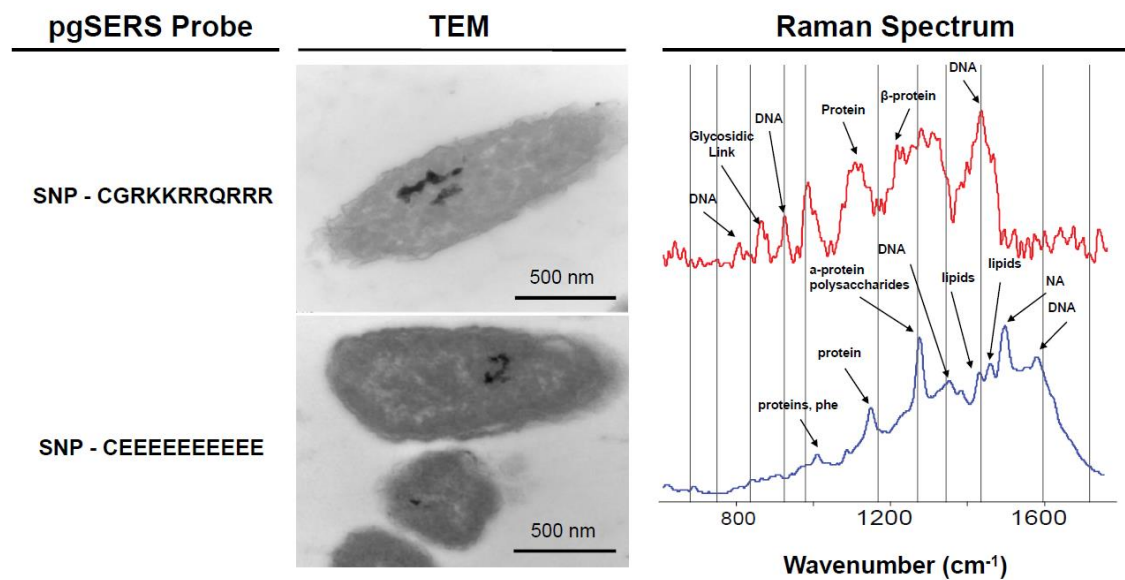


**Figure 4.** *Ex vivo* assembly of pgSERS probes, localization in the *E. coli* interior, and resulting spectra when analyzed by Raman spectroscopy

***In vivo* pgSERS assembly**

The assembly of Ag-NPs with all three peptides fused with the AgBP<sub>2</sub> silver binding domain is conceptualized in Fig. 5.

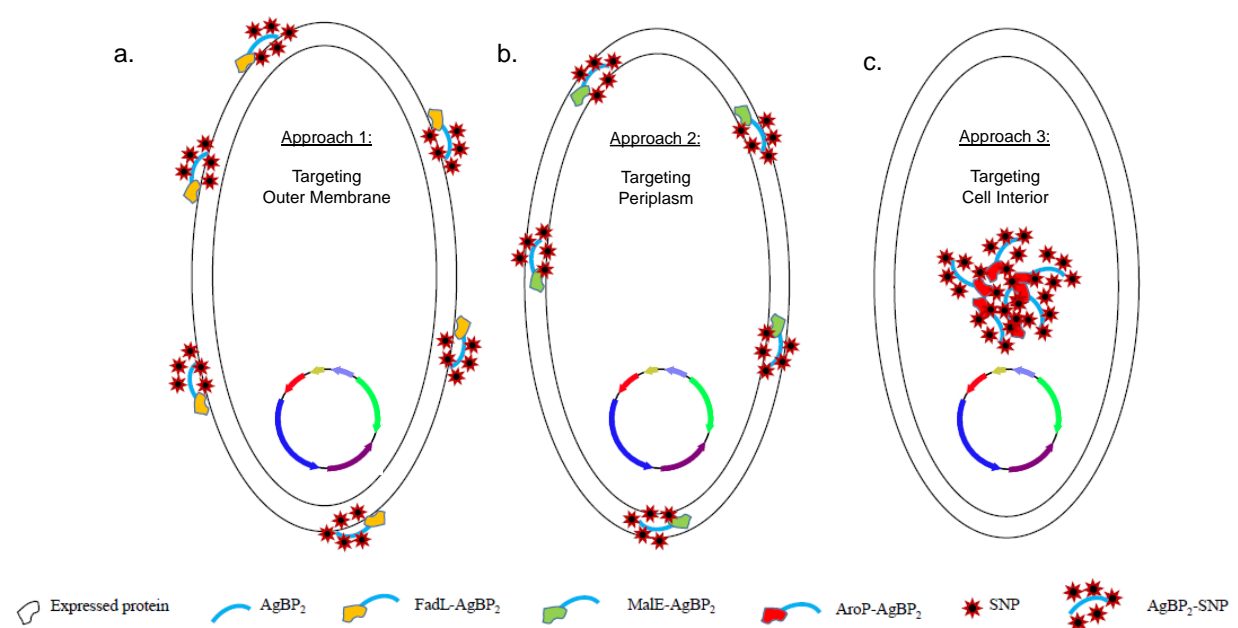


**Figure 5.** Visualization of the hypothesized protein-AgBP<sub>2</sub>-SNP *in vivo* assembly and localization for (a) FadL:AgBP<sub>2</sub>, (b) MalE:AgBP<sub>2</sub>, and (c) AroP:AgBP<sub>2</sub>

Location-specific pgSERS signals were obtained by first cloning the target gene sequence modified to contain the AgBP<sub>2</sub> silver binding domain. Second, by employing an arabinose-inducible promoter in the plasmid construct, expression of the target protein:AgBP<sub>2</sub> fusion could be regulated. When the pBAD promoter was not induced, the targets were not expressed. With pBAD induction using 0.1M arabinose, the targets were expressed, as shown in the SDS-PAGE protein gel image in Fig. 6. A culture in which the pBAD promoter was induced with 0.1M arabinose in the presence of 1.2% 1-butanol showed little to no target protein expression (Fig. 6) and cell debris was largely present in TEM images (not shown).

This is likely the result of a loss in culture viability due to previously observed 1-butanol toxicity (2).

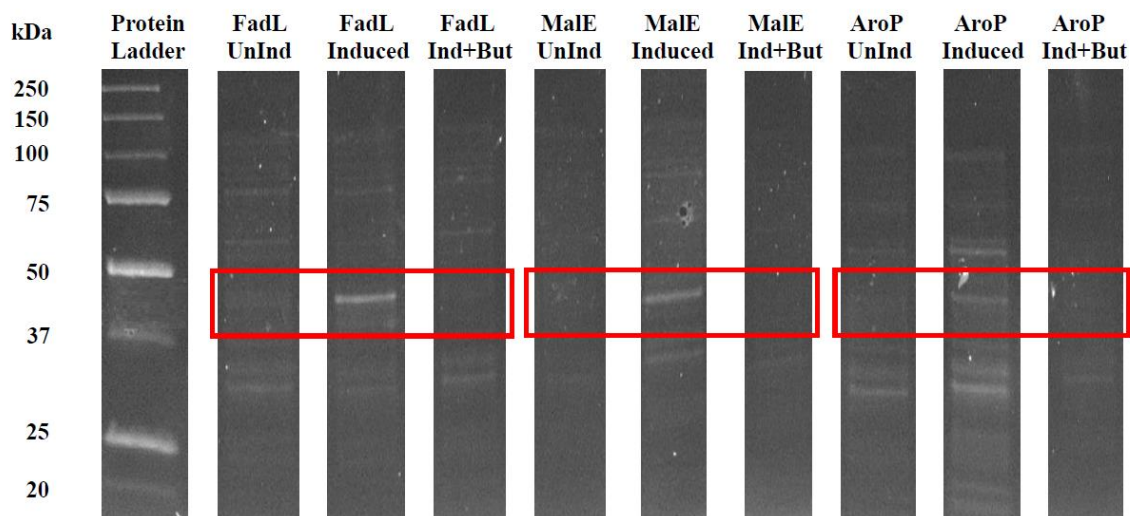


**Figure 6.** SDS-page gel image showing the three proteins; (i) FadL, (ii) MalE, and (iii) AroP before and after induction with arabinose and in the presence of 1-butanol (but).

Following the expression of the target:AgBP<sub>2</sub> fusions (in absence of 1-butanol), 40 nm Ag-NPs were infused into the culture, and *in vivo* assembly and localization of pgSERS probes was observed. TEM images are shown in Fig. 7. In particular, control cultures (no Ag-NPs) are shown in Figs. 7a,b. The higher magnification in Fig. 7b is required to show the absence of Ag-NPs inside the cell. This is compared with Fig. 7c, which shows a single cell with unlabeled and randomly distributed Ag-NPs. Very little order or aggregation of Ag-NPs is observed for this scenario. The *in vivo* assembled pgSERS probes are shown in Fig. 7d-f. Ag-NPs aggregate around the exterior of the cell where FadL:AgBP<sub>2</sub> is expected to be localized, with few Ag-NPs in the interior of the cell (Fig 7d), suggesting that the silver binding domain was successful in binding 40 nm Ag-NPs. Likewise, for the second case, Ag-NPs aggregate on inside of the cell close to the exterior membrane where MalE:AgBP<sub>2</sub> is expected to localize and this is shown in Fig. 7e. Significantly greater silver aggregation was observed for the MalE:AgBP<sub>2</sub> fusion than for the FadL:AgBP<sub>2</sub> fusion. The reasons for this are not entirely clear but could in part be as a result of

the hydrophobic outer membrane bilayer. In addition, the AroP:AgBP<sub>2</sub> fusion bound Ag-NPs and localized in the cell interior near the center of the cell, (Fig. 7f). In this case, even fewer probe aggregates were observed.

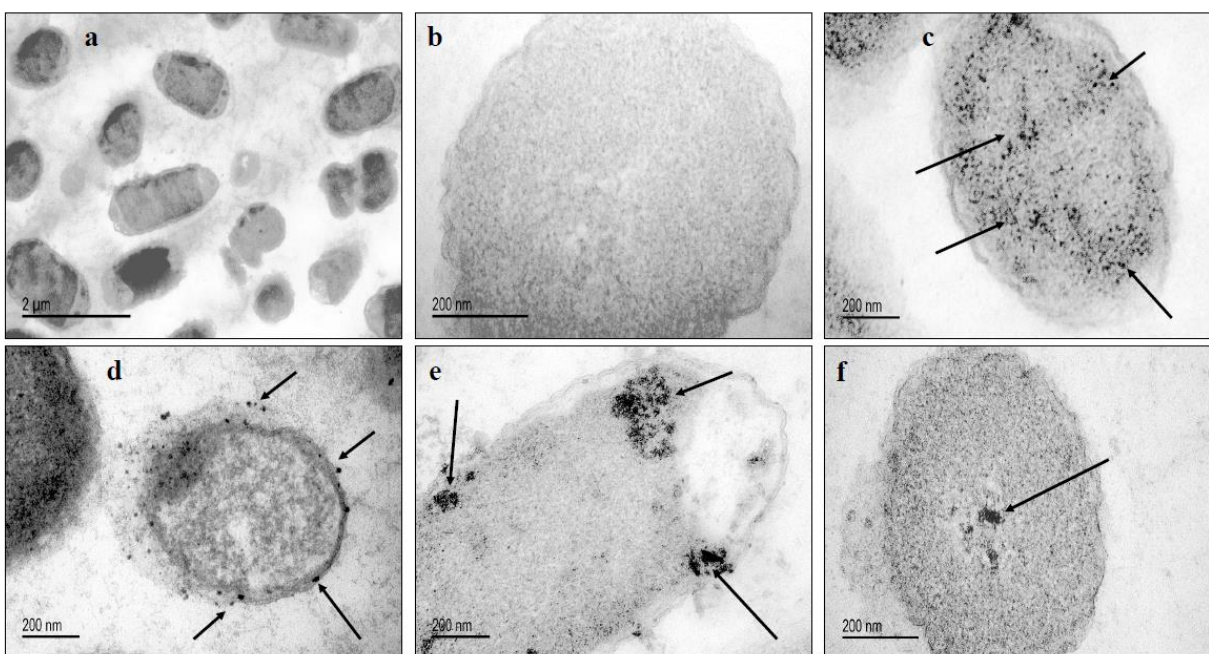


**Figure 7.** Localization of protein:AgBP<sub>2</sub>-SNP conjugates at targeted locations of *E. coli* cells. SNP aggregates are shown as dark spots in b-f TEM images. The following images are shown: (a,b) control sample with no Ag-NPs added, (c) control sample mixed with unlabeled Ag-NPs, (d) induced FadL:AgBP<sub>2</sub> (targeting the outer membrane) mixed with Ag-NPs, (e) induced MalE:AgBP<sub>2</sub> (targeting the periplasm) mixed with Ag-NPs, and (f) induced AroP:AgBP<sub>2</sub> (targeting the cell interior) mixed with Ag-NPs.

### ***Raman spectroscopy of in vivo assembled pgSERS probes***

The representative Raman spectra from cultures harboring the pgSERS probes are shown in Figs. 8-10 for the FadL:AgBP<sub>2</sub>, MalE:AgBP<sub>2</sub>, and AroP:AgBP<sub>2</sub> fusions, respectively. Raman

spectra are shown for both induced and un-induced cultures. Following exposure to 1.2% v/v 1-butanol, the exposed cells were found to undergo a toxicity response that resulted in altered membrane fatty acid structures, increased membrane fluidity, and dramatically reduced cell growth (2). These characteristics were found by both Raman spectroscopy and conventional analytical methods. It was also demonstrated that the total protein content as well as the total amino acids content of hydrolyzed protein for exposed and control cells was unaltered. As shown in Fig. 6, the target fusion proteins were not detected when the cells were exposed to 1.2% v/v 1-butanol. The Raman spectra results for both cases of protein expression in the presence and absence of the alcohol are shown for comparative in Figs. 8-10 for comparison.

The pgSERS acquired signal for the FadL:AgBP<sub>2</sub> fusion protein and control cells show significant differences among the superimposed spectra, as shown in Fig. 8. FadL is an outer membrane protein and the Raman spectrum exhibits characteristics of components of the *E. coli* cell wall such as lipids and  $\alpha$ -protein polysaccharides. The un-induced culture produced multiple signals for DNA, nucleic acids, and proteins, which are absent from the Raman spectra of the induced culture. These Raman peaks are characteristic of Ag-NPs scattered throughout the cell randomly (10). Interestingly, for the 1-butanol exposed cells, the Raman spectrum seems to mimic that of the un-induced culture with several less sharp peaks for nucleic acids, which may be indicative of toxicity.

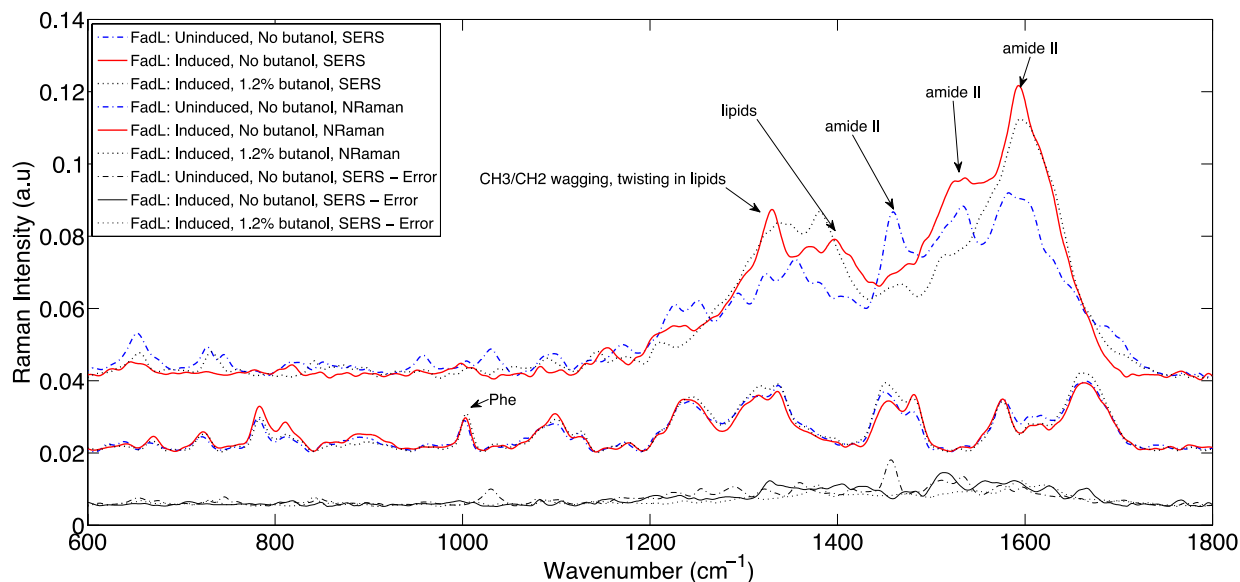


**Figure 8.** Averaged ( $n=10$ ) SERS spectra (top), normal Raman (middle), and standard deviations of SERS signal (bottom) for *E. coli* cells containing the FadL:AgBP<sub>2</sub> fusion. The following SERS spectra are shown: (red) induced, (blue-dashed) un-induced, and (green) induced with 1-butanol exposure. The following normal Raman spectra are shown: (red) induced, (blue-dashed) un-induced, and (green) induced with 1-butanol exposure.

Similarly, when the MalE:AgBP<sub>2</sub> fusion protein was expressed by induction, additional Raman bands were observed in the resulting spectra that are indicative of lipids, proteins, and carbohydrates, as shown in Fig. 9. Again, the major differences between the spectra of induced and un-induced cultures are the presence of lipids, beta-protein structures, and the amide III bands for the induced culture and nucleic acids for the un-induced culture. In addition, the 1-butanol exposed cells produced a Raman signal similar that of the un-induced culture with the notable exception being the strength of the nucleic acids bands.

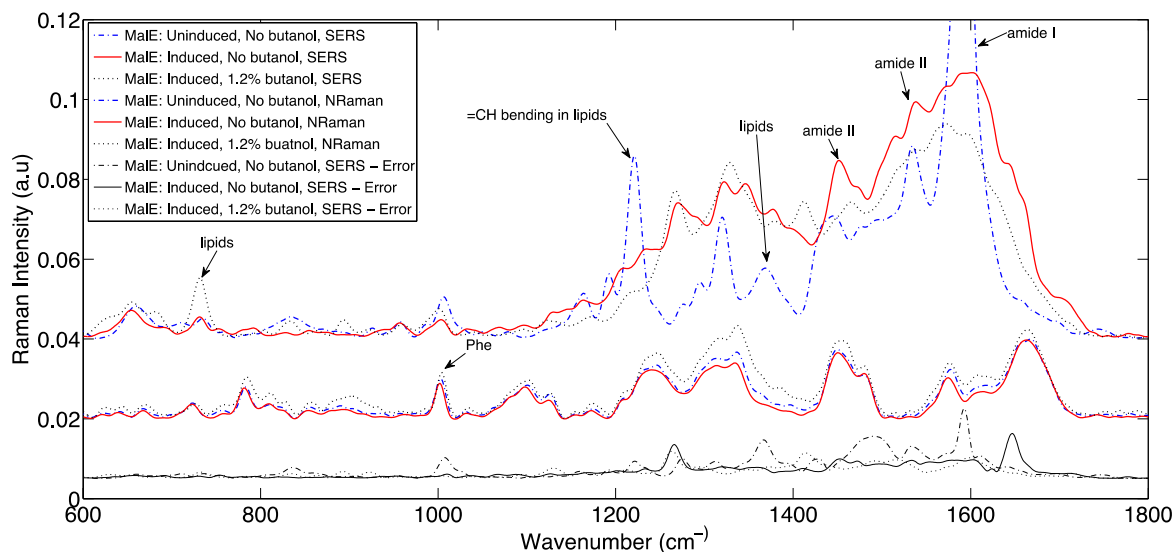


**Figure 9.** Averaged ( $n=10$ ) SERS spectra (top), normal Raman (middle), and standard deviations of SERS signal (bottom) for *E. coli* cells containing the MalE:AgBP<sub>2</sub> fusion. The following SERS spectra are shown: (red) induced, (blue-dashed) uninduced, and (green) induced with 1-butanol exposure. The following normal Raman spectra are shown: (red) induced, (blue-dashed) uninduced, and (green) induced with 1-butanol exposure.

The AroP:AgBP<sub>2</sub> fusion protein, which localized in the cytoplasm, showed strong DNA, RNA, and carbohydrate Raman signals when induced compared to the un-induced culture. This is shown in Fig. 10. These two Raman spectra were found to be similar, as nucleic acids normally dominate the SERS signal generated from randomly distributed Ag-NPs. The 1.2% v/v 1-butanol exposed cells again closely mimicked the un-induced culture with some notable exceptions in peak intensity

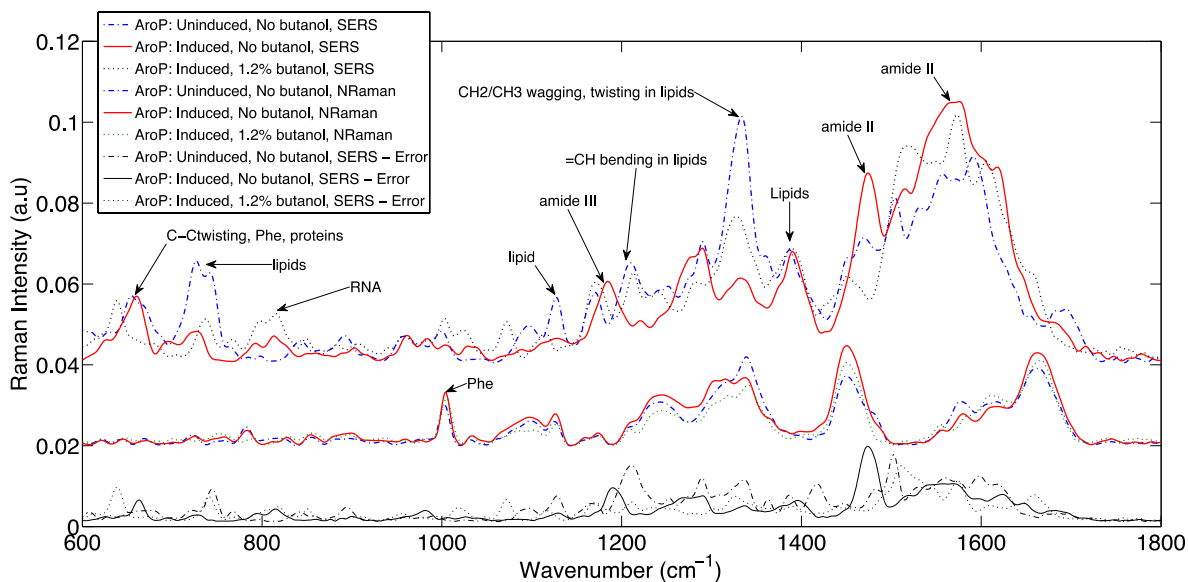


**Figure 10.** Averaged ( $n=10$ ) SERS spectra (top), normal Raman (middle), and standard deviations of SERS signal (bottom) for *E. coli* cells containing the AroP:AgBP<sub>2</sub> fusion. The following SERS spectra are shown: (red) induced, (blue-dashed) uninduced, and (green) induced with 1-butanol exposure. The following normal Raman spectra are shown: (red) induced, (blue-dashed) uninduced, and (green) induced with 1-butanol exposure

## DISCUSSION

### *Use of SERS to acquire microbial phenotype signatures*

In this research, techniques in molecular biology and assembly were combined with SERS technology to target subcellular locations in *E. coli* and obtain chemical composition information. This allowed us to address the challenges of (i) reproducibility of SERS spectra due to randomness of un-labeled SNP dispersion, and (ii) convoluted signal due to the complex nature of cellular composition. The SERS signal is acquired by placing the sample of interest in close proximity to metallic nanoparticles (i.e., usually gold or silver). However, the typical procedure of mixing and

incubating bacteria with SERS substrates, results in random dispersion of substrates within the cell. This leads to the signal amplification of diverse chemical environments simultaneously, resulting in a largely un-reproducible signal. By exploiting the silver binding properties of the AgBP<sub>2</sub> peptide as a fusion tag, Ag-NPs were shown to be drawn to this domain. Thus, localizing Ag-NPs became possible by fusing AgBP<sub>2</sub> with proteins with known localization properties. The prospect of this technology is promising in that very specific cell environments can now be targeted, and the potential applications are multi fold. For example, while this technique was used to probe cell chemical composition broadly, it can also be used to identify specific molecules within a cell. This will have applications in nano-medicine as well as environmental microbiology. We chose the problem of 1-butanol toxicity for pg-SERS analyses since we already have data for the same experiment using Raman spectroscopy analysis..

### ***Analyzing 1-butanol toxicity***

In a separate approach (2), Raman spectroscopy was used together with standardized methods of analysis (e.g., GC-FID/MS, UPLC, fluorescence anisotropy, and Bradford assay) to study the phenotypic responses of *E. coli* cells exposed to 1.2% 1-butanol. Good correlations between different analytical methods were found. An attempt was made to further investigate these original findings by employing the *in vivo* assembled pgSERS methodology. SDS-PAGE protein gels (Figure 6) showed, interestingly, that the targeted protein fusions were not expressed (or at least not visible on the gel) in the presence of 1.2% v/v 1-butanol. This could potentially be as a result of interaction of the alcohol groups with hydrophobic parts of the membrane proteins disrupting their function. This presumably means that Ag-NPs were not aggregated in the targeted locations, yet caused adverse disruptions in the cells seen as cell debris in the TEM images (not shown). Visual inspection of the SERS spectra for all three cases of presumed induction in the

presence of 1.2% 1-butanol showed differences in spectra when compared to spectra of the induced cells in absence of 1-butanol. However, this was found to depend on the target location. Cells expressing the AroP protein (Figure 10) showed less impact by the alcohol showing relatively similar signature to the control presumably because this protein disperses from the inner membrane through the cytoplasm further from the external membrane which is most impacted by the alcohol. Similarly, MalE:AgBP<sub>2</sub> protein fusion (Figure 9) induced spectra were more similar to the control than did cells expressing FadL:AgBP<sub>2</sub> (Figure 8), but the former (MalE:AgBP<sub>2</sub>) was still worse than AroP:AgBP<sub>2</sub>.

### ***Integrating pgSERS into metabolic engineering***

The results presented in this research represent a first step in the use of pgSERS. The potential exists to use the *ex vivo* and *in vivo* approaches for biological discovery with further applications in the field metabolic engineering. However, these developments will not be trivial. The overall understanding of SERS spectra has proven challenging over the past two decades, but reproducibility of pgSERS spectra offers a significant advantage. Furthermore, analyses, such as the 1-butanol toxicity responses, can demonstrate the potential to monitor localized phenotype changes. This will obviously be important in determining toxicity mechanisms and will certainly be of use in measuring intracellular storage of valuable products. Overall, this research has demonstrated that pgSERS probes can be assembled *in vivo* and that both *ex vivo* and *in vivo* assembled probes can be localized effectively and provide local cell composition information.

## REFERENCES

1. **Setchell K.** 1983. Liquid-solid extraction, lipophilic gel chromatography and capillary column gas chromatography in the analysis of bile acids from biological samples, p. 1-18, *Bile Acids in Gastroenterology*. Springer.
2. **Zu TNK, Athamneh AIM, Wallace RS, Collakova E, Senger RS.** 2014. Near real-time analysis of the phenotypic responses of *Escherichia coli* to 1-butanol exposure using Raman spectroscopy. Accepted to *J Bacteriol*.
3. **Ryder AG.** 2002. Classification of narcotics in solid mixtures using principal component analysis and Raman spectroscopy. *Journal of forensic sciences* **47**:275-284.
4. **Allred CD, McCreery RL.** 1990. Near-infrared Raman spectroscopy of liquids and solids with a fiber-optic sampler, diode laser, and CCD detector. *Applied Spectroscopy* **44**:1229-1231.
5. **Yang D, Velamakanni A, Bozoklu G, Park S, Stoller M, Piner RD, Stankovich S, Jung I, Field DA, Ventrice Jr CA.** 2009. Chemical analysis of graphene oxide films after heat and chemical treatments by X-ray photoelectron and Micro-Raman spectroscopy. *Carbon* **47**:145-152.
6. **Carlsen WF, Gray DF, George WHI, Perry J, Pittaro RJ, Simons TD.** 1995. Raman spectroscopy of airway gases. Google Patents.
7. **Crow P, Stone N, Kendall C, Uff J, Farmer J, Barr H, Wright M.** 2003. The use of Raman spectroscopy to identify and grade prostatic adenocarcinoma in vitro. *British journal of cancer* **89**:106-108.

8. **Mahadevan-Jansen A, Mitchell MF, Ramanujamf N, Malpica A, Thomsen S, Utzinger U, Richards-Kortumt R.** 1998. Near-Infrared Raman Spectroscopy for In Vitro Detection of Cervical Precancers. *Photochemistry and photobiology* **68**:123-132.
9. **Snook RD, Harvey TJ, Faria EC, Gardner P.** 2009. Raman tweezers and their application to the study of singly trapped eukaryotic cells. *Integrative Biology* **1**:43-52.
10. **Athamneh AI, Senger RS.** 2012. Peptide-guided surface-enhanced Raman scattering probes for localized cell composition analysis. *Applied and environmental microbiology* **78**:7805-7808.
11. **Premasiri W, Moir D, Klempner M, Krieger N, Jones G, Ziegler L.** 2005. Characterization of the surface enhanced Raman scattering (SERS) of bacteria. *The Journal of Physical Chemistry B* **109**:312-320.
12. **Vo-Dinh T, Allain LR, Stokes DL.** 2002. Cancer gene detection using surface-enhanced Raman scattering (SERS). *Journal of Raman Spectroscopy* **33**:511-516.
13. **Aroca R.** 2006. *Surface-enhanced vibrational spectroscopy*. John Wiley & Sons.
14. **Efrima S, Zeiri L.** 2009. Understanding SERS of bacteria. *Journal of Raman Spectroscopy* **40**:277-288.
15. **Willets KA.** 2009. Surface-enhanced Raman scattering (SERS) for probing internal cellular structure and dynamics. *Analytical and bioanalytical chemistry* **394**:85-94.
16. **Premasiri WR, Gebregziabher Y, Ziegler LD.** 2011. On the difference between surface-enhanced Raman scattering (SERS) spectra of cell growth media and whole bacterial cells. *Applied spectroscopy* **65**:493-499.

17. **Athamneh AI, Senger RS.** 2012. Peptide-guided surface-enhanced Raman scattering probes for localized cell composition analysis. *Applied and environmental microbiology* **78**:7805-7808.
18. **Klein K, Steinberg R, Fiethen B, Overath P.** 1971. Fatty acid degradation in *Escherichia coli*. *European Journal of Biochemistry* **19**:442-450.
19. **Overath P, Raufuss E-M, Stoffel W, Ecker W.** 1967. The induction of the enzymes of fatty acid degradation in *Escherichia coli*. *Biochemical and biophysical research communications* **29**:28-33.
20. **Hancock R.** 1986. Model membrane studies of porin function. *Bacterial outer membranes as model systems*. New York: John Wiley and Sons.
21. **Nikaido H, Vaara M.** 1985. Molecular basis of bacterial outer membrane permeability. *Microbiological reviews* **49**:1.
22. **Black PN, Kianian S, DiRusso C, Nunn W.** 1985. Long-chain fatty acid transport in *Escherichia coli*. Cloning, mapping, and expression of the *fadL* gene. *Journal of Biological Chemistry* **260**:1780-1789.
23. **Busch W, Saier MH.** 2002. The transporter classification (TC) system, 2002. *Critical reviews in biochemistry and molecular biology* **37**:287-337.
24. **Black P.** 1988. The *fadL* gene product of *Escherichia coli* is an outer membrane protein required for uptake of long-chain fatty acids and involved in sensitivity to bacteriophage T2. *Journal of bacteriology* **170**:2850-2854.
25. **Black PN.** 1991. Primary sequence of the *Escherichia coli* *fadL* gene encoding an outer membrane protein required for long-chain fatty acid transport. *Journal of bacteriology* **173**:435-442.

26. **Van den Berg B, Black PN, Clemons WM, Rapoport TA.** 2004. Crystal structure of the long-chain fatty acid transporter FadL. *Science* **304**:1506-1509.
27. **Cristalli G, DiRusso CC, Black PN.** 2000. The amino-terminal region of the long-chain fatty acid transport protein FadL contains an externally exposed domain required for bacteriophage T2 binding. *Archives of biochemistry and biophysics* **377**:324-333.
28. **van den Berg B.** 2005. The FadL family: unusual transporters for unusual substrates. *Current opinion in structural biology* **15**:401-407.
29. **Dassa E, Lambert P.** 1997. Activity of protein MalE (maltose-binding protein) fused to cytoplasmic and periplasmic regions of an *Escherichia coli* inner membrane protein. *Research in microbiology* **148**:389-395.
30. **Bassford Jr PJ.** 1990. Export of the periplasmic maltose-binding protein of *Escherichia coli*. *Journal of bioenergetics and biomembranes* **22**:401-439.
31. **Quioco FA, Ledvina PS.** 1996. Atomic structure and specificity of bacterial periplasmic receptors for active transport and chemotaxis: variation of common themes. *Molecular microbiology* **20**:17-25.
32. **Spurlino JC, Lu G-Y, Quioco F.** 1991. The 2.3-Å resolution structure of the maltose-or maltodextrin-binding protein, a primary receptor of bacterial active transport and chemotaxis. *Journal of Biological Chemistry* **266**:5202-5219.
33. **Sharff AJ, Rodseth LE, Spurlino JC, Quioco FA.** 1992. Crystallographic evidence of a large ligand-induced hinge-twist motion between the two domains of the maltodextrin binding protein involved in active transport and chemotaxis. *Biochemistry* **31**:10657-10663.

34. **Ames GF.** 1964. Uptake of amino acids by *Salmonella typhimurium*. Archives of biochemistry and biophysics **104**:1-18.
35. **Brown K.** 1970. Formation of aromatic amino acid pools in *Escherichia coli* K-12. Journal of bacteriology **104**:177-188.
36. **Cosgriff AJ, Pittard A.** 1997. A topological model for the general aromatic amino acid permease, AroP, of *Escherichia coli*. Journal of bacteriology **179**:3317-3323.
37. **Cosgriff AJ, Brasier G, Pi J, Dogovski C, Sarsero JP, Pittard A.** 2000. A study of AroP-PheP chimeric proteins and identification of a residue involved in tryptophan transport. Journal of bacteriology **182**:2207-2217.
38. **Honore N, Cole ST.** 1990. Nucleotide sequence of the aroP gene encoding the general aromatic amino acid transport protein of *Escherichia coli* K-12: homology with yeast transport proteins. Nucleic acids research **18**:653.
39. **Arnold K, Kiefer F, Kopp J, Battey JN, Podvynec M, Westbrook JD, Berman HM, Bordoli L, Schwede T.** 2009. The Protein Model Portal. Journal of structural and functional genomics **10**:1-8.
40. **Sedlak RH, Hnilova M, Grosh C, Fong H, Baneyx F, Schwartz D, Sarikaya M, Tamerler C, Traxler B.** 2012. Engineered *Escherichia coli* silver-binding periplasmic protein that promotes silver tolerance. Applied and environmental microbiology **78**:2289-2296.
41. **Guzman LM, Belin D, Carson MJ, Beckwith J.** 1995. Tight regulation, modulation, and high-level expression by vectors containing the arabinose PBAD promoter. Journal of Bacteriology **177**:4121-4130.

42. **Athamneh AI, Alajlouni RA, Wallace RS, Seleem MN, Senger RS.** 2014. Phenotypic profiling of antibiotic response signatures in *Escherichia coli* using Raman spectroscopy. *Antimicrobial agents and chemotherapy* **58**:1302-1314.

## CHAPTER SIX

# CONCLUSIONS

Critical to the advancement of microbial biofuel production and donor organ preservation, is access to analytical techniques that can be applied in real-time. In this dissertation, Raman spectroscopy and multivariate statistical analyses were used to study; (i) alcohol toxicity in *E. coli*, (ii) perfused organ health using the new VasoWave<sup>®</sup> technology, and (iii) target sub-cellular study of microbes employing molecular biology design techniques. Raman spectroscopy is of interest for bacterial phenotyping because it can be performed: (i) in near real-time, (ii) with minimal sample preparation (label-free), and (iii) with minimal spectral interference from water.

In the initial study, Raman spectroscopy was used to study the time-course phenotypic responses of *E. coli* (DH5- $\alpha$ ) to 1-butanol exposure (1.2% v/v). Here, traditional methods of analysis such as GC-MS and fluorescence anisotropy data were correlated with Raman data which showed good correlation ( $R^2 \geq 0.75$ ) between techniques. Several macromolecules were investigated in this paper in relation to the traditional method chosen. For example, GC-MS data allowed for comparison of Raman peaks assigned to different macromolecules (saturated, unsaturated, and cyclopropane fatty acids), membrane fluidity data were compared with Raman peaks used to measure the degree of order or disorder within the cell membrane, whereas data from Bradford assay test allowed comparison with Raman peak intensity for total proteins. The observed phenotypic responses following 1-butanol exposure included: (i) decreased saturated fatty acids levels, (ii) retention of unsaturated fatty acids and low levels of cyclopropane fatty acids, (iii)

increased membrane fluidity following the initial response of increased rigidity, and (iv) no changes in total protein content or protein-derived amino acid composition.

In the follow-up study, *E. coli* cells were exposed to different 4-carbon alcohols: (i) 1-butanol and 2-butanol (straight chain alcohols), (ii) isobutanol and tert-butanol (branched chain alcohols), and (iii) 1,4-butanediol (no terminal alkyl end). The Raman data were analyzed using the in-house MATLAB software – Raman Data Processing (RDA) toolbox, which allows for multivariate statistical analysis, like principle components analysis (PCA) and linear discriminant analysis (DA). In this work, distinct phenotype clustering based on alcohol chain length and/or positioning of the OH group were explored using “chemometric fingerprint”. While the isobutanol and tert-butanol treated cells showed similar phenotypes, isobutanol was significantly more toxic. In addition, the phenotypic response was found to take place largely within 60 min of culture treatment; however, significant responses (especially for 1,4-butanediol) were still occurring at 180 min post-treatment. The usefulness of the “chemometric fingerprinting” is that it helps eliminate any ambiguity that may exist from Raman band assignments as is evident from the literature. The approach allows for comparison of different phenotypes and how they may relate to an organism’s phenotypic response. To further ascertain these new capabilities, “chemometric fingerprinting” was again applied to monitor the overall health and degradation of porcine livers perfused *ex vivo* using the VasoWave<sup>®</sup> system. Raman spectroscopy is an excellent analytical technique for organ monitoring as it is label-free, non-invasive and can be applied in real-time. Three livers, perfused under different pressures and temperatures, were compared over a 24 h *ex vivo* perfusion time-course. Results indicated that perfusion pressure was a more significant factor in organ degradation than was temperature. In addition, a non-linear degradation time-course was identified for all three perfused livers, and this time-course was different for individual livers,

demonstrating the time-dependent transition from its initial “healthy” state towards a more “unhealthy” degenerative state at 24 h. Finally, the related technique of surface-enhanced Raman scattering was employed together with *ex vivo* and *in vivo* assembled probes for sub-cellular target analyses in *E. coli* DH5- $\alpha$ . Three different sub-cellular locations: (i) cell outer membrane (FadL protein), (ii) cell periplasm (MalE protein) and (iii) cell cytoplasm (AroP protein) were investigated. The developed technique, *in vivo* pgSERS, proved very efficient and clearly showed peak specificity for target locations from the SERS acquired spectra. FadL:AgBP2 fused proteins showed peaks rich in lipids and polysaccharides as will be present in the *E. coli* cell membrane. MalE:AgBP2 showed a mixture of outer membrane components with inner membrane components such as nucleic acids. AroP:AgBP2 fused protein resulted in a spectrum devoid of outer membrane components like lipids while being heavily rich with peaks for nucleic acid content which is quiet similar to peaks in the uncontrolled SERS spectrum.

The applications of real-time analysis of biological samples with Raman spectroscopy are numerous, and the method is capable of delivering near real-time phenotyping. The results of this research demonstrate the power of Raman for phenotypic profiling of *E. coli* cells. In addition, real-time phenotypic monitoring has tremendous application to the field of biosensing, as cell composition changes may be observed in response to small quantities of environmental toxins as well as chemical or biological warfare agents. Finally, the ability to deliberately target specific locations within or outside a cell has tremendous potential for diverse research with microbes and endless applications. Different pgSERS probes can be designed for specific study with careful thought into the design process all at the control of the researcher.

## CHAPTER SEVEN: SUPPLEMENTARY MATERIALS

Near real-time analysis of the phenotypic responses of *Escherichia coli* to 1-butanol exposure using Raman spectroscopy

### Supplementary Appendix

**Supplementary Table 1.** Correlation coefficients (R values) for FAME analysis data with Raman spectroscopy data using Raman bands assigned in the literature and new bands identified in this research.

Raman Band (cm <sup>-1</sup> )	Saturated Fatty Acids (R)	Unsaturated Fatty Acids (R)	Cyclopropane Fatty Acids (R)	Raman Signature Assignment	References
877	0.014	-	-	Symmetric stretching (C-C-N <sup>+</sup> )	(1)
968	-	-	-	Lipids	(1)
980	0.20	-	-	Bending (=CH)	(1)
1057	-	0.37	-	Lipids	(1)
1064	-	0.09	-	Vibrational stretch (C-C)	(1)
1078	-	-	-	Vibrational stretch (C-C) (C-O)	(1)
1095	-	0.64	-	Lipids	(1)
1123	0.33	-	0.56	Vibrational stretch (C-C)	(1, 2)
1131	0.02	-	0.37	Fatty Acid	(1)
1168	-	-	0.14	Lipid Assignment (C=C) (COH)	(1)
1249	-	0.53	-	Bend (=CH)	(3)
1250	-	0.57	-	Bend (=CH)	(3)
1251	-	0.60	-	Bend (=CH)	(3)
1252	-	0.59	-	Bend (=CH)	(3)
1253	-	0.60	-	Bend (=CH)	(3)
1254	-	0.60	-	Bend (=CH)	(3)
1255	-	0.61	-	Lipids, Bend (=CH)	(1, 3)
1256	-	0.62	-	Bend (=CH)	(3)

1257	--	0.64	-	Bend (=CH)	(3)
1258	-	0.66	-	Bend (=CH)	(3)
1259	-	0.69	-	Bend (=CH)	(3)
1260	-	0.72	-	Bend, <i>cis</i> Stretch (=CH), Deformation (-CH <sub>2</sub> )	(1, 3, 4)
1263	-	0.76	-	Bend, Symmetric Rocking (=CH)	(2, 3)
1264	-	0.75	-	Bend (=CH)	(3)
1265	-	0.71	-	Bend (=CH)	(3)
1266	-	0.64	-	Bend (=CH), <i>cis</i> Deformation (=CH)	(1, 3, 5)
1267	-	0.55	-	Lipid (CH), Bend (=CH)	(1, 3)
1268	-	0.46	-	Deformation (=CH)	(1)
1270	-	0.40	-	Lipid assignment (C=C)	(1)
1298	-	0.12	0.30	Palmitic Acid, Acyl Chains, Fatty Acids	(1)
1299	-	0.03	0.40	Deformation (CH <sub>2</sub> )	(1)
1300	0.07	-	0.48	Twist (-CH <sub>2</sub> )	(2)
1301	0.16	-	0.54	Vibration (-CH) Twist (-CH <sub>2</sub> )	(1, 3)
1302	0.23	-	0.59	Lipid Assignment, Bend, Twist (-CH <sub>3</sub> ) (-CH <sub>2</sub> )	(1)
1304	0.29	-	0.64	Deformation (-CH <sub>2</sub> )	(1)
1307	0.2	-	0.60	Bend, Twist (-CH <sub>3</sub> ) (-CH <sub>2</sub> )	(1)
1309	0.02	-	0.49	Bend, Twist (-CH <sub>3</sub> ) (-CH <sub>2</sub> )	(1)
1313	-	0.31	0.11	Twist (-CH <sub>2</sub> CH <sub>3</sub> )	(1)
1367	-	0.03	0.47	Phospholipids, Symmetric Vibration (-CH <sub>3</sub> )	(1)
1379	-	0.02	0.31	Lipid Assignment	(1)
1393	0.16	-	0.53	Rocking (CH)	(1)
1437	0.10	-	-	Deformation (CH <sub>2</sub> )	(1)
1439	0.2	-	-	Deformation, Scissoring (CH <sub>2</sub> )	(1)

1440	0.24	-	-	Deformation (CH) (CH <sub>2</sub> ) (CH <sub>3</sub> )	(1)
1441	0.28	-	-	Deformation, Bend, Scissoring (CH) (CH <sub>2</sub> ) (CH <sub>3</sub> )	(1)
1442	0.31	-	-	Fatty Acids, Deformation, Bend (CH <sub>2</sub> ) (CH <sub>3</sub> )	(1)
1443	0.32	-	-	Fatty Acids, Deformation (CH <sub>2</sub> )	(1)
1444	0.32	-	-	Fatty Acids, Deformation (CH <sub>2</sub> )	(1)
1445	0.3	-	-	Phospholipids, Deformation, Bend, Scissoring (CH <sub>2</sub> ) (CH <sub>3</sub> ) (-CH <sub>2</sub> CH <sub>3</sub> )	(1)
1446	0.26	-	-	Deformation, Bend (CH <sub>2</sub> )	(1)
1447	0.2	-	-	Deformation, Bend (CH <sub>2</sub> )	(1)
1448	0.13	0.00	-	Deformation (CH <sub>2</sub> ) (-CH <sub>2</sub> CH <sub>3</sub> )	(1)
1449	0.05	0.09	-	Lipids, Vibration (CH)	(1)
1450	-	0.18	-	Deformation, Bend (CH <sub>2</sub> ) (CH)	(1)
1451	-	0.26	-	Deformation (-CH <sub>2</sub> CH <sub>3</sub> )	(1)
1454	-	0.27	-	Overlapping Asymmetric CH <sub>3</sub> Bending and CH <sub>2</sub> Scissoring	(1)
1460	-	0.21	-	Deformation (CH <sub>2</sub> ) (CH <sub>3</sub> )	(1)
1465	-	0.40	-	Lipids	(1)
1525	-	0.27	-	Vibration (C=C)	(1)
1554	0.38	-	0.79	Discovered in this research	
1580	-	-	0.54	Stretching (C-C)	(1)
1582	0.06	-	0.60	Discovered in this research	
1585	0.16	-	0.65	Olefinic Stretch (C=C)	(1)
1607	0.60	-	0.82	Discovered in this research	
1616	0.68	-	0.79	Discovered in this research	
1628	-	0.13	0.30	Stretch (C=C)	(1)
1652	-	0.38	-	Lipids, Stretch (C=C)	(1)
1655	-	0.40	-	Lipids, Stretch (C=C) (C=O)	(1)
1656	-	0.37	-	Lipids, Stretch, <i>cis</i> Vibration (C=C)	(1)

1657	-	0.32	-	Fatty Acids	(1)
1660	-	0.13	-	Lipids, Fatty Acids, <i>cis</i> Vibration (C=C)	(1)
1667	-	0.11	-	Stretch (C=C) (C=O)	(1)
1674	-	0.54	-	Stretch (C=C)	(1)
1734	-	0.21	-	Lipids, Stretch (C=O)	(1)
1736	-	0.18	-	Lipids, Esters (C=O)	(1)
1738	-	0.27	-	Lipids	(1)
1744	-	-	-	Lipids (Carbonyl Group)	(1)
1745	0.1	-	0.11	Lipid Assignment, Phospholipids, Vibration (C=O)	(1)
1746	0.21	-	0.31	Lipids, Stretch (C=O)	(1)
1747	0.22	-	0.42	Lipids (C=O)	(1)
1750	-	-	0.10	Lipids, Fatty Acids (C=C) (C=O)	(1)
1754	-	0.31	-	Lipids (C=O)	(1)
2817	-	0.37	-	Symmetric Stretch (-CH <sub>2</sub> )	(1)
2840	-	0.49	-	Symmetric Stretch (-CH <sub>3</sub> )	(1)
2850	-	0.19	0.10	Lipids, Fatty Acids, Symmetric Stretch (-CH <sub>2</sub> ) (-CH <sub>3</sub> )	(1)
2855	0.52	-	0.53	Symmetric Stretch (-CH <sub>2</sub> ) (-CH <sub>3</sub> ), Asymmetric Stretch (-CH <sub>2</sub> )	(1, 2)
2856	0.59	-	0.58	Symmetric Stretch (-CH <sub>2</sub> ) (-CH <sub>3</sub> ), Asymmetric Stretch (-CH <sub>2</sub> )	(1, 2)
2858	0.60	-	0.60	Symmetric Stretch (-CH <sub>2</sub> ) (-CH <sub>3</sub> ), Asymmetric Stretch (-CH <sub>2</sub> )	(1, 2)
2859	0.55	-	0.56	Symmetric Stretch (-CH <sub>2</sub> ) (-CH <sub>3</sub> ), Asymmetric Stretch (-CH <sub>2</sub> )	(1, 2)
2868	0.76	-	0.63	Symmetric Stretch (-CH <sub>2</sub> )	(1)

				(-CH <sub>3</sub> ), Asymmetric Stretch (-CH <sub>2</sub> )	
2870	0.78	-	0.64	Symmetric Stretch (-CH <sub>2</sub> ) (-CH <sub>3</sub> ), Asymmetric Stretch (-CH <sub>2</sub> )	(1, 6)
2876	0.67	-	0.47	Stretch (-CH), Asymmetric Stretch (-CH <sub>2</sub> )	(1)
2883	-	0.27	-	Stretch (-CH), Asymmetric Stretch (-CH <sub>2</sub> )	(1)
2889	-	0.17	0.22	Asymmetric Stretch (-CH <sub>2</sub> )	(1)
2893	-	0.20	0.21	Symmetric Stretch (-CH <sub>3</sub> )	(1)
2900	-	0.51	-	Stretch (-CH)	(1)
2910	0.67	-	0.52	Stretch (-CH <sub>3</sub> )	(1)
2915	0.74	-	0.47	Lipids (-CH)	(1)
2924	0.76	-	0.60	Asymmetric Stretch (-CH <sub>2</sub> )	(6, 7)
2930	0.79	-	0.50	Asymmetric Stretch (-CH)	(2)
2933	0.81	-	0.47	Asymmetric Stretch (-CH)	(1)
2940	0.62	-	0.38	Vibration (-CH) (-CH <sub>2</sub> )	(1)
2954	-	0.23	-	Asymmetric Stretch (-CH <sub>3</sub> )	(6)
2956	-	0.51	-	Asymmetric Stretch (-CH <sub>3</sub> )	(1)
2960	-	0.65	-	Asymmetric Stretch (-CH <sub>3</sub> )	(1)
2970	-	0.55	-	Asymmetric Stretch (-CH <sub>3</sub> )	(1, 5)
3008	-	0.52	-	Lipids, Fatty Acids, Asymmetric Stretch (=CH)	(1)
3010	-	0.36	-	Unsaturated Fatty Acids, Stretch (=CH)	(1)
3015	0.04	0.08	-	Lipids, Vibration (=CH)	(1)

\* Negative correlation coefficients are represented by a dash.

**Supplementary Table 2.** All literature cited Raman bands considered for each amino acid (8, 9) for compiling the optimized results shown in Table 1.

<b>Amino Acids</b>	<b>Associated Raman Bands (cm<sup>-1</sup>)</b>
Ala	399, 533, 771, 852, 922, 1021, 1115, 1149, 1308, 1361, 1378, 1411, 1464, 1485, 1599
Arg	857, 873, 930, 985, 1036, 1086, 1176, 1199, 1264, 1310, 1317, 1408, 1423, 1443, 1477
Asp/Asn	749, 779, 877, 939, 1084, 1125, 1338, 1408, 1426, 1695
Cys	455, 499, 542, 613, 678, 785, 873, 967, 1341, 1385, 1410
Glu/Gln	623, 669, 873, 917, 988, 1080, 1182, 1319, 1379, 1422, 1462, 1637, 1682
Gly	359, 496, 603, 898, 1036, 1327, 1332, 1413, 1442, 1458, 1515
His	539, 657, 731, 784, 806, 854, 919, 929, 964, 977, 1062, 1088, 1113, 1176, 1225, 1252, 1272, 1319, 1336, 1349, 1355, 1409, 1431, 1443, 1500, 1578
Ile	536, 557, 675, 765, 820, 825, 852, 873, 918, 964, 993, 1017, 1033, 1134, 1168, 1191, 1257, 1309, 1329, 1338, 1355, 1398, 1413, 1421, 1448, 1465, 1514, 1583, 1619
Leu	771, 836, 848, 1135, 1178, 1187, 1243, 1342, 1410, 1457, 1583, 1623
Lys	625, 785, 849, 877, 912, 946, 975, 988, 1036, 1055, 1064, 1072, 1097, 1141, 1168, 1305, 1321, 1341, 1360, 1399, 1414, 1433, 1447, 1456, 1464, 1485, 1609
Met	645, 682, 700, 721, 765, 805, 877, 1068, 1175, 1245, 1265, 1321, 1343, 1355, 1415, 1428, 1447
Phe	469, 525, 606, 622, 748, 821, 835, 915, 954, 1005, 1036, 1158, 1188, 1214, 1310, 1413, 1608
Pro	642, 843, 899, 921, 986, 1035, 1084, 1239, 1453
Ser	610 805, 814, 854, 857, 969, 1010, 1127, 1220, 1301, 1327, 1417, 1468
Thr	447, 564, 872, 932, 1045, 1116, 1251, 1341, 1410, 1419, 1458
Trp	756, 759, 849, 875, 961, 1010, 1013, 1078, 1120, 1233, 1253, 1340, 1360, 1426, 1460, 1489, 1559
Tyr	641, 798, 831, 847, 986, 1044, 1180, 1201, 1267, 1328, 1615
Val	542, 665, 753, 776, 825, 850, 902, 948, 965, 1000, 1066, 1100, 1126, 1200, 1273, 1300, 1331, 1354, 1396, 1400, 1427, 1454, 1467, 1509

**Supplementary Table 3.** Alternative Raman band assignment Set 1 for amino acids. Correlation coefficient (R) between Raman and UPLC data = 0.86.

\*

Amino Acids	Optimum Raman Band (cm <sup>-1</sup> )	Amino Acid Composition Determined by Raman	Amino Acid Composition Determined by UPLC	Published Amino Acid Composition
Ala	1308	11.4	11.1	9.60
Arg	1423	3.53	3.39	5.53
Asp/Asn	1338	11.9	8.98	9.01
Cys	785	4.47	1.64*	1.64
Glu/Gln	1637	6.75	9.16	9.84
Gly	1327	10.9	12.0	11.5
His	854	2.01	0.890	1.77
Ile	1329	11.2	8.76	5.43
Leu	1457	11.7	11.4	8.42
Lys	1168	2.19	5.24	6.41
Met	877	1.63	0.467	2.87
Phe	1413	3.05	4.59	3.46
Pro	843	0.749	1.02	4.13
Ser	1010	4.50	4.42	4.03
Thr	1116	3.48	6.26	4.74
Trp	1426	3.68	1.06*	1.06
Tyr	641	1.69	0.390	2.58
Val	1126	5.20	9.22	7.91
Sum	-	100	100	100

Values for Cys and Trp could not be resolved by the UPLC method. Cys is converted to several oxidation products, while Trp is destroyed during acidic protein hydrolysis used in this research. The published literature values were used for Cys and Trp.

\*\* Amino acid composition is defined as the fraction of each amino acid in *E. coli* total protein.

\*\*\* Possible overlapping bands: Gly (1327 cm<sup>-1</sup>) / Ile (1329 cm<sup>-1</sup>); Arg (1423 cm<sup>-1</sup>) / Trp (1426 cm<sup>-1</sup>)

**Supplementary Table 4.** Alternative Raman band assignment Set 2 for amino acids. Correlation coefficient (R) between Raman and UPLC data = 0.89.

Amino Acids	Optimum Raman Band (cm <sup>-1</sup> )	Amino Acid Composition Determined by Raman	Amino Acid Composition Determined by UPLC	Published Amino Acid Composition
Ala	1308	12.0	11.1	9.60
Arg	1199	2.67	3.39	5.53
Asp/Asn	1338	12.5	8.98	9.01
Cys	499	1.57	1.64*	1.64
Glu/Gln	1637	7.10	9.16	9.84
Gly	1442	10.7	12.0	11.5
His	964	1.89	0.890	1.77
Ile	1355	7.03	8.76	5.43
Leu	1457	12.3	11.4	8.42
Lys	1064	2.55	5.24	6.41
Met	1068	3.13	0.467	2.87
Phe	1413	3.21	4.59	3.46
Pro	843	0.787	1.02	4.13
Ser	1417	3.46	4.42	4.03
Thr	1116	3.66	6.26	4.74
Trp	849	1.57	1.06*	1.06
Tyr	641	1.77	0.390	2.58
Val	1331	12.1	9.22	7.91
Sum	-	100	100	100

\* Values for Cys and Trp could not be resolved by the UPLC method. Cys is converted to several oxidation products, while Trp is destroyed during acidic protein hydrolysis used in this research. The published literature values were used for Cys and Trp.

\*\* Amino acid composition is defined as the fraction of each amino acid in *E. coli* total protein.

\*\*\* Possible overlapping bands: Pro (843 cm<sup>-1</sup>) / Trp (849 cm<sup>-1</sup>); Lys (1064 cm<sup>-1</sup>) / Met (1068 cm<sup>-1</sup>); Val (1331 cm<sup>-1</sup>) / Asp/Asn (1338 cm<sup>-1</sup>)

**Supplementary Table 5.** Alternative Raman band assignment Set 3 for amino acids. Correlation coefficient (R) between Raman and UPLC data = 0.85.

<b>Amino Acids</b>	<b>Optimum Raman Band (cm<sup>-1</sup>)</b>	<b>Amino Acid Composition Determined by Raman</b>	<b>Amino Acid Composition Determined by UPLC</b>	<b>Published Amino Acid Composition</b>
Ala	1464	10.5	11.1	9.60
Arg	1036	1.97	3.39	5.53
Asp/Asn	1426	3.83	8.98	9.01
Cys	1385	4.08	1.64*	1.64
Glu/Gln	1319	11.6	9.16	9.84
Gly	1332	12.2	12.0	11.5
His	964	1.87	0.890	1.77
Ile	1257	8.66	8.76	5.43
Leu	1457	12.2	11.4	8.42
Lys	785	4.65	5.24	6.41
Met	765	1.22	0.467	2.87
Phe	1214	6.20	4.59	3.46
Pro	986	2.38	1.02	4.13
Ser	805	1.73	4.42	4.03
Thr	1116	3.63	6.26	4.74
Trp	1078	4.42	1.06*	1.06
Tyr	798	1.82	0.390	2.58
Val	1354	7.10	9.22	7.91
Sum	-	100	100	100

\* Values for Cys and Trp could not be resolved by the UPLC method. Cys is converted to several oxidation products, while Trp is destroyed during acidic protein hydrolysis used in this research. The published literature values were used for Cys and Trp.

\*\* Amino acid composition is defined as the fraction of each amino acid in *E. coli* total protein.

\*\*\* Possible overlapping bands: Tyr (798 cm<sup>-1</sup>) / Ser (805 cm<sup>-1</sup>)

## REFERENCES

1. **Movasaghi Z, Rehman S, Rehman IU.** 2007. Raman spectroscopy of biological tissues. *Appl Spectrosc Rev* **42**:493-541.
2. **Afseth NK, Segtnan VH, Marquardt BJ, Wold JP.** 2005. Raman and near-infrared spectroscopy for quantification of fat composition in a complex food model system. *Appl Spectrosc* **59**:1324-1332.
3. **Notingher I.** 2007. Raman spectroscopy cell-based biosensors. *Sensors* **7**:1343-1358.
4. **Wu H, Volponi JV, Oliver AE, Parikh AN, Simmons BA, Singh S.** 2011. *In vivo* lipidomics using single-cell Raman spectroscopy. *Proc Natl Acad Sci U S A* **108**:3809-3814.
5. **Lee T-H, Chang J-S, Wang H-Y.** 2013. Rapid and *in vivo* quantification of cellular lipids in *Chlorella vulgaris* using near-infrared Raman spectrometry. *Anal Chem* **85**:2155-2160.
6. **Schultz ZD, Levin IW.** 2011. Vibrational spectroscopy of biomembranes. *Annu Rev Anal Chem* **4**:343-366.
7. **Cherney DP, Conboy JC, Harris JM.** 2003. Optical-trapping Raman microscopy detection of single unilamellar lipid vesicles. *Anal Chem* **75**:6621-6628.
8. **Zhu G, Zhu X, Fan Q, Wan X.** 2011. Raman spectra of amino acids and their aqueous solutions. *Spectrochimica acta. Part A, Molecular and biomolecular spectroscopy* **78**:1187-1195.
9. **Neidhardt FC, Ingraham JL, Schaechter M.** 1990. *Physiology of the bacterial cell: a molecular approach.* Sinauer Associates Sunderland, MA.